ARAI Journal of Mobility Technology

A Quarterly Peer-Reviewed Journal

https://araijournal.com

Volume 2, Issue 2, April-June, 2022

Publication from

ARAI®

Progress through Research

TÜV SÜD

The Automotive Research Association of India

An ISO 9001, ISO 14001, ISO 27001, OHSAS 18001 and NABL Accredited R&D Institute

Published by

BSP BOOKS

BSP Books Pvt. Ltd.

Foreword

The rapidly changing customer preferences in mobility, contribution of the sector to climate change and the drive for sustainability drives the need for accelerated innovation higher than never before. In addition to the constant demands to make products low cost, low maintenance, improved reliability, there is also a mindful demand for improved safety, sustainability, connectivity, self-serviceability, convenience, etc. As a result, the desired form, fit, and functional needs of the product are becoming more and more complex with greater integration to both physical and virtual world. Accelerated transition to products catering to these complexities and increased functionalities would thus require simultaneous innovations in design for circularity, safety, technologies for net-zero emission, low carbon fuels, preventive maintenance, telematics etc.

One of the key ways to achieve this accelerated transition is through increased use of advanced simulations, analysis led design and validations as well as the use of data and data analytics. Use of machine learning and advanced analytics with connectivity to cloud computing is already exploding rapidly around the world. Progress in simulations and numerical methods to solve complex issues in EV and battery systems are being made. At the same time, continued innovations and new chemistries are being researched upon to improve the performance and safety of the batteries. India also continues to look for alternate fuels as well as new materials and chemistry for batteries to address the issues of energy security and reduce dependence on petroleum and Lithium, respectively.

This issue presents to you, articles spread across important topics covering automotive safety, electric/hybrid mobility, advanced numerical and analytical methods and powertrain technologies. We look forward to using this platform to bring to you solutions to more real-world challenges and research findings which will help the community to together transition into sustainable and safe-mobility.

Dr. Anuradda Ganesh
Chief Technical Advisor &
Director, Cummins Technologies India Pvt Ltd., Pune
Emeritus Professor, IIT-B, Mumbai

ARAI Journal of **Mobility Technology**

A Quarterly Peer-Reviewed Journal

ADVISORY BOARD MEMBERS

SUBJECT EXPERTS

Dr. Abhijeet Marathe
General Manager - Automotive Research Association of India. Survey No. 102, Vetal Hill, off Paud Road, Kothrud, Pune - 411 038

Dr. Akella Sharma
Vice President - Automotive Sector - Mahindra & Mahindra Limited. Mahindra Towers, 17/18, Pattullous Road, Royapettah, Anna Salai, Mount Road, Express Estate, Chennai, Tamil Nadu 600002

Dr. Amala Justus Selvam
Professor and Head - Vel Tech University. Automobile Engineering Department, No.42, Avadi-Vel Tech Road, Vel Nagar, Avadi, Chennai – 600 062, Tamil Nadu, India.

Dr. Arun Jaura
Chief Technology Officer - Hero MotoCorp. Jaipur, Rajasthan, India

Dr. B. Ashok
Associate Professor - VIT University. Department of Automotive, School of Mechanical Engineering, Vellore Campus, Tiruvalam Rd, Katpadi, Vellore, Tamil Nadu 632014

Dr. B. S. Kothavale
Professor - Dr Vishwanath Karad MIT World Peace University. School of Mechanical Engineering, S.No.124, Paud Road, Kothrud, Pune-411038

Dr. Bharatkumar Ahuja
Professor & Director - College of Engineering Pune (CoEP). Wellesley Rd, Shivajinagar, Pune, Maharashtra 411005

Dr. Fangwu (Mike) Ma
Lead Professor - Jilin University. Automotive Research Institute, China, Jilin, Changchun, Chaoyang District, Changchun

Dr. Ganesh Kakandikar
Professor and Head - Dr. Vishwanath Karad MIT World Peace University, Pune. School of Mechanical Engineering, S.No.124, Paud Road, Kothrud, Pune-411038

Dr. K. C. Vora
Emeritus Professor - College of Engineering Pune (CoEP). Wellesley Rd, Shivajinagar, Pune, Maharashtra 411005

Dr. Luděk Hynčík
Associate Professor - University of West Bohemia. Univerzitní 2732, 301 00 Plzeň 3, Czechia

Dr. M. Suresh
Assistant Professor - Karunya Institute of Technology and Sciences. Department of Mechanical Engineering, Karunya Institute of Technology and Sciences, Coimabtore, Tamil Nadu, India-641114

Dr. M.V. Uchgoankar
Ex - Sr. Deputy Director - Automotive Research Association of India. Survey No. 102, Vetal Hill, off Paud Road, Kothrud, Pune - 411 038

Dr. Mohan Godse
Proprietor - U 2 I. Pune, Maharashtra, India

Dr. Mohd Rafiq B. Agrewale
Manager - Automotive Research Association of India. Survey No. 102, Vetal Hill, off Paud Road, Kothrud, Pune - 411 038

Dr. Nagesh H. Walke
Deputy Director - Automotive Research Association of India. Survey No. 102, Vetal Hill, off Paud Road, Kothrud, Pune - 411 038

Dr. P A Lakshminarayanan
Former - Technical Advisor - Simpson & Co. Ltd., No. 861, 862, Anna Salai, Border Thottam, Padupakkam, Triplicane, Chennai, Tamil Nadu 600002

Dr. P. P. Chattaraj
Additional Director - National Automotive Testing and R&D Infrastructure Project (NATRiP). Madhavpur, Sagore-Manpur Road, Khandawa, Dhar, Pithampur 454774, Madhya Pradesh

Dr. P.K. Ajeet Babu
Manager - Automotive Research Association of India. Survey No. 102, Vetal Hill, off Paud Road, Kothrud, Pune - 411 038

Dr. R Basargekar
Head, Research & Technology Centre and Technical Director - APPL Industries, Survey No. 279 (1 & 2), Maan,, Mulshi, Hinjawdi, Pune, Maharashtra 411057

Dr. Ravindra Utgikar
Vice President - Corporate Strategy & Marketing - Praj Industries Ltd., Praj Tower 274 & 275/2, Bhumkar Chowk, Hinjewadi Road, Hinjewadi, Pune 411057, India.

Dr. Sanjay A Patil
General Manager - Automotive Research Association of India. Survey No. 102, Vetal Hill, off Paud Road, Kothrud, Pune - 411 038

Dr. S.A. Mohan Krishna
Associate Professor - Vidyavradhaka College of Engineering. Department of Mechanical Engg., Vidyavradhaka College of Engineering, Mysuru, Karnataka, India

Dr. Sanjay Arole
Director - Automotive Materials & Manufacturing Engineering Services, Education Administration & Management - SMA Engineering Solutions, 4, Surya Tower, 50A, Erandwane, Near Mehandale Garage Chowk, Pune, Maharashtra 411004

Dr. Sanjay D. Yadav
Professor - Rajarambapu Institute of Technology, Rajaramnagar. Automobile Engineering Department, Post-Sakharale. Tal. Walwa Dist. Sangli PIN- 415414, Maharashtra State (INDIA)

Dr. Sarit Kumar Das
Institute Chair Professor - Indian Institute of Technology-Madras. Indian Institute Of Technology, Chennai, Tamil Nadu 600036

Dr. Satyam Sahay
John Deere Fellow - John Deere Technology Centre India. Level 1 Tower 3, Cybercity, Magarpatta, Pune, Maharashtra 411028

Dr. Senthil Muthu Kumar Thiagamani
Associate Professor - Kalasalingam Academy of Research and Education. Anand Nagar, Krishnankoil, Srivilliputhur, Tamil Nadu 626102

Dr. Sharada Vikram Chougule
Professor and Head of Department - Finolex Academy of Management and Technology. Electronics and Telecommunication Engineering, P-60¸ P- 60/1, MIDC, Mirjole Block, Ratnagiri, Maharashtra 415639

Dr. Shivprakash Barve
Professor - Dr. Vishwanath Karad MIT World Peace University, Pune. S.No.124, Paud Road, Kothrud, Pune-411038

Dr. Simhachalam D. Juttu
General Manager - Automotive Research Association of India. Survey No. 102, Vetal Hill, off Paud Road, Kothrud, Pune - 411 038

Dr. Srinivas Gunti
Sr. Deputy General Manager, Automotive Sector - Mahindra & Mahindra Limited. Mahindra Towers, 17/18, Pattullous Road, Royapettah, Anna Salai, Mount Road, Express Estate, Chennai, Tamil Nadu 600002

Dr. Sundarapandian Vaidyanathan
Professor (R & D Centre) - Vel-Tech University. No.42, Avadi-Vel Tech Road, Poonamallee - Avadi High Rd, Vel Nagar, Chennai, Tamil Nadu 600062

Dr. Sushil S. Ramdasi
Deputy Director - Automotive Research Association of India. Survey No. 102, Vetal Hill, off Paud Road, Kothrud, Pune - 411 038

Dr. Vijay Narkhede
Senior Manager (R&D) - Süd-Chemie India. A-1/2/3, Nandesari Industrial Developmental Area, P.O. Nandesari, Vadodara district, Gujarat 391 340

Dr. Y.K. Bhateshvar
Faculty - Automotive Research Association of India. Survey No. 102, Vetal Hill, off Paud Road, Kothrud, Pune - 411 038

Mr. A. A. Gaikwad
Deputy General Manager - Automotive Research Association of India. Survey No. 102, Vetal Hill, off Paud Road, Kothrud, Pune - 411 038

Mr. Alok Jaitley
Senior Vice President - Maruti Suzuki India Ltd., 1, Nelson Mandela Road, Vasant Kunj, New Delhi - 110070 India

Mr. Alok Sethi
General Manager – Transportation Technology Solutions - Delhi Integrated Multi Modal Transit System Ltd (DIMTS). 8th Floor, Block-1, Delhi Technology Park, Shastri Park, Delhi-110053

Mr. Arun Komawar
Consultant - Pune, Maharashtra, India

Mr. Ashwin Subramanian
Dy. General Manager - Automotive Research Association of India. Survey No. 102, Vetal Hill, off Paud Road, Kothrud, Pune - 411 038

Mr. Atul Pol
Program Manager - Tata Technologies. Plot No 25, Phase 1, Hinjewadi Rajiv Gandhi Infotech Park, Hinjawadi, Pune, Maharashtra 411057

Mr. Ayush Maheshwari
Researcher (Automotive System Design) - Akar International. Singapore

Mr. Devendra Mandke
Technical Specialist - JOHN DEERE INDIA PRIVATE LIMITED. Tower 14, Cybercity, Magarpatta City, Hadapsar, Pune - 411013, Maharashtra, India

Mr. Karthik Kaliappan
Sr. Manager- Product Safety and Compliance, Standards - John Deere Equip. Pvt. Ltd. Shikrapur, Sanaswadi, Maharashtra 412208

Mr. M K Chaudhari
Consultant - Pune, Maharashtra, India

Mr. Mahadevan Pichandi
Domain Head – Chassis Engineering & Vehicle Dynamics (AGM-PD), LCV Division - Ashok Leyland Limited. No.1, Sardar Patel Road, Guindy, Chennai – 600 032.

Mr. Mahesh Masurkar
Chief Manager - Embedded Software Development - John Deere India Pvt Ltd. Tower 14, Cybercity, Magarpatta City, Hadapsar, Pune - 411013, Maharashtra, India

Mr. Mouqtik Bawase
General Manager - Automotive Research Association of India. Survey No. 102, Vetal Hill, off Paud Road, Kothrud, Pune - 411 038

Mr. P. R. Pawar
General Manager - Automotive Research Association of India. Survey No. 102, Vetal Hill, off Paud Road, Kothrud, Pune - 411 038

Mr. Pradeep Chandrasekaran
Associate Director - Ola Electric Mobility Pvt. Ltd. Bangalore, Karnataka, India

Mr. Prakash V. Sardesai
Head, Application Engg & Business Development - Sud-chemie-India-Pvt Ltd. A-1/2/3, Nandesari Industrial Developmental Area, P.O. Nandesari, Vadodara district, Gujarat 391 340

Mr. Prashant Mahale
Asst. General Manager - Fiat Chrysler. 1601 (III), 16th Floor, B Wing, The Capital, Plot #C-70, G Block, Bandra Kurla Complex, Bandra (East), Mumbai 400 051, India.

Mr. R M Cursetji
Head-Technology Department - Sud Chemie India Pvt. Ltd. A-1/2/3, Nandesari Industrial Developmental Area, P.O. Nandesari, Vadodara district, Gujarat 391 340

Mr. Rahul Mahajan
Deputy Director - Automotive Research Association of India. Survey No. 102, Vetal Hill, off Paud Road, Kothrud, Pune - 411 038

Mr. S Bhattacharya
Director - Technical Sales - Huegli Tech AG Switzerland. Pune, Maharashtra, India

Mr. S R Marathe
Engineering Consultant - Pune, Maharashtra, India

Mr. S. B. Sonawane
Manager - Automotive Research Association of India. Survey No. 102, Vetal Hill, off Paud Road, Kothrud, Pune - 411 038

Mr. Sanjay Deshpande
Vice President - Mahindra & Mahindra. Nasik, Maharashtra, India

Mr. Srinivasan Raju
Automotive Consultant - Pune, Maharashtra, India

Mr. Swarupanand Sewalkar
Sr. Technology Lead - JOHN DEERE INDIA PRIVATE LIMITED. Pune, Maharashtra, India

Mr. T.C. Kamath
Deputy General Manager-Design Standards - MRF Limited. Chennai, Tamil Nadu, India

Mr. Vikram A. Tandon
General Manager - Automotive Research Association of India. Survey No. 102, Vetal Hill, off Paud Road, Kothrud, Pune - 411 038

Mr. Vinay Mundada
Consultant - Pune, Maharashtra, India

Mr. Vinit Jawale
Systems Engineering Leader - JOHN DEERE INDIA PRIVATE LIMITED. Tower 14, Cybercity, Magarpatta City, Hadapsar, Pune - 411013, Maharashtra, India

Mr. Yogesh Thipse
General Manager - Automotive Research Association of India. Survey No. 102, Vetal Hill, off Paud Road, Kothrud, Pune - 411 038

Mr. Z. A. Mujawar
Consultant - Pune, Maharashtra, India

Mrs. Beena Sandeep Limkar
Assistant Professor - Savitribai Phule Pune University. Department of Technology, Pune, Maharashtra, India

Mrs. Swati Athavale
Engineering Consultant - Pune, Maharashtra, India

Ms. Jyoti Kirve
General Manager - Automotive Research Association of India. Survey No. 102, Vetal Hill, off Paud Road, Kothrud, Pune - 411 038

ABOUT THE JOURNAL

ARAI Journal of Mobility Technology is a print and online technical journal dedicated to automotive and related fields. This publication is a collaboration between ARAI and BSP Books Pvt. Ltd., Hyderabad. It is a quarterly publication that covers automotive and related topics. Its main goal is to meet the needs of professionals, academia, and industry, as well as to further the dissemination of original research in all fields of automotive technology. One of the objectives of this journal is to provide a platform for the publication of articles on a variety of automotive and related topics. A manuscript published in this journal will receive a lot of attention and acquire a very high reputation in the automotive and research communities.

Papers: This journal seeks high-quality research papers/articles for upcoming issues from academic and industry scholars, academicians, and automotive professionals. Manuscripts of sufficient quality that are relevant to the objectives and scope of the AJMT will be reviewed.

Paper Type:

Research Papers: They should include a hypothesis, a background study, methods, results, an interpretation of the findings, and a discussion of the potential implications.

Review Papers: They should provide a critical and constructive analysis of existing published literature in a field via summary, analysis, and comparison, frequently identifying specific gaps or problems and providing recommendations for future research.

Subscriptions: Subscribers will receive four print copies annually as well as immediate access to the online journal, including full online access to all current and back articles.

Degree offering Colleges / University: Rs. 5000/- yearly subscription for print & online access.

Corporate / Individual / R&D Institute / Government Institute: Rs. 8000/- yearly subscription for print & online access.

For more information, please visit our journal's website at https://araijournal.com/index.php/arai/index

PUBLISHING PARTNER
BSP Books Pvt. Ltd., Hyderabad.
4-4-309, Giriraj Lane, Sultan Bazar,
Hyderabad 500 095, Telangana.

PUBLISHING COORDINATORS
1. Dr. A. Madhava Rao, ARAI, Pune.
2. Mr. Nikunjesh Shah, BSP Books, Hyderabad.
3. Mr. Naresh Davergave, BSP Books, Hyderabad.

ARAI Journal of Mobility Technology

ARAI J. Mobi. Tech (AJMT); *Online Access & Print Journal*

https://araijournal.com

DISCLAIMER

DECLARATION

(a) Name of the Publisher and Printer	The Automotive Research Association of India
(b) Printing Press with Address	Aditya offset Process (I) Pvt. Ltd. H.No:- # 3-1/7, Survey No.56/1, Jalapally Village, Saroornagar Mandal, Ranga Reddy Dist. Hyderabad 500005.
(c) Place of Publication with Address	Survey No. 102, Vetal Hill, off Paud Road, Kothrud, Pune - 411 038 P. B. No. 832, Pune - 411 004
(d) Name of the Editor-in-Chief	**Dr. Sukrut S. Thipse** Sr. Deputy Director ARAI, Pune

For Manuscript Submission

Dr. A. Madhava Rao (Assistant Editor)
Manager, ARAI, Pune
Email: madhavrao.lib@araiindia.com

For Subscription

Mr. Nikunjesh Shah (Marketing Head)
BSP Books Pvt. Ltd., Hyderabad
E-mail: nikunjesh.shah@bspbooks.net

ARAI Journal of Mobility Technology

A Quarterly Peer-Reviewed Journal

CONTENTS

Research Papers

ARAI Journal of Mobility Technology
Volume 2 • Issue 2 • April–June, 2022, pp. 169-174
Research Paper
https://doi.org/10.37285/ajmt.1.2.1

Bilateral Facet Dislocations With and Without Head Impact Sustained by Restrained Occupants

Chandrashekhar K. Thorbole

Thorbole Simulation Technologies, LLC, 2524 Horizon Blvd. Rogers, Arkansas - 72758, USA

ABSTRACT

This paper aims to understand the different injury mechanism involved with traumatic Bilateral Facet Dislocation (BFD) and fracture of the cervical spine. The intent is to demonstrate and elucidate tensile and compression induced injury mechanisms producing BFD by employing real-world crash investigations in association with all the past laboratory testing and studies done by numerous researchers. The study indicates that in a frontal crash scenario, maintaining the position of the shoulder belt is paramount, and any migration towards the base of the neck allows the fulcrum formation that amplifies distractive moments on the neck producing BFD. Similarly, in a rollover crash scenario, roof intrusion magnitude, and its rate along with roof deformation pattern can impose a rotational constraint on the head and plays a vital role in producing BFD. Roof design must address the formation of pocketing in the roof due to deformations imposing rotational head constraint exposing neck to buckling and subsequent BFD as the roof intrusion continues.

KEYWORDS: Frontal crash scenario, Human cervical spine, Bilateral Facet Dislocation (BFD), Head impact, Rollover crash scenario, Zygapophysial joints, Neural arch, Safety.

Introduction

The human cervical spine consists of seven vertebrae interconnected by articulating joints and tissues supporting the human head. Facet joints, also known as Zygapophysial joints, can be best visualized from the side laterally. The neural arch (dorsal part) of typical vertebrae supports seven processes: four articular processes, two transverse processes, and one spinous process. The superior and inferior articular process on each side forms an articular pillar. The articulating joints between these pillars are called facet joints. The articulating surfaces of these pillars are at an angle steeper in the upper region than in the lower region. Figure 1 shows the side view of the cervical spine highlighting the facets joints and pillars, forming articulating joints of the cervical spine.

The facet dislocation injury pattern typically involves upper superior vertebral body displacement relative to the inferior vertebral body, mostly in the forward direction. The anterior displacement disrupts ligaments and locking of facet surfaces, significantly reducing the spinal canal's anteroposterior diameter. Figure 2 shows the schematics of facet dislocation at the C5-C6 level that compares normal with the dislocated condition. Facet dislocation with fracture mainly of the facet or lamina is termed as Facet fracture-dislocation. The dislocation injury produces devastating outcomes due to sever dynamic cord compression at the instant of dislocation injury. Figure 3 shows the schematics of cord injury due to facet dislocation. This paper focuses on neck injuries involving spinal cord mainly produced by facet dislocations with or without fracture. The vehicle kinematics and structural deformations govern the restrained occupant kinematics during a collision. Furthermore, the head and neck kinematics of a restrained occupant is modulated by several factors such as crash type, restraint performance, and compartment intrusions. This paper describes real-world frontal and rollover crashes to elucidate the role of head and neck kinematics with and without compartment intrusion in producing BFD at C5-C6 level inducing spinal cord injury. Mechanistic classification by Allen Jr et al. [1] for the lower cervical spine injury and dislocation is based on the mechanism of injuries such as compression-flexion, vertical compression, distractive-flexion, and other combinations.

The motivation of this paper is to demonstrate using real-world frontal and rollover crash about the production of BFD injury with different injury mechanism. In doing so, the study will demonstrate the concomitant injuries that accompany the BFD injury mechanism and facilitate differentiating the injury mechanism producing similar C5-C6 BFD injury patterns.

ABBREVIATIONS: BFD - Bilateral Facet Dislocation; GCS - Glasgow Coma Scale; CT - Computerized Tomography; MRI - Magnetic Resonance Imaging; EMS - Emergency Medical Services; A.S.I. S - Anterior Superior Iliac Spine

Fig. 1. Schematic of cervical spine from side showing facet joints and pillars.

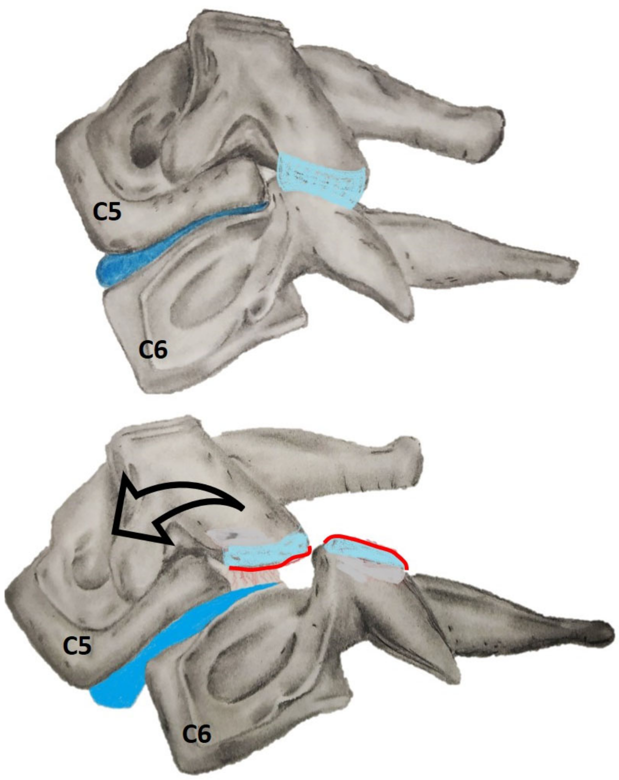

Fig. 2. Schematics of Facet dislocation at C5-C6.

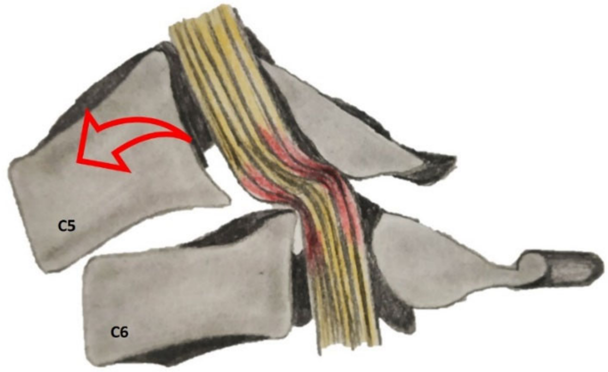

Fig. 3. Schematics of cord injury due to canal narrowing at the instant of dislocation.

Method

In this study, the field crash investigations conducted by the author on the selected matter are presented to elucidate more on facet dislocation and fracture injury mechanism under different loading conditions. The selected case matter involved a frontal and a rollover crash. The case selection criteria for the frontal crash involved the following.

1. Presence of cervical cord injury at the dislocation level.
2. Anterolisthesis of C5 over C6.
3. Ligamentous disruption at the injury level.
4. Concomitant cerebrovascular injury at the injury level.
5. Properly restrained occupants at the time of collision.
6. No external or internal head or face injury.
7. No structural intrusion at the location of the subject occupant.

Similarly, for the rollover crash the selection criteria was the following.

1. Presence of cervical cord injury at the dislocation level.
2. Anterolisthesis of C5 over C6.
3. Ligamentous disruption at the injury level.
4. Concomitant cerebrovascular injury at the injury level.
5. Properly restrained occupants at the time of collision.
6. Presence of head injury.
7. Significant roof intrusion into the survival space.

Frontal Crash Case Report with C5-C6 BFD

The crash involves a 30-year-old female who was the left rear belted passenger of a four-door sedan. She weighed 72.5 Kg (160 lbs.) at the time and is 170.18 cm (~5ft 7 in) in height.

At the crash scene, she was alert and oriented to person, place, and event with her GCS (Glass glow coma scale) of 13. Her physical assessment at the scene showed abrasion to both hips, abrasion, and avulsion to her left neck and chest area with no other visible injury. She complained about abdominal pain and complete numbness in all four extremities. The vehicle inspection showed that the vehicle's damage was limited to the frontal body, with almost no intrusion into the front occupant's survival space.

Figure 4 shows the damage pattern on the vehicle. The vehicle EDR data recorded 39.0 mph as longitudinal Delta-V in 100 ms and 6.2 mph for lateral Delta-V. All available frontal airbags for the driver and the front passenger also deployed along with the driver side curtain airbag and the driver seat-mounted thorax airbag.

The inspection of left rear seatbelt webbing and the hardware showed load marks consistent with proper use of the seatbelt. Furthermore, the fat stranding analysis using CT (Computed tomography) imaging scans of pelvis and abdomen indicates proper placement of the lap belt before the crash.

Figure 5 shows the fat stranding at the ASIS (anterior superior iliac spine) due to lap belt loading during the subject frontal crash. Figure 6 shows the shoulder belt loading marks on the body near the base of the neck on the left. Figure 7 shows the C5-C6 dislocation pattern that involves bilateral facet dislocation with the widening of posterior disc space and interspinous space with disruption of the disc. The imaging studies also revealed cerebrovascular injury at the dislocation level.

Fig. 4. Exterior damage pattern on the vehicle.

Fig. 5. Fat stranding as visible on the CT abdomen at A.S.I.S level.

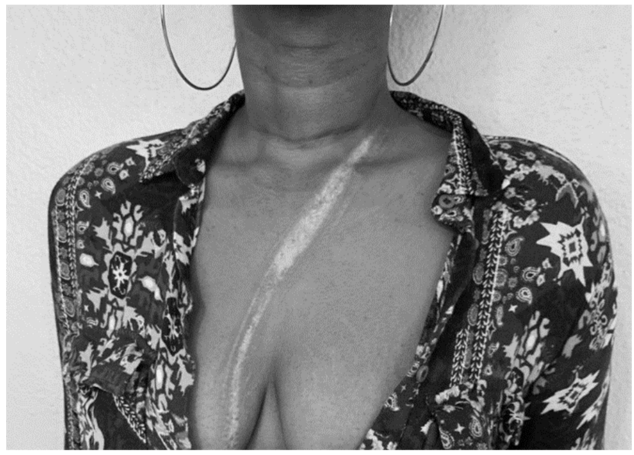

Fig. 6. Shoulder belt injury marks.

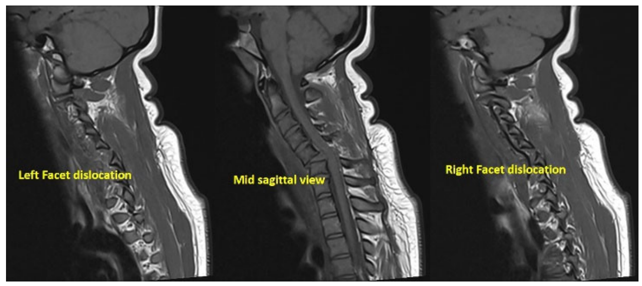

Fig. 7. C5-C6 level dislocation with ligamentous injury occurred in the frontal crash.

Rollover Crash Case Report with C5-C6 BFD

The crash involves a 22-year-old female who was the front belted passenger of a four-door sedan. She weighed 74.8 Kg (165 lbs.) at the time and is 172.7 cm (~5ft 8 in) in height. At the crash scene based on EMS records, she was alert and oriented to person, place, and event with her GCS (Glass glow coma scale) of 15. The CT and MRI studies at the hospital showed C5-C6 level BFD with 3-column injury and severe compression of the cervical cord.

She was unable to move or feel anything below her upper chest at the scene. She also sustained an acute bilateral traumatic cerebrovascular injury at the dislocation level. The imaging studies also showed the scalp head injury with no underlying skull fracture.

Figure 8 shows the roof crush profile of the vehicle from outside and inside. Figure 9 shows the hair deposit on the roof substrate, as observed during the vehicle inspection. Figure 10 shows the local roof deformation pattern from inside above the occupant's head.

The belt inspection shows consistent load marks on the webbing and the hardware confirming the proper use of the seatbelt. Figure 11 shows the head scan that shows the location of scalp hematoma on her head.

Figure 12 shows the MRI scan of her neck, showing severe canal stenosis at C5-C6 level due to BFD.

The vehicle rolled the driver's side, making the subject front passenger a far side occupant. Accident reconstruction shows four quarter turns (one complete rotation) driver side with tripping mechanism. The vehicle was found on its all four wheels at its rest position.

Fig. 8. Vehicle roof crush profile.

Fig. 9. Hair deposit on the interior roof substrate above occupant's head.

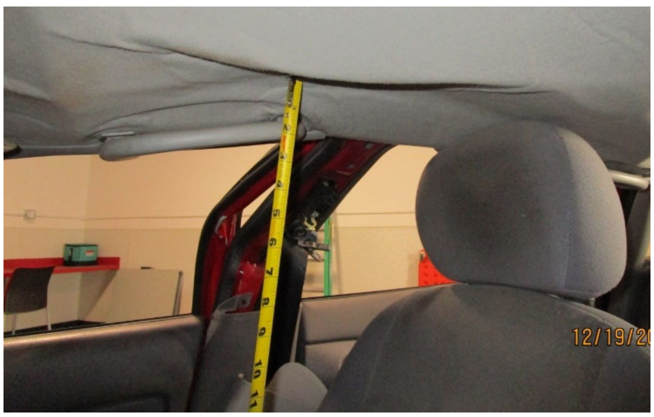

Fig. 10. Roof deformation pattern above the occupant's head.

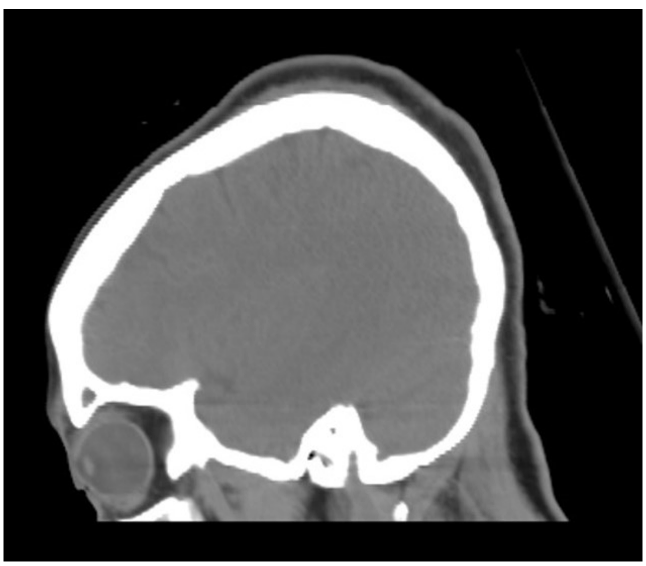

Fig. 11. Location of subcutaneous hematoma over the head.

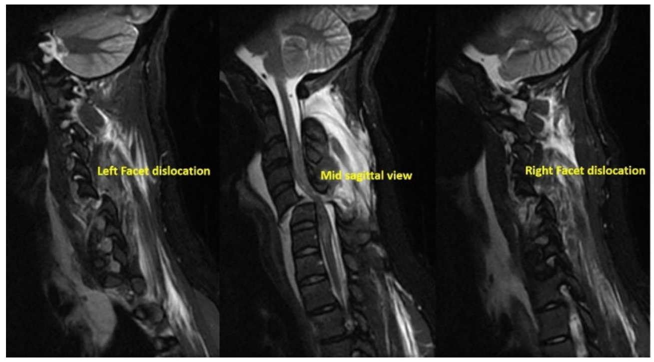

Fig. 12. C5-C6 level dislocation with ligamentous injury occurred in the rollover crash.

Discussion

BFD (Bilateral facet dislocation) produces a narrowing of the spinal canal as the superior vertebrae move anteriorly relative to the inferior vertebrae [1,2]. The spinal cord is subjected to a high rate dynamic pinching produced at the instant of dislocation [3,4]. In this study, two different crash modes resulting in entirely different overall occupant kinematics produced cervical spine BFD with spinal cord injury. In the frontal crash scenario, the neck tensile loading, and the rollover crash, the compressive neck loading superimposed with neck moments resulted in injury-producing facet joint kinematics. The current study aims to elucidate facet joint kinematics using real-world traffic crashes and laboratory testing as done in the past.

In the frontal crash scenario, based on the injury diagnosis and vehicle inspection, no evidence of head impact is available. The BFD produced is entirely due to the inertial loading of the neck exerted by the mass of the occupant's head. Punjabi et al. [5] conducted a laboratory experiment to quantify facet joint kinematics in a high-speed frontal loading condition. The experiment employed a bench-top sled to produce frontal impact decelerations of the FSU (Functional Spinal Units) mounted on the sled. The mass attached to the superior vertebrae of the FSU produced inertial forces and moments modulated by the sled deceleration severity. The high loading rate testing showed that facet joints separate first with significantly higher separation at the posterior edge of the facet compared to the anterior. Followed by peak flexion rotation and facet forward sliding occurred. The CT and MRI imaging confirms the kinematics, as observed by Punjabi et al. in their testing. The final rest position of the C5 inferior facets and widening of the posterior disc space and interspinous space validates the kinematic observations made by Punjabi et al. in their experiment. Flexion-distraction loading pattern produces BFD in the frontal crash scenario.

Several studies from the past explain BFD injuries to occupants in the absence of any head impact during the frontal crash. Shanahan Dennis [6], in his research paper based on real-world crash analysis, reported seven cases involving neck fractures and dislocations in the frontal crash scenario. According to this study, the impingement of the shoulder belt near the neck during the frontal crash amplifies forces on the spine. The study further states that the belt creates a fulcrum over which the neck flexes. Smith et al. [7] explain the amplification of moments due to belt fulcrum formation that shifts the center of rotation forward, producing injuries. Huelke et al. [8] reported several cases with neck fracture-dislocation in a frontal crash without any head impacts. Furthermore, they noted no correlation between neck injury and crash severity when an injury occurs without any head impact.

This conclusion supports observations of Shanahan regarding the amplification of forces and moments due to belt fulcrum about which the neck flexes. Moreover, the author of this paper has investigated low severity frontal crash with delta V less 20mph producing BFD with spinal cord injury for front passenger further supporting the conclusions drawn by Huelke and Shanahan.

In the rollover crash scenario, the overall body kinematics are significantly different compared to a frontal crash. The loading on the head from the roof structure mainly modulates the neck kinematics.

The neck is predominantly acted upon by the compressive load as opposed to tensile, as observed in the frontal crash without head impact. Despite compressive loading, the second case's neck injury pattern is like the first case with some minor difference. It has been shown by various researchers employing laboratory testing in the past that compressive load on the head and neck complex producing BFD injury pattern. Factors such as neck orientation, location of blunt impact on top of the head, padding, and head constraint boundary conditions have been shown to modulate the neck injury pattern [9,10]. Bauze et al. [11] may be the first ones to produce a BFD injury pattern in the laboratory while applying compressive loading on the cervical spine while the head was constrained such that its rotation was restricted. Hodgson et al. [12], in their laboratory testing's with rotationally constrained helmeted heads, showed cervical spine buckling after head crown impacts.

Nightingale et al. [13] imposed several end conditions to the cervical spine to understand failure modes under compressive loading. The study showed that with rotational constraint alone, all specimens produced BFD. All the past research points to rotational constraints of the head as a significant factor in BFD production under compressive. The head rotational constraint produces buckling kinematics that positions and orients some regions of the cervical vertebrae to flex and extend.

While buckling is not injury, but the buckled spine can lead to compression-flexion or compression-extension type of injury with a continued increase in load. Henceforth, any surface capable of producing such end conditions due to its deformation and failure patterns is highly likely to produce BFD under compressive loading. In the second case study involving the rollover crash, the medical evidence of scalp hematoma shows the traumatic force acting on the head near the crown.

Furthermore, the vehicle roof's failure pattern shows the pocketing effects in the headliner substrate, confirming head rotational constraint produced by the roof. The roof intrusion caused a traumatic head impact near the crown while the head is rotationally constrained produced BFD.

The detailed knowledge of the injury mechanism facilitates a crucial understanding of the design requirements to eliminate design induced hazards. The two case studies in association with all the laboratory testing's done in the past by numerous researchers show the importance of boundary conditions imposed on the head and neck modulating the neck injury pattern.

In the frontal crash scenario, the shoulder belt migration near the base of the neck and acting as a fulcrum imposes constraints and kinematics capable of producing BFD and cord injury, and hence, it must be a vital restraint design performance criteria.

Occupant submarining on the seat causes the seatbelt migrations from the stronger skeletal sites to the undesirable sites such as the abdomen and the neck [14,15,16,17]. Hence, to eliminate the BFD injury risk due to the belt fulcrum formation in a frontal crash, it is reasonable to implement a restraint design that prevents occupant submarining.

Similarly, in the rollover crash scenario, the roof high rate intrusion and the roof's capability to impose head rotational constraint must be eliminated to design out the hazard of severe neck BFD injury. The alternative designs that prevent submarining or roof designs maintaining structural integrity are not the focus of this paper. However, the study focuses on the conditions required to produce BFD in frontal and rollover crashes, which have been discussed using real-world examples.

Conclusion

Two real-world investigations are presented involving traumatic BFD at the C5-C6 level. In the frontal crash scenario, the shoulder belt transition towards the base of the neck and forming a fulcrum amplifying force and moments above the level of the fulcrum produced BFD at the C5-C6 level. In the rollover crash scenario, the head's traumatic impact from the intruding roof buckled the cervical spine and exposed it to BFD at the C5-C6 under continued increasing load from the roof. In both the crashes, the occupants sustained cervical cord injury. The case studies in association with all the laboratory testing by numerous researchers in the past confirm that tensile or compressive loading of the cervical spine under certain conditions produce BFD. Furthermore, in the absence of any information about the related accidents, the presence and absence of head injury play a vital role in describing the mechanism that produced BFD.

In the frontal crash scenario, the amplification of loading due to the belt fulcrum point formation produces vertebrae kinematics as required to cause BFD. The vertebral body kinematics has been produced in the laboratory in the past. In the rollover crash scenario, the roof intrusion and local deformation pattern of the roof produce rotational constraint of the head causing buckling of the cervical spine followed by BFD as the load continues to increase on the head from the intruding roof. The buckling of the cervical spine has been produced in the laboratory and provides excellent details of explanation regarding the neck injury sustained in the rollover case study. The concomitant scalp hematoma and the hair deposit found on the headliner substrate confirm the roof's role in producing the BFD in a rollover crash.

The injury mechanism analysis and study are crucial for automotive passive safety. These two real-world cases, in conjunction with laboratory testing, shows that preventing occupant submarining that repositions the shoulder belt near the neck can eliminate the risk of BFD in frontal crash scenarios. Furthermore, limiting the roof intrusion and maintaining the roof structure can prevent the traumatic head impact and formation of the rotational constraint for the head, eliminating the risk of spine buckling and subsequent BFD.

References

[1] Allen Jr, B. L., R. L. Ferguson, THOMAS R. Lehmann, and R. P. O'brien. "A mechanistic classification of closed, indirect fractures and dislocations of the lower cervical spine." Spine 7, no. 1 (1982): 1-27. https://pubmed.ncbi.nlm.nih.gov/7071658/

[2] Daffner, Scott D., and Richard H. Daffner. "Computed tomography diagnosis of facet dislocations: the “hamburger bun” and “reverse hamburger bun” signs." The Journal of emergency medicine 23, no. 4 (2002): 387-394. https://pubmed.ncbi.nlm.nih.gov/12480021/

[3] Ivancic, Paul C., Manohar M. Panjabi, Yasuhiro Tominaga, Adam M. Pearson, S. Elena Gimenez, and Travis G. Maak. "Spinal canal narrowing during simulated frontal impact." European spine journal 15, no. 6 (2006): 891-901. https://pubmed.ncbi.nlm.nih.gov/16220351/

[4] Ivancic, Paul C., Adam M. Pearson, Yasuhiro Tominaga, Andrew K. Simpson, James J. Yue, and Manohar M. Panjabi. "Mechanism of cervical spinal cord injury during bilateral facet dislocation." Spine 32, no. 22 (2007): 2467-2473. https://pubmed.ncbi.nlm.nih.gov/18090087/

[5] Gomes, Shanda, Scott Rudkin, Fong Tsai, and Shahram Lotfipour. "Bilateral cervical spine facet fracture-dislocation." The western journal of emergency medicine 10, no. 1 (2009): 19. https://www.ncbi.nlm.nih.gov/pmc/articles/PMC2672293/

[6] Panjabi, Manohar M., Andrew K. Simpson, Paul C. Ivancic, Adam M. Pearson, Yasuhiro Tominaga, and James J. Yue. "Cervical facet joint kinematics during bilateral facet dislocation." European Spine Journal 16, no. 10 (2007): 1680-1688. https://www.ncbi.nlm.nih.gov/pmc/articles/PMC2078308/

[7] Shanahan, Dennis F. "Shoulder belt-induced flexion–distraction fractures of the cervical spine." International Journal of Crashworthiness 18, no. 6 (2013): 559-569.[https://www.tandfonline.com/doi/abs/10.1080/13588265.2013.825387

[8] Smith, William S., and Herbert Kaufer. "Patterns and mechanisms of lumbar injuries associated with lap seat belts." JBJS 51, no. 2 (1969): 239-254. https://pubmed.ncbi.nlm.nih.gov/5767317/

[9] Huelke, Donald F., G. Murray Mackay, Andrew Morris, and Maureen Bradford. "A review of cervical fractures and fracture-dislocations without head impacts sustained by restrained occupants." Accident Analysis & Prevention 25, no. 6 (1993): 731-743. https://pubmed.ncbi.nlm.nih.gov/8297440/

[10] Nusholtz, Guy S., D. E. Huelke, P. Lux, Nabih M. Alem, and F. Montalvo. Cervical spine injury mechanisms. No. 831616. SAE Technical Paper, 1983.[https://www.sae.org/publications/technical-papers/content/831616/

[11] Nightingale, Roger W., William J. Richardson, and Barry S. Myers. "The effects of padded surfaces on the risk for cervical spine injury." Spine 22, no. 20 (1997): 2380-2387. https://pubmed.ncbi.nlm.nih.gov/9355219/

[12] Bauze, ROBERT J., and Gordon M. Ardran. "Experimental production of forward dislocation in the human cervical spine." The Journal of bone and joint surgery. British volume 60, no. 2 (1978): 239-245. [https://pubmed.ncbi.nlm.nih.gov/659473/]

[13] Hodgson, Voigt R., and L. Murray Thomas. "Mechanisms of cervical spine injury during impact to the protected head." SAE Transactions (1980): 3792-3805. https://www.sae.org/publications/technical-papers/content/801300/

[14] Nightingale, Roger W., James H. McElhaney, Daniel L. Camacho, Michael Kleinberger, Beth A. Winkelstein, and Barry S. Myers. "The dynamic responses of the cervical spine: buckling, end conditions, and tolerance in compressive impacts." SAE transactions (1997): 3968-3988. https://www.sae.org/publications/technicalpapers/content/973344/

[15] Adomeit, Dieter, and Alfred Heger. "Motion sequence criteria and design proposals for restraint devices in order to avoid unfavorable biomechanic conditions and submarining." SAE Transactions (1975): 3150-3159. https://www.sae.org/publications/technicalpapers/content/751146/

[16] Thorbole, Chandrashekhar K. "Seatbelt submarining injury and its prevention countermeasures: How a cantilever seat pan structure exacerbates submarining." Journal of family medicine and primary care 4, no. 4 (2015): 587. https://pubmed.ncbi.nlm.nih.gov/26985421/

[17] Thorbole, Chandrashekhar K., and Prashant Naik. "role of traumatic seatbelt fat stranding in automotive crash injury analysis." 26th ESV Conference, Eindhoven Netherlands,[https://www-esv.nhtsa.dot.gov/Proceedings/26/26ESV-000137.pdf

[18] Thorbole, Chandrashekhar K. "Dangers of seatback recline in a moving vehicle: how seatback recline increases the injury severity and shifts injury pattern." In ASME 2015 International Mechanical Engineering Congress and Exposition. American Society of Mechanical Engineers Digital Collection, 2015. https://asmedigitalcollection.asme.org/IMECE/proceedingsabstract/IMECE2015/57380/V003T03A056/264306

Address correspondence to: *Dr. Chandrashekhar K. Thorbole, Thorbole Simulation Technologies, LLC, 2524 Horizon Blvd. Rogers, Arkansas -* 72758, *USA.*
Ph: +1 (479) 466-7050
E-mail: thorsimtech@gmail.com; chandrathorbole@injurybiomechanics.com

ARAI Journal of Mobility Technology
Volume 2 • Issue 2 • April–June, 2022, pp. 175-182
Research Paper
https://doi.org/10.37285/ajmt.1.2.2

Failure Analysis of Front Axle Wheel Studs in Small Commercial Vehicles

Mahadevan Pichandi and Jagadeesh Selvaraj

Chassis Engineering - LCV PD, Ashok Leyland Technical Centre, Chennai.

ABSTRACT

Irrespective of specific applications, the Small Commercial Vehicles (SCV) are always subjected to severe working conditions, especially the front wheels experience higher loads than design intended due to higher overloading by customers, driver abuse and frequent brake applications. The front axle wheels fasten system plays a key role for safety of the vehicle and pedestrian.

The wheel separation can lead to serious injuries to passengers of the vehicle and pedestrian or from another vehicle maneuvering including fatalities. In this project investigation, the causes that promote failure of front axle wheels fasten system and subsequent wheels separation of SCV is analyzed carefully. Metallurgical analysis of the failed fasten system shows that it is characterized by a series of synergetic steps that include plastic deformation of nuts and studs caused due to disproportionate torque tightening practices. Also, the effect of other external factors that lead to deterioration of stud fatigue life such as road camber and driver abuse are analyzed. Based on this promise, the present investigation deals with detailed analysis of the root causes contributing such failures are analyzed and discussed in this paper. This study would help the fellow designers to select optimized fastening system considering all the parameters influencing wheel separation due to stud failures for SCV, passenger vehicles and heavy duty trucks.

KEYWORDS: Wheel stud failure, wheel fastener, wheel separation, deformation, fatigue life, optimized fastening system, stud clamping load, metallurgical analysis, chemical composition, microstructural analysis, fractographic analysis, hardness test, road camber, fracture surface, SEM, torsional load, tempered martensite, design load, thread section.

Introduction

The ever increasing demand for SCVs to move logistics such ecommerce goods and groceries has led to the operation of SCVs all round the clock. Revenue generation and profitabality of SCV owners have improved significantly owing to this increased running hours. It is important that safety critical components of SCVs are robust such that they ensure safety of drivers and others.

The wheel being a safety critical component, must satisfactorily perform its function for the intended design life. The design of wheels have become more complicated due to the demand for lighter weight and aesthetic wheel configuration coupled with vehicle overloading practices by the customers operating SCVs. Thus, it is paramount to perform rigorous assessment of wheel elements design on the strength and durability perspective. Strength and durability of the wheel elements are underpinned on well-designed wheel studs. Since, failure of them could cause huge risk of accidents.

The wheels poise the complete load of vehicle through vertical reaction from the road. wheel studs clamp wheel rim and hub securely with sufficient clamping load so that vertical load transfer happens from tyre through wheel rim to the hub. The wheel studs while clamping wheel rim and hub may undergoe radial load due to vertical reaction forces exerted during vehicle operation. During vehicle operation, any relaxation in clamping load on the wheel studs could them to cyclic radial loads compromising fatigue reliability of the wheel studs.

To keep up with the market trend, a new SCV with higher payload carrying capacity and superior engine was developed. In general proto build vehicles will be subjected to extensive durability trials simulating customer road and load conditions preceding to the release of production vehicles to the market. In-addition to conducting performance and endurance trials, the proto vehicle drivers would themselves do wheel retrofitments when in need using vehicle tool kit during endurance trials. The intention of this activity was to capture customer abusive behaviour on vehicles pertaining to retrofitment activities and improve design if necessary. Therefore, during the endurance trials proto vehicle drivers used wheel spanners for removing and fastening the front wheel studs without following any defined torque tightening procedure or torque wrenches.

During this extensive endurance trials, all the front axle parts were performing good except front wheel studs.Considerable number of the proto vehicles started exhibiting wheel stud failures only on the front RHS wheels (Right Hand Side of vehicle) after covering 70,000km in Highway as shown in Figure 1. Details of the failures are shown in Table.1

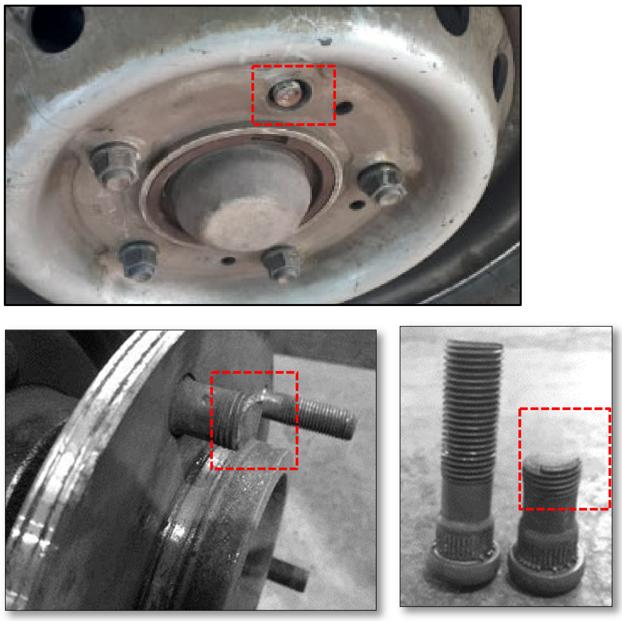

Fig. 1. Photographs of wheel stud failures.

The authors in this paper had attempted to analyse the causes that promoted the failure of front axle RHS wheel studs and proposed a solution that would be useful for the fellow design engineers to select an optimized fastening system for the wheel elements.

TABLE 1

Proto vehicle wheel stud failure km status

Sl. No.	Vehicles	Application	Failure km	REMARKS
1	Proto Vehicle - 01	Highway	71522	1 RHS wheel stud got failed
2	Proto Vehicle - 02	Highway	72435	1 RHS wheel stud got failed
3	Proto Vehicle - 03	Highway	82289	1 RHS wheel stud got failed

As a primary step, visual inspection of the failed wheel studs was done to understand the mode of failure. Design calculations were revisited to check for any fallacy in design. Since the effect of road camber on load acting on the wheel studs were overlooked during the initial phase of design, it was done to understand its consequences on the wheel stud loads. A metallurgical analysis viz. Chemical composition study, Microstructural analysis, Fractographic analysis and hardness test were conducted on the failed samples to get clear picture on the failure and to propose a design solution. Finally, the proposed design solution was validated through bench level and vehicle level tests to proceed for implementation.

Visual Inspection

As a part of failure study, the failed sections of the failed hub studs shown in Figure. 2 were visually inspected.

Figure. 2 (a) & (f) confirms that, the failure has happened between hub and wheel rim interface joints. Figure.2 (b) shows the grade identity of 10.9 on wheel stud which confirms to the specification. The failure mode is not obvious in Figure.2 (c) & (e). The section in Figure.2(d) reveals fatigue mode of failure.

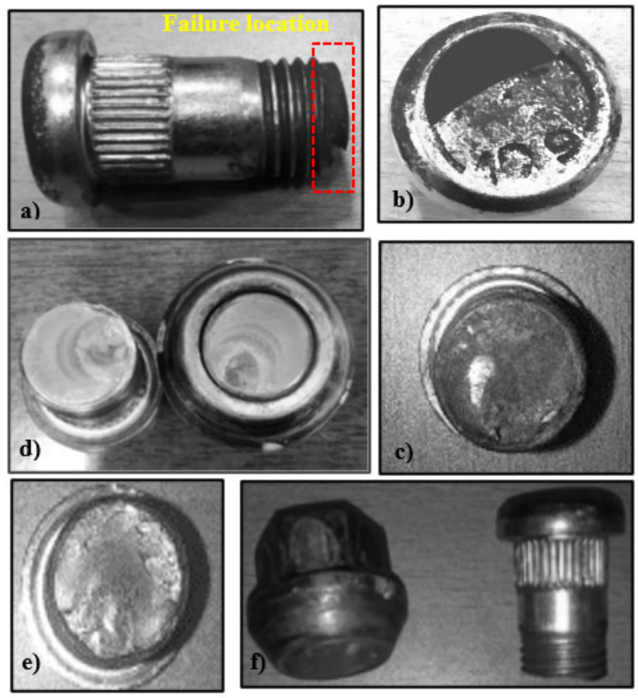

Fig. 2. Visual Inspection of Failed Wheel Studs.

Design Calculation

During a vehicle's life cycle, the wheels are exposed to large variation in load and road conditions. The bench-marked operating load conditions were taken into account for the design calculations. For this SCV, the design calculations were considered for M14 X 1.5mm wheel stud.

$$Fv = \frac{T}{K * D}$$

$$T = Fv[(0.16 * p) + (0.58 * \mu m * d2) + (0.5 * \mu n * du)]$$

$$Fv = \frac{170000}{[(0.16 * 1.5) + (0.58 * 0.2 * 13.025) + (0.5 * 0.18 * 17.5)]}$$

$$Fv = 51kN$$

Where,

Fv - Stud clamping force;

T - Tightening torque

P - Thread pitch=1.5mm

µm – Thread friction co-efficient

µn – Under head co-efficient

d2 – major diameter

du – head diameter

For M14 × 1.5mm wheel stud, theoretical clamping load calculated was 51kN with tightening torque of 170 Nm. With five studs being used, the total clamp load of 256kN was considered to ensure the integrity between wheel rim and hub.

$$Le = \frac{(d - 0.938)^2}{(d - 0.649 * p)}$$

$$Le = \frac{(14 - 0.938)^2}{(14 - 0.649 * p)} = 13.097mm$$

$$As = 0.5 * \pi * do * Le = 273mm^2$$

$$Fs = \lambda * As = 275kN$$

$$At = \frac{\pi}{4} * do^2 = 138mm^2$$

$$\sigma = \frac{Fs}{At} = 1332Mpa$$

$$Fs\sigma = \frac{\pi * \left(\frac{d2}{2}\right)^2}{4 * 9.81} = 5227kg$$

Where,

Le – Effective length of engagement

As - Shear area

Fs – Shear force

λ – Shear strength = 675Mpa

At – Tensile stress area

do –Pitch diameter = 13.26mm

σ – Tensile stress

Fsσ – Stripping strength of stud

Influence of Road Camber on Wheel Stud Failures

Road Camber is the slope gradient of road surface set in transverse direction to discharge precipitation from the road. Camber on straight roads are provided by raising the centre of the road known as crown with respect to the road edges as shown in Figure.3. Usually slope camber of up to 3% is provided for highway roads. This camber on road surface would prevent damage of the roads due to percolation of rain water. Since left hand traffic is practised in India, the vehicles plying on the straight roads have their LHS wheels bearing more load than their RH counterpart owing to road camber. In such instance, LHS wheel studs should experience fairly higher load than its RH counterpart. This phenomenon was evaluated in FEA for road camber with 3% slope.

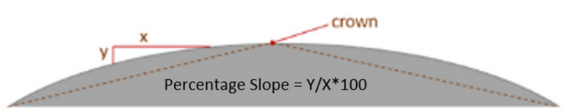

Fig. 3. Road camber.

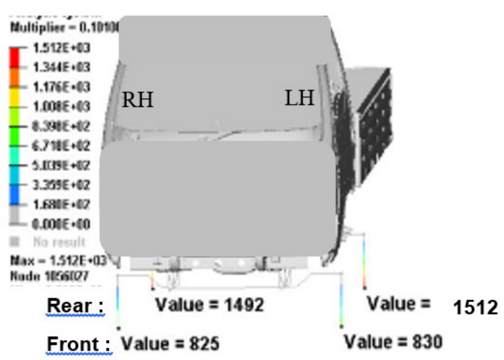

Fig. 4. Flat Road - Zero Camber (load values in kg).

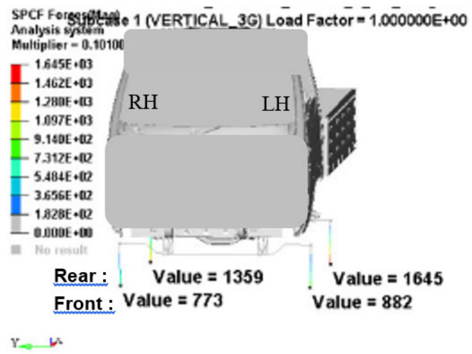

Fig. 5. LH Road Camber – 3% slope (load values in kg).

By referring Figure.4 & 5, it can be observed that due to LH road camber with slope 3%, RHS front wheel load had decreased from 825kg at Zero camber to 773kg i.e Load on RHS heel decreased by 6%. Thus road camber conditions at India have no influence on RHS wheel stud failures.

Chemical Composition Study of Failed Samples

Chemical composition analysis for a pair of failed wheel stud samples were conducted by optical emission spectroscopy. The results of which are shown in Table 2. It had been observed that the chemical composition of the failed wheel stud samples satisfies the nominal composition of steel 15B41/ Grade 10.9.

TABLE 2

Chemical Composition of Failed Samples

Description	Drawing Specification	Observation %	
		Sample 1	Sample 2
C	0.28 - 0.55	0.39	0.40
Si	-	0.22	0.21
Mn	-	1.49	1.47
S	0.045 max	0.01	0.01
P	0.040 max	0.006	0.006
Cr	-	0.12	0.12
B	-	0.003	0.003
Material Grade	STEEL PER SAE J1199 PROPERTY CLASS 10.9/15B41	Conforms to drawing specification with respect to chemical composition and hardness	Conforms to drawing specification with respect to chemical composition and hardness
Hardness (HRc)	33 - 39	34 - 37	33 - 36
Microstructure	-	Tempered martensite with no decarb on surface	Tempered martensite with no decarb on surface

Microstructural Analysis of Failed Samples

The failed samples were then subjected to metallurgical analysis to study their microstructure. The samples were prepared for inspection by various grade of SiC paper polishing under colloidal solution for refinement. Post polishing it was etched with 3% of nitric acid. With the sections in place as shown in Figure.6 the microstructural properties were analysed under optical microscopy. The corresponding microstructures were obtained in the samples. Figure.7 shows Sample-1 results, where-in the microstructure on the surface of the stud is basically tempered martensite at the case and core, no decarburization was found on the thread. It can be observed from Figure.8 that the core of the section sample-2 & 3 presents tempered martensite in core together with bainite. Microstructures indicate that hardened & tempered process were done properly.

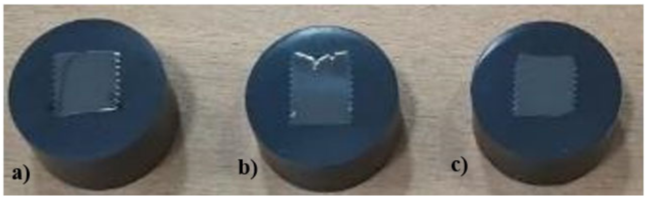

Fig. 6. Microstructure analysis – Cut Sections (a) Sample-1, (b) Sample-2, (c) Sample-3.

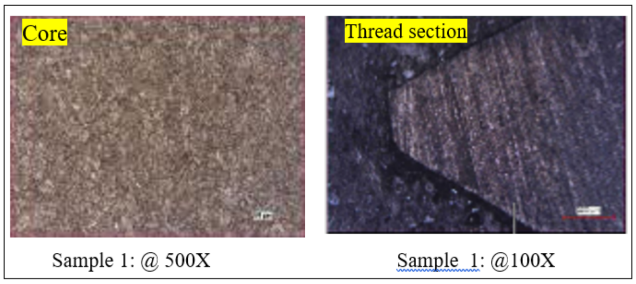

Fig. 7. Microstructure shows Tempered martensite in core & no decarb seen in thread.

No microstructure defects were found in both failed samples. Hydrogen embrittlement was not observed in all the stud samples. These test results conclude that failed stud samples are in agreement with the material specification and no abnormalities were observed.

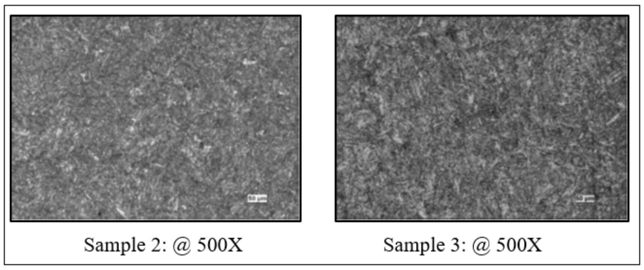

Fig. 8. Microstructure shows Tempered martensite together with bainite.

Hardness Test on Failed Samples

Hardness is defined as the resistance of the subject material to penetration by another harder material. Hardness measurements were made on segmented M14 stud specimen to determine the hardness gradient from the thread surface to the core of failed stud. The sectioning was carefully prepared using diamond disc and abundant amount of coolant were used to mitigate heat generated during cutting process. The hardness test was carried out by using Rockwell hardness tester. In Rockwell hardness test method, the hardness of the specimen was mesured by means of measured indentation depth. As shown in Figure. 9, the test specimen thickness was kept at 12 times the depth of indentation and secured on the support table. A diamond cone with 120° apical angle was used as an indenter. With the help of a handwheel, the specimen was pressed against the indenter until preliminary test force F0 of 10kgf for 3 seconds .Then an additional test force F1 of 90kgf was applied for 6 seconds. Permanent increase in depth of penetration 'e'under preliminary test force after removal of additional force was recorded. The Rockwell hardness value HRC was read from the machine directly after withdrawing force F1.

The Formula for determining Rockwell Hardness number is

$$HRc = N - e/S$$

Where,

e = Remaining indentation depth in mm

HRc = Rockwell hardness value on the C scale with diamond cone as indenter

N = Numerical value tied to S;

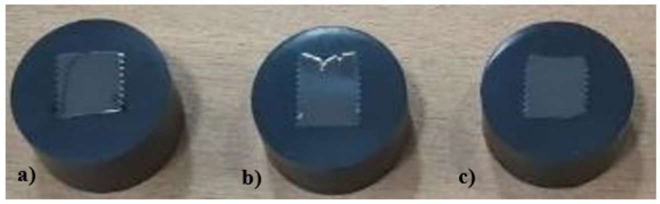

Fig. 9. Hardness Measurements - Test Specimen - Sections (a) Sample-1, (b) Sample-2, (c) Sample-3.

Multiple indentations were done at different positions at a distance of 2.5 times the indentation diameter from the test specimen edge to determine the variation in hardness from surface to the core. Core and surface hardness values were observed to be in the range from 33HRC to 37HRC which are in-line with the specification

Fractographic Analysis of Failed Samples

Fractographic analysis was carried out on three failed studs to identify the failure mode and sequence of failure. The analysis was done using Scanning Electron Microscope (SEM). Figure.10 depicts the images of areas pertaining to fracture surfaces of failed Stud sample-1. The most significant observation is that failure has initiated from thread root under torsional load. The SEM image reveals that, crack which had originated at the thread root had undergone propagation prior to final fracture. From Figure. 10, beach marks can be clearly seen indicating fatigue failure.Unsuitable wheel installation with deficient torqueing practice have allowed for the possibility of very higher preloads on the studs leading to crack intiation at thread root. This crack couldt have propagated under the influence of service loads. The slackening of the stud might have then set in allowing for unidirectional bending fatigue failure.

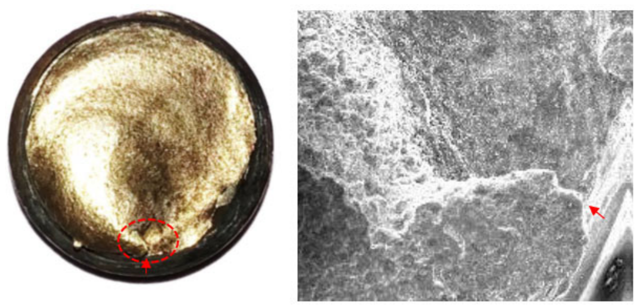

Fig. 10. Failed Stud Sample-1 & its fracture surface.

Figure 11. depicts failed stud sample-2 and fracture surface. It can be seen that mode of failure was unrecognizable by observing both failed sample and SEM

image. However this failure can be attributed to over-torqueing of studs to some extent.

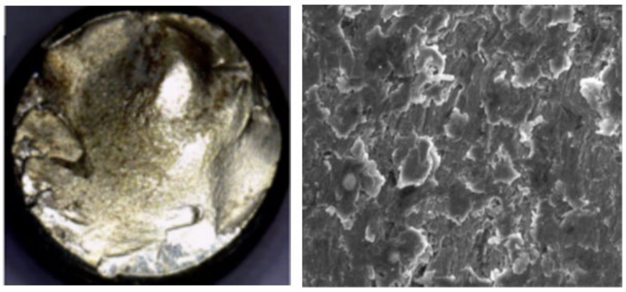

Fig. 11. Failed Stud Sample-2 & its fracture surface.

In Figure.12, failed stud sample-3 exhibits some significant results. Cracks are observed at the thread root of studs, with multiple initiation points. The adjacent SEM image corresponds to an area with the important presence of ductility fracture.

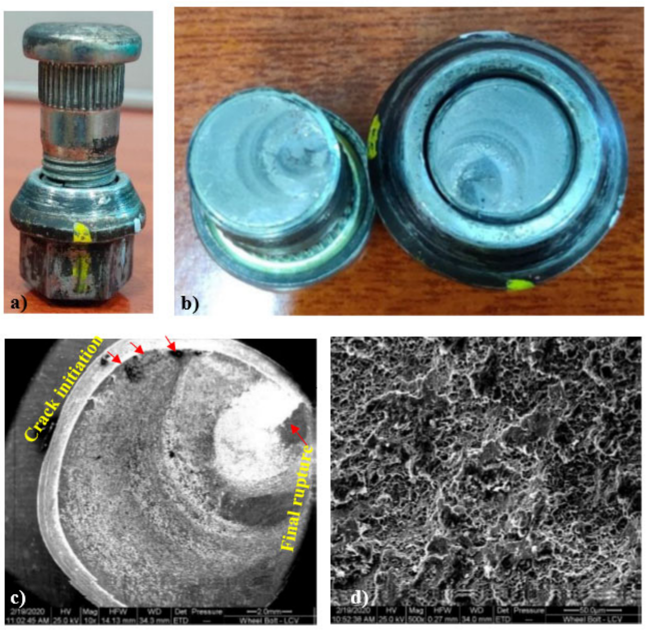

Fig.12. Failed Stud Sample-3 and its fracture surface & SEM image.

Metallurgical analysis of presented failed wheel studs reveals that all the wheel studs failed due to over tightening of wheel nuts causing too high pre-load to the wheel studs. The excessive tension in studs had resulted in yielding of the stud causing relaxation in tension. This pre-load relaxation in studs subjected them to cyclic loads during vehicle operation resulting in fatigue failure at the end. Since the design load calculations were intact, it was decided to go with a superior stud of same grade with improved fatigue properties which also should withstand the abusive torque tightening practices of the customers.

With the help of fastener suppliers and along with our Metallurgical experts opinion, M14 stud of material SAE4140, Grade 10.9 was chosen. SAE4140 wheel studs possesses improved hardenability, tougness and fatigue properties due to additional alloying of Chromium and Molybdenum as shown in Table 3.

TABLE 3
Chemical Composition comparison of SAE4140 and SAE15B41

Grade/Elements %	SAE 4140	SAE 15B41
C	0.38 / 0.43	0.35 / 0.45
Mn	0.75 / 1.00	1.25 / 1.75
Si	0.15 / 0.35	0.15 / 0.35
Cr	0.80 / 1.10	0.040 Max.
Ni	-	0.035 Max.
Mo	0.15 / 0.25	-
S	0.04 Max.	-
P	0.035 Max.	-

A comparison study on hardenibility of materials SAE15B41 and SAE4140 was made and the results were plotted as shown in Figure 13. The graph clearly shows that SAE4140 has better hardenability compared to SAE15B41 owing to its additional composition of molybdenum and chromium. Bench level tests were conducted for abusive torqueing conditions to corroborate the material analysis of SAE4140 wheel studs and are discussed futher.

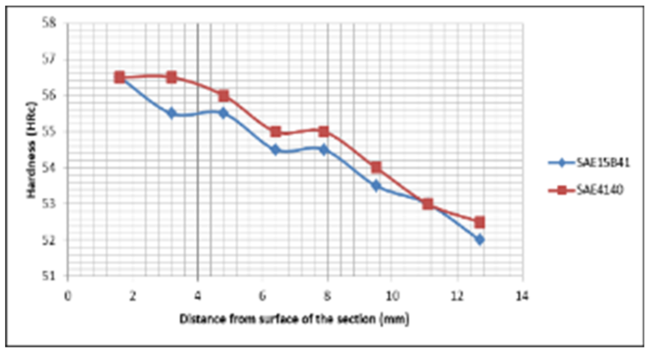

Fig. 13. Hardenability comparison of SAE4140 & SAE15B41.

Bench Level Abusive Torqueing Test on Existing - SAE15B41 and Proposed - SAE4140 Wheel Studs

The vehicle during operation are subjected for regular service tyre change, brake pad change and similar services which may lead to high torque application by the vehicle driver and service mechanic while reassembly. In order to capture this scenario, bench level abusive torqueing test was conducted on existing studs - SAE 15B41 & proposed studs – SAE4140.

Set of five new studs of material SAE 15B41 were assembled to a wheel hub. The wheel hub was then clamped tightly to a fixture table and wheel rim was carefully placed over the wheel hub with the guidance of wheel studs. Wheel nuts of grade class 10 were hand-tightened all over the studs. Using a calibrated torque wrench of capacity 980NM, torque was gradually applied over the all the nuts in clockwise sequence as shown in Figure 14(a) and the readings were noted.

Among the five studs, four were torqued until failure and one was torqued till crack initiation by gradually increasing the torque as shown in Figure 14(b). Failed studs of material - SAE 15B41 is shown in Figure.15(a),(b) & (e).

Fig. 14. Bench Level Abusive Torqueing Test: (a) Fixture setup for torque test, (b) Bolts failed due to abusive torqueing.

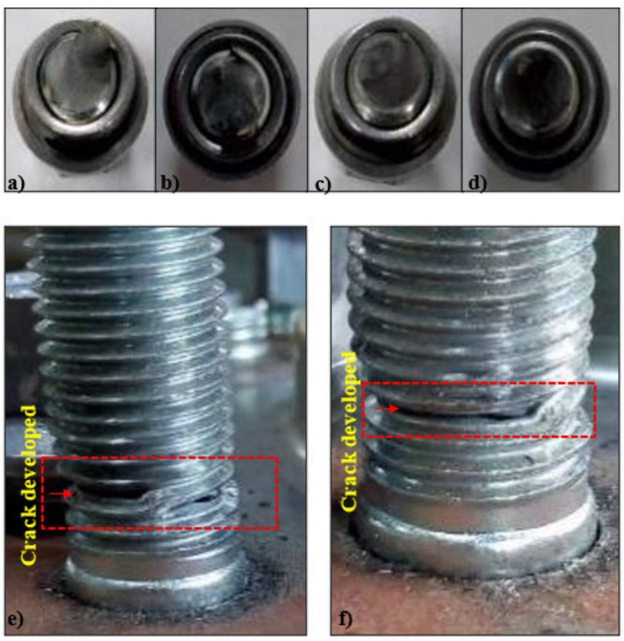

Fig. 15. Studs failed abusive torqueing test: (a),(b) &(e) – SAE 15B41; (c),(d) & (f) – SAE 4140.

The abusive torqueing test was repeated with the studs of proposed material-SAE4140 using the same setup as explained above. Failed studs of material - SAE4140 is shown in Figure.15(c),(d) & (f). By physical observation, it can confirmed that, failure have originated from the thread root under torsional load.

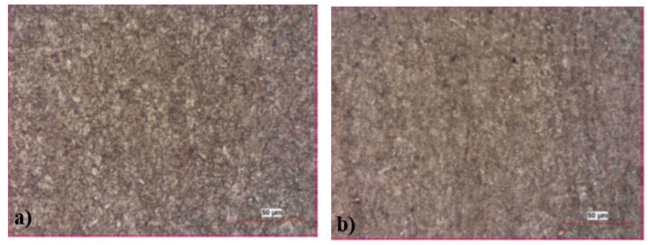

Fig.16. Microstructure analysis @500x: (a) – SAE 4140 showing tempered martensite, (b) – SAE 15B41 showing tempered martensite.

The samples failed by bench test were subjected to metallurgical and fractography analysis for study. By microstructural analysis, there observed no abnormalities in terms of decarburization or internal oxidation in both SAE5B41 & SAE4140 bolts as shown in Figure.16. The surface and core microstrures were observed to be temepered martensite.

The fractography study which is shown in Figure.17&18 reveals that, failure had been initiated from thread root and progressed towards the core section. The fracture surface reveals dimple mode failure, which indicates ductile failure by excess torsional load.

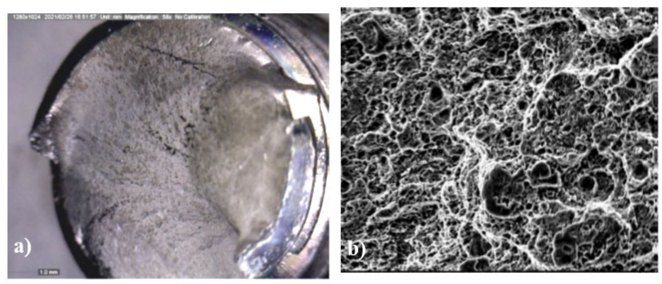

Fig. 17. Fractography analysis of SAE 4140 studs failed by bench level abusive torqueing test (a) - Dino image shows fracture surface at stud thread, (b) - SEM image @ 1000x magnification shows dimples indicating ductile mode of failure.

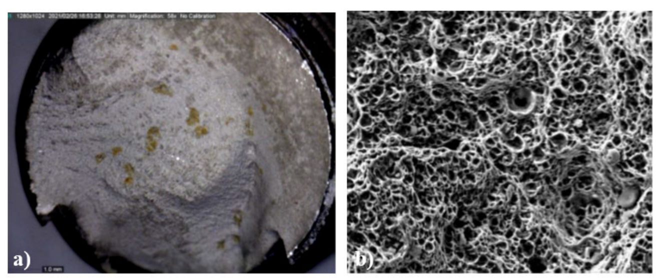

Fig. 18. Fractography analysis of SAE15B41 studs failed by bench level abusive torqueing test (a) - Dino image shows fracture surface at stud thread, (b) - SEM image @ 1000x magnification shows dimples indicating ductile mode of failure.

From abusive torqueing test, it is evident that, proposed SAE 4140 wheel stud is capable of withstanding higher abusive torque of 750Nm(avg.) than existing SAE15B41 wheel stud which was able to wtihstand only 591Nm(avg.). The comparison of abusive torque test results are in shown in Figure. 19.

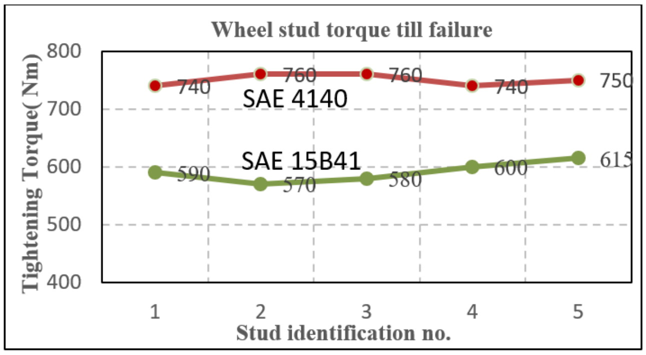

Fig. 19. Abusive torque test results comparison between SAE4140 & SAE15B1.

Vehicle Level Endurance Trials with Proposed - SAE4140 Wheel Studs

Based on the confidence from bench level tests and metallurgical analysis results, new proto-built vehicles as well as proto vehicles which had SAE15B41 wheel stud failures were assembled with proposed SAE4140 wheel studs and endurance trials were carried out. Similar to earlier validation practice, the proto vehicle drivers followed removal/refitment of front wheel studs using wheel end spanners at service intervals/as required during endurance trials. The endurance trials on the three proto vehicles (which had SAE15B41 stud failures) were stopped upon they covering 49,000 to 64,000km without any wheel stud failures since most of the other proto-built vehicles crossed highest failure km of 82,289km without any issues. More than 14,000 vehicles were sold with SAE4140 wheel studs assembled to them. Many customer vehicles have crossed 90,000km without any wheel stud failure issues. Few customer vehicles have crossed 1.2 lakh km without any front axle wheel stud failures till date as shown Table.4.

TABLE 4

Details on km coverage of few customer vehicles & proto vehicle (which had SAE15B41 stud failures) endurance trials fitted with SAE4140 wheel studs

Sl. No.	Vehicle ID	Application	Covered km	Remarks
1	Customer Vehicle - 01	Highway	119,858	As on 08.07.21 Guttapalli, AP
2	Customer Vehicle – 02	Highway	100,581	As on 10.07.21 Guntur, AP
3	Customer Vehicle - 03	Highway	94,236	As on 20.07.21 Undi, AP
4	Customer Vehicle - 03	Highway & Intracity	90,100	As on 12.07.21 Guntur, AP
5	Customer Vehicle - 04	Highway & Intracity	81,782	As on 12.07.21 Krishnagiri, TN
6	Proto Vehicle - 01	Highway	54,782	Failure - 71,522 km ODO - 126,304 km
7	Proto Vehicle - 02	Highway	49,916	Failure - 72,435 km ODO - 122,351 km
8	Proto Vehicle - 03	Highway	64,230	Failure – 82,289 km ODO - 146,519

Summary

A thorough analysis was done in identifying the causes that promoted the failure of front axle RHS wheel studs at 70,000+ km and a design solution is proposed.

Design calculations were revisited to check for any fallacy in design and concluded that original design specification holds good for this SCV. Load shift from RHS wheel to LHS wheel due to road camber was studied. It was observed that due to LH road camber with slope 3%, RHS front wheel load had decreased by 6% thus confirming that Indian road camber conditions didn't have any influence on RHS wheel stud failures. However, for wheel stud failures on LHS wheels, influence of Indian road camber conditions should be taken into account while analyzing such failures. Because, LHS road camber causes increase in load on LHS wheels by 6% on front axles and 9% on rear axles which is significant.

Metallurgical analysis of presented failed wheel studs reveals that all the wheel studs failed due to over tightening of wheel nuts causing too high pre-load to the wheel studs. The excessive tension in studs had resulted in yielding of the stud causing relaxation in tension. This pre-load relaxation in studs subjected them to cyclic loads during vehicle operation resulting in eventual fatigue failure.

Since the design load calculations were intact and metallurrgical results confirmed that the failure of studs were due to excessive torqueing, it was decided use a superior wheel stud of same grade with improved fatigue properties and can withstand the abusive torque tightening practices.

With the help from metallurgical experts and fastener suppliers, SAE 4140 stud of grade 10.9 was proposed which is superior to SAE 15B41 stud. SAE 4140 studs have improved mechnical properties due to its additional composition of molybdenum and chromium. Bench level tests were performed to confirm whether SAE4140 wheel studs would withstand excessive torque while tightening. The test results reveled that, SAE 4140 wheel stud was capable of withstanding higher abusive torque of 750Nm than existing SAE15B41 wheel stud which was able to wtihstand torque only upto 591Nm on average.

Endurance trials conducted on proto vehicles with SAE4140 wheel studs and crossed highest failure km without any issues. Based on the above confidence, SAE4140 wheel studs were sucessfully applicated on SCV front axle wheels. More than 14,000 vehicles were sold with SAE4140 wheel studs till date and many customer vehicles have crossed 90,000 km. Some of them covered 1.2 lakh km without any front axle wheel stud failures.

Acknowledgements

This work is carried out under the guidance and motivation of Mr. Alfred Nixon Mendez, Head LCV PD, Ashok Leyland Limited.

References

[1] Artigas, A., Monsalve, A., Colás, R. and Garza-Montes-de-Oca, N., 2017. Failure analysis of the fasten system of wheels used

in mining pickup trucks. Case Studies in Engineering Failure Analysis, 8, pp.28-35.

[2] Fisher, J. and Struik, J., 1974. Guide to design criteria for bolted and riveted joints. New York: Wiley, pp.35-71. ISBN 0-471-83791-1.

[3] Hagiwara, M. and Yoshimoto, I., 1986. The Relation between Load and Strength in Bolted Joints Subjected to Fatigue Loading. Bulletin of JSME, 29(257), pp.3917-3922.

[4] Baggerly, R., 2001. Evaluating the Effects of Over torque in Bolts. Practical Failure Analysis, 1(1), pp.41-46.

[5] Varin, J., 2017. Wheel Attachment Failures in Light-Duty Vehicles. Journal of Failure Analysis and Prevention, 17(4), pp.660-671. doi: 10.1007/s11668-017-0297-0.

[6] Valles González, P., Pastor Muro, A. and García-Martínez, M., 2020. Failure analysis study on a fractured bolt. Engineering Failure Analysis, 109, p.104355.

[7] Croccolo, D., De Agostinis, M. and Vincenzi, N., 2011. Failure analysis of bolted joints: Effect of friction coefficients in torque–preloading relationship. Engineering Failure Analysis.

[8] Boltscience.com. 2022. [online] Available at: <https://www.boltscience.com/pages/failure-of-an-m24-engine-mounting-bolt.pdf> [Accessed 20 July 2021].

Address correspondence to: *Mahadevan Pichandi, Assistant General Manager, Chassis Engineering - LCV PD, Ashok Leyland Technical Centre, Chennai - 600 103.*
Ph: 07299031569
E-mail: Mahadevan.P@ashokleyland.com; mahadevan.p.vellore@gmail.com

ARAI Journal of Mobility Technology
Volume 2 • Issue 2 • April–June, 2022, pp. 183-191
Research Paper
https://doi.org/10.37285/ajmt.1.2.3

Effects of Vortex Generators on Aerodynamic Drag Force in the Hatchback Type Car

Sanjay D. Patil, Vikas T. Mujmule, Ajay P. Mahale, Suhas A. Jagtap and Ganesh S. Patil

Department of Automobile Engineering, Government College of Engineering and Research, Avasari, Pune – Maharashtra.

ABSTRACT

Aerodynamic drag force is one of the main obstacles on moving a vehicle. This force significantly reduces a vehicle's speed and, as a result, its fuel efficiency. In today's scenario, fuel efficiency is a prime concern in vehicle design, so a reduction in aerodynamic drag force is highly important. Road vehicles are designed to pass through surrounding air and displace it as efficiently as possible. Due to the rear shape of a car, airflow suddenly separates from the vehicle at a point near the rear windscreen. This flow separation at the rear end of the car is responsible for the drag force, which is the main opposition to the vehicle's forward motion. This drag force is proportional to the square of the velocity of the car and, as a result, increases significantly after certain speeds. To reduce the drag force, the flow separation at the rear end needs to be avoided. In hatch-back type cars, to avoid this separation, a vortex generator (VG) can be used. VG creates the vortex at the rear end of the car, which delays the flow separation and, ultimately, drag is reduced significantly. In this work, the effect of a VG on the pressure distribution, velocity destitution and aerodynamic drag on the hatchback type car, is studied by the numerical simulation. The numerical simulations are carried out using the ANSYS FLUENT® software. The simulation setup is validated with wind tunnel test results.

KEYWORDS: Drag force; Vortex generator (VG); Aerodynamics forces; Flow separation; Velocity distribution; Pressure distribution; CFD.

Introduction

Aerodynamics is a branch of fluid dynamics that studies interactions between the air and solid bodies moving through it. The aerodynamic forces exerted on a vehicle by the air due to the relative motion of the air and the vehicle when it goes forward. This causes the resistance to vehicle's moment [1-2]. The motion of air around the vehicle is called a "flow field," which is an analysis by using various properties like velocity, pressure, density, and temperature. These properties are a function of position and time and can be calculated by using equations for the conservation of mass, momentum, and energy [3].

When a vehicle is moving, lift and drag are the two primary aerodynamic forces acting on the vehicle. The lift force is acting in the vertical direction on the vehicle body. As the effect of lift force is produced, up-thrust or down-thrust depends upon the shape of the vehicle. Up-thrust is undesirable as it reduces the tyres' ground grips, whereas down-trust enhances the tyre's road-holding [4-6]. The lift force is represented by,

$$F_L = \frac{1}{2}\rho V^2 C_L A \qquad \text{.....(1)}$$

Where,

F_L= Lift force
C_L = Lift coefficient
A= Frontal area of the vehicle
V= Wind velocity
ρ = Air density

The lift coefficient C_L is a dimensionless quantity that is a measure of the difference in pressure created above and below of vehicle body, it is also used to compare the different vehicle shapes [5, 8].

From an energy-saving point of view, the aerodynamic drag force receives special attention [1-2]. The drag force acts in the opposite direction of car movement. Due to constraints created by boot space, rear windscreen, size of car, regulations, etc., cars end up being somewhat obliquely and boxy shaped. Such a shape is responsible for creating the low pressure zone behind a car in a forward motion [5]. This low pressure zone is called the "wake region" [6, 9]. During the airflow over the surface of the vehicle, in the wake region, there are some points when the change in velocity comes to stall and the air starts flowing in the reverse direction. This phenomenon is called "separation" of the flow field, which is undesirable in vehicle motion [7-8]. Ultimately, this airflow separation pulls the car from behind and opposes the forward motion of the car. This is called the "drag force." To avoid this flow separation, the transitions of the airflows from the roof to the rear window need to be smoother [7-9].

The drag force is represented by,

$$F_D = \frac{1}{2}\rho V^2 C_D A \quad \text{.....(2)}$$

F_D = Lift force

C_D = Lift Coefficient

The drag performance of vehicles is characterized by the drag coefficient (C_D) This non-dimensional coefficient allows the drag performance between different vehicles and different setups of the same vehicle to be compared directly [5, 8].

Various kinds of literature are available in the public domain on active and passive systems to minimise the drag force. In case of the active system, jets are used to create vortices, while on passive systems, a modified shape is used to reduce the wake region. The studies by Abdellah Ait Moussa et al. [13] worked on the reduction of aerodynamic drag in generic trucks using optimised geometry of rear cabin bumps. Damjanovic et al. [14] investigated the use of a spoiler to reduce race car aerodynamic drag. Computational analysis of flow separation to reduce the drag force vehicle is performed by Rouméas et al. [15]. Wang et al. [16] studied the active system for drag reduction, even with wheel-vehicle interaction drag force can be reduced. A Steady Jet Flow (SJF) system is reduced the pressure difference at the rear end, this system was used in works by Pastoor et al. [17] for drag reduction. C.H. Bruneau et al. [19] used a combination of jet actuation and a porous top layer on the Ahmed body and presented numerical results showing a remarkable drag reduction of around 31%. Salati et al. [20] examined VG in a truck model with both numerical models and wind tunnel tests and concluded the advantageous effects, besides drag and overturning moment reduction. Lee et al. [21] stated that the spoiler can reduce the vehicle's drag by 3.1%. Zhigang Yang [2] worked on the aerodynamics of pick-up trucks and described the geometrical aspects to reduce drag force. Xin-kai Li et al. [23] examined the offset between two delta-shaped winglets and concluded the maximum drag reduction was achieved at a 5 offset distance/VG height ratio. To the author's best knowledge, less exposure has been observed in the study of the effects of various numbers of VG on the pressure contours, velocity vector, and aerodynamic drag force in the case of a hatchback type car.

This paper is structured as follows. The finite volume numerical simulations are performed on ANSYS FLUENT software. The numerical simulation setup is validated with a wind tunnel test in Section 2. A similar set-up has been used in section 3 to analyse the effect of VGs on the aerodynamic characteristics of a hatchback car, namely, velocity destitution, pressure distribution, velocity vectors, and drag force. First, a car model without VGs is considered the baseline configuration, and using numerical simulation, the aerodynamic characteristics of the baseline model are evaluated. Second, on the same setup, one to five number of VGs are attached at the rear end of the car and evaluate aerodynamic characteristics. Furthermore, these aerodynamic characteristics are compared with each other and with the baseline configuration.

Experimental Validation of Simulation Setup

Vortex Generator

In various car models, VG is used to reduce the drag force. The rear end of hatchback cars is somewhat obliquely and boxy. As discussed in section 1 flow separation takes place at the rear end of the car and air starts moving in the reverse direction, which causes the drag force as shown in figure 1 [8, 21]. A VG is one of the solutions to this problem [17,21]. A VG is an aerodynamic surface made up of a small vane or bump that is attached to the back of the car because of its shape and position, which creates a vortex [20].VG controls the boundary layer transition by creating a vortex at the rear end, which delays the flow separation and, ultimately, drag is reduced significantly [19, 21, 22].

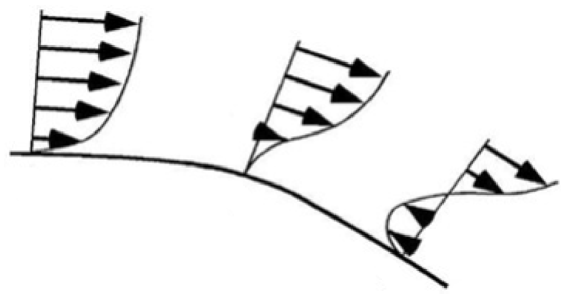

Fig. 1. Flow of air at rear end of car.

Experimental Setup on Wind tunnel test

The validation of the numerical simulation setup is to be done by using the wind tunnel test ring. The airfoil model, having a chord length of C=100 mm and a length of L= 300 mm, is placed in the wind tunnel at an angle of attack of α=50 with the free stream direction. The upstream velocity V= 15m/s and the density ρ is 1.2kg/m3. The air velocity is assumed to be steady state, inviscid, and uniform. A piezometer is used to measure the pressure difference ΔP along the length of the airfoil model. The experimental setup is shown in figure 2.

Fig. 2. Wind tunnel experimental setup.

The elemental pressure force per unit span of airfoil is can be expressed as,

$$df = \Delta P\, dl, \quad .....(3)$$

Due to airfoil model angle of attack this element pressure is divided into two component, and they are calculated by,

$$df_x = \Delta P\, dy \quad .....(4)$$

$$df_y = \Delta P\, dx \quad .....(5)$$

Therefore, total force in X and Y direction is can be evaluated by integrating the element force along the Y and X direction respectively. This is to be done by measuring the pressure using piezometer along curtain interval in the X and Y direction of airfoil model so,

$$F_x = \int \Delta P\, dy \quad .....(6)$$

$$F_y = \int \Delta P\, dx \quad .....(7)$$

Dynamic pressure on airfoil model is obtained by,

$$F = \frac{1}{2}\rho V^2 C \quad .....(8)$$

Where C is force coefficient which is have two component in X and Y direction which are,

$$C_x = \frac{Fx}{(\frac{1}{2}\rho V^2)} = \frac{\int \Delta P\, dy}{(\frac{1}{2}\rho V^2)} \quad .....(9)$$

$$C_y = \frac{Fy}{\frac{1}{2}\rho V^2} = \frac{\int \Delta P\, dx}{\frac{1}{2}\rho V^2} \quad .....(10)$$

For airfoil angle of attack $\alpha=5^0$ and piezometer angle of inclination $\theta=0^0$ the C_D and C_L are calculated by,

$$C_D = C_y \sin\theta + C_x \cos\alpha \quad .....(11)$$

$$C_L = C_y \cos\alpha - C_x \sin\theta \quad .....(12)$$

Numerical Simulation setup on CFD software

To validate the numerical simulation setup, all parameter values like velocity, the density of air, size of airfoil model, etc. are taken as the same as used in the wind tunnel experimental test in section 2.2. The airfoil 3D model is created in the SolidWork software and import into the ANSYS software for further analysis. The necessary boundary conditions like inlet velocity, outlet velocity, and wall movements are applied, and the model is mesh with an element size of 1.5. Figure 3 (a) and (b) show the velocity distribution and streamline flow around an airfoil. The C_D and C_L are obtained from simulation and compared with wind tunnel test results in Table 1.

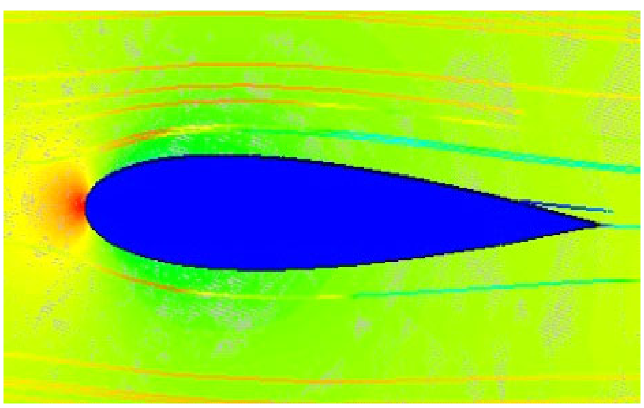

Fig. 3 (a) Velocity distribution around airfoil.

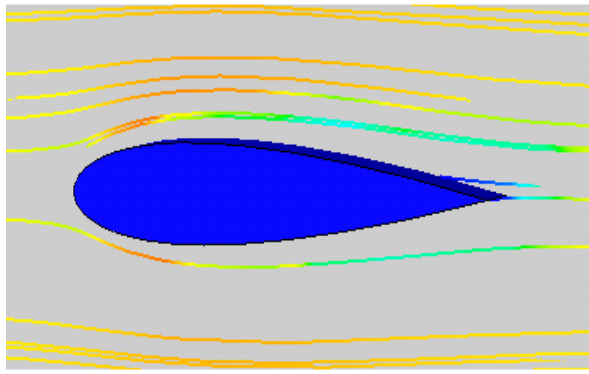

Fig. 3 (b). Velo. streamline around airfoil.

TABLE 1

Experimental and simulation results comparison

Sr. No.	Parameter	Wind tunnel experimental	Numerical Simulation	Percentage Error
1	Drag Coefficient (C_D)	0.213	0.197	9.2%
2	Lift Coefficient (C_L)	0.197	0.174	8.8%

It has been observed that the absolute error between the wind tunnel experimental test and the CFD simulation of C_D and C_L is less than 10% and they are considerably closer to each other. Hence, the above-mentioned simulation setup is considered in the present work for further study of the car model with VG and without VG.

Numerical Simulation

The hatchback car model shown in Figure 4 was selected for the study. The 3D geometrical model of the car is created in the SolidWork software and has an overall length of 3765mm, an overall height of 1500mm, and an overall width of 1690mm. As per the many kinds of literature, the optimum height of the VG is defined as being almost equal to the boundary layer thickness [5]. The most favourable size of VG is found to be 25.45 mm X 10mm of a bump-shaped piece with a rear slope angle of 25°. Figure 5 shows the dimension of VG [23,24]. The location of vortex generators is selected at a point immediately upstream of the flow separation point and a point at a distance of 100 mm from the facade of the roof end.

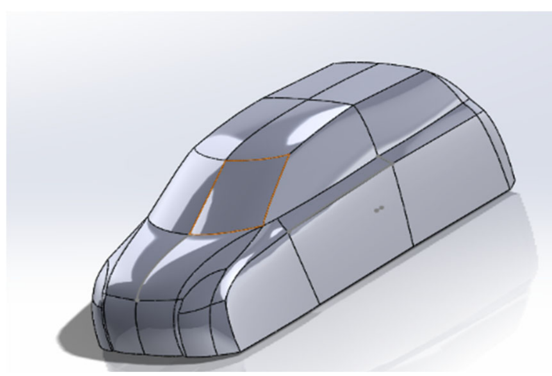

Fig. 4. Hatchback car base model.

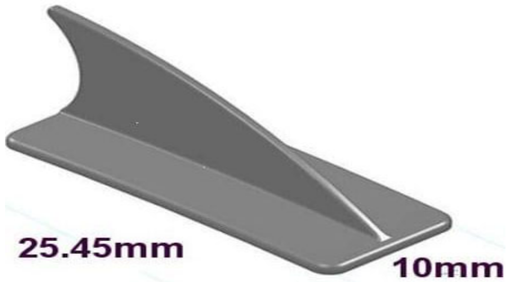

Fig. 5. Dimensions of Vortex generator.

A further computational analysis is carried out in the ANSYS FLUENT software. The car model is imported into ANSYS software. For the computational simulation, it has been assumed that the airflow is a steady-state with constant velocity at the inlet, constant pressure outlet, no-slip wall boundary conditions at the car's body, and inviscid flow wall boundary conditions at the car's surface, roof, and sidewall. The enclosure size is based on literature [21], and dimensions in X, Y, and Z directions are 6L X 2L X 2L m, respectively. The necessary boundary conduction like inlet velocity, outlet velocity, and wall movement is applied in simulation. The model is discretized with triangular elements of size 1.5. The other simulation parameters are given in table 2, and the ANSYS simulation setup is shown in figure 6.

TABLE 2

Simulation Parameters.

Sr. No	Parameter	Boundary conditions	Parameter Values
1	Velocity inlet	Magnitude measured normal to boundary	60 km/hr
2	Pressure outlet	Gauge pressure magnitude	0 Pa
		Gauge pressure direction	Normal to boundary
		Turbulence specification method	Intensity & viscosity
		Backflow turbulence intensity	10%
3	Fluid properties	Fluid type	Air
		Density (ρ)	1.175 (kg/m3)
		Kinematic viscosity (V)	1.7894 × 10−5 (kg/(m s))

To analyse the effect of VG on drag force, the first simulation (simulation 1) is performed without VG by taking the above-said parameter. During the simulation process, drag force, lift force, drag coefficient, and lift coefficient were tracked. Simulation 2 is carried out by taking the 1 number of VG mounted at the centre of the roof. The simulation parameters for simulation 2 and further simulations are kept the same as in simulation number 1. Similarly, simulations 3 to 6 are performed by taking the 2 to 5 number of VGs, respectively. For all simulations, the above-mentioned parameter values are obtained. The pressure distribution, velocity distribution, and velocity vector of all 6 simulations are plotted to analyse the flow separation. A detailed comparison of CFD results is discussed in the following section.

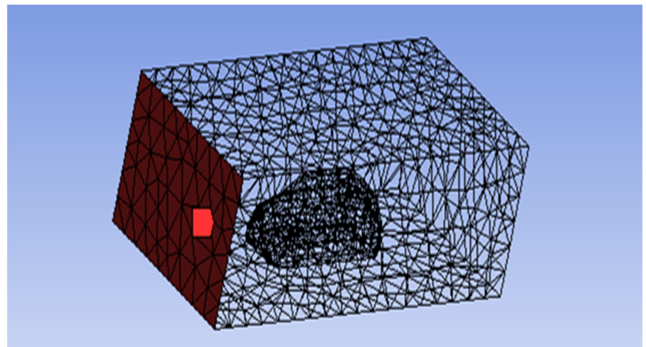

Fig. 6. ANSYS simulation setup.

Result and Discussion

All the simulations mentioned in the previous section are performed and their results, like pressure distribution, velocity distribution, velocity streamline, and value of drag force, are obtained and discussed in detail in the following subsections.

Pressure Distribution

The pressure distribution around the car model for all simulations is as expected. The high-pressure zone is depicted in red in Figures 7(a-f), and the low-pressure zone is depicted in blue.

It was observed that the pressure distribution in different areas behaves differently because of the way air particles interact with a certain portion of the car. At the front of the car, there is a direct collision of air partials, so for all simulations at the front, there is a high-pressure zone. On the other hand, at the rear end, the pressure is considerably lower. As discussed earlier, the low-pressure zone at the rear end is the main factor in creating the drag force. Figure 7 (a) shows that the low-pressure zone blue spots are more prevalent at the rear end of Simulation 1 (without VG) than in the other figures. While, in figures 7 (e) and (f) (simulations 5, and 6), low-pressure zones, blue spots are observed on the roof of the car. Low-pressure zone spots in figures 7(b) and (c) (Simulations 2 and 3) are comparable to fewer in other figures. As the number of VG increases, as in figures 7 (e) and (f) (simulations 5 and 6), low-pressure zones are observed at the roof of the car, which increases drag force at the roof of the car.

Velocity Distribution

Figure 8 (a to l) depicts the velocity distribution and velocity vectors of all simulations at a symmetry plan.

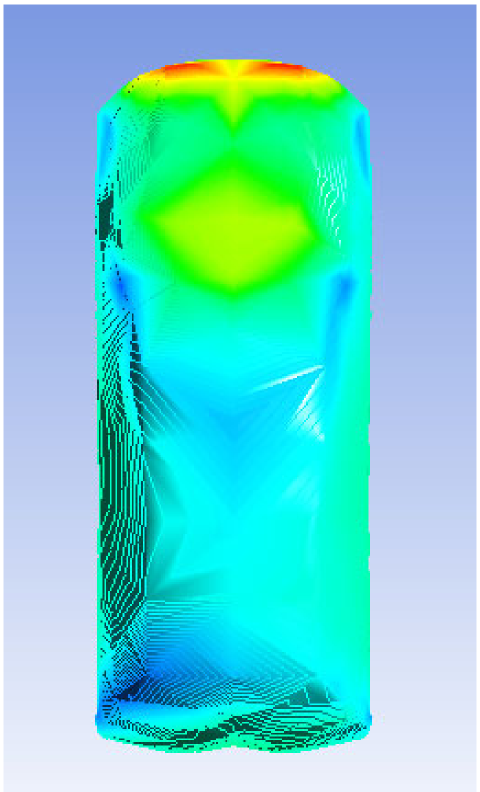

Fig. 7 (**a**) Pressure distribution of sim. 1.

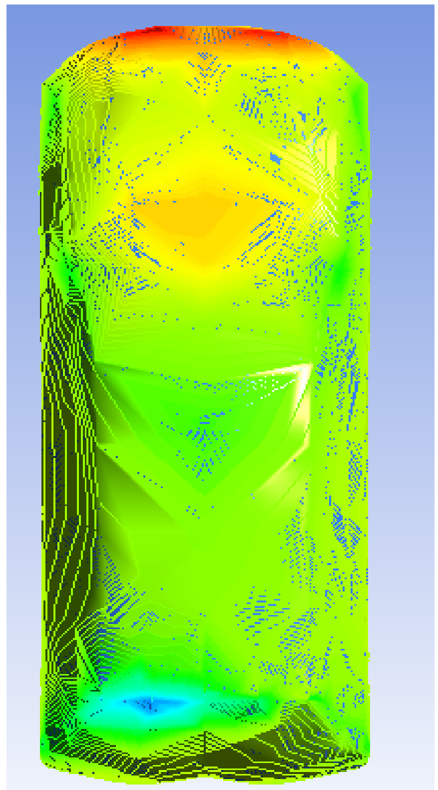

Fig. 7 (**b**) Pressure distribution of sim. 2.

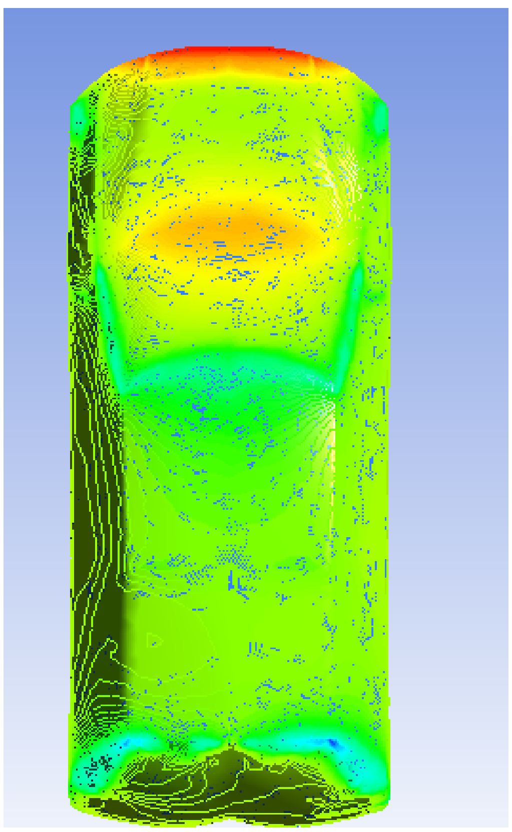

Fig. 7 (**c**) Pressure distribution of sim. 3

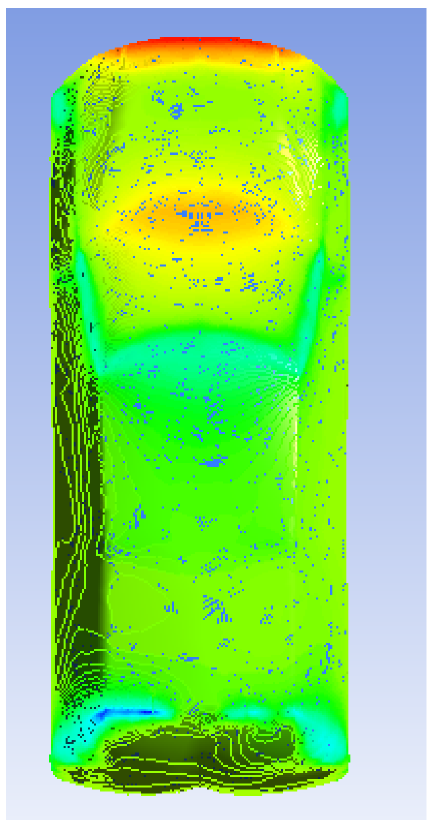

Fig. 7 (**d**) Pressure distribution of sim. 4

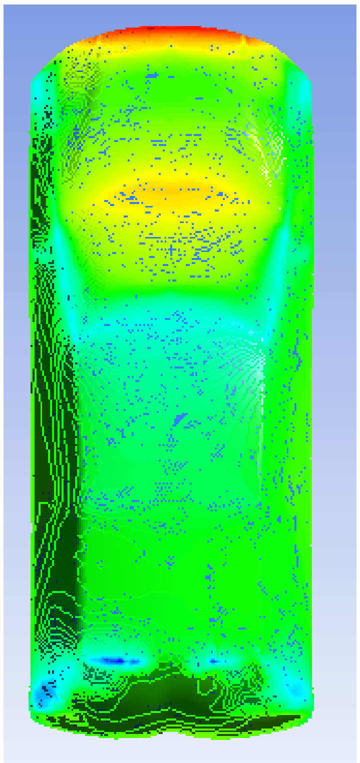

Fig. 7 (e) Pressure distribution of sim. 5

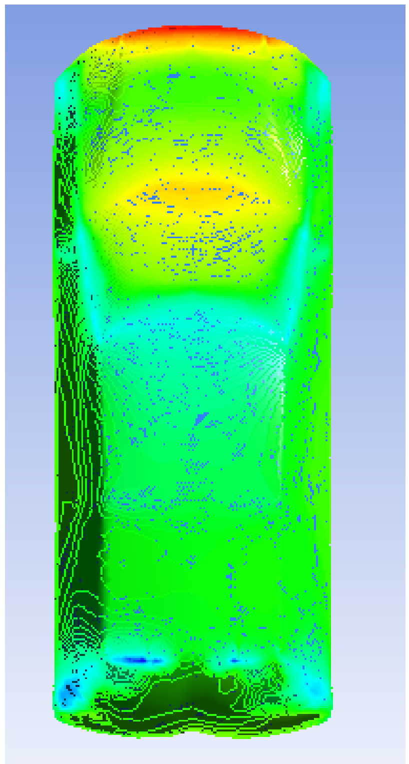

Fig. 7 (f) Pressure distribution of sim. 6

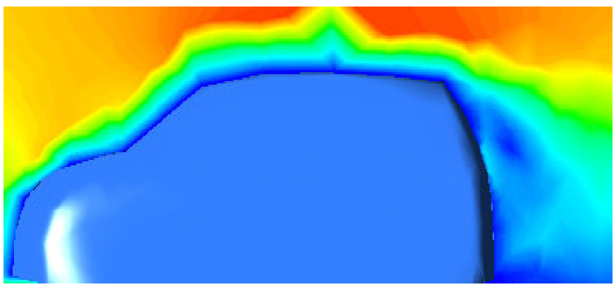

Fig. 8(a) Velocity distribution of sim.1

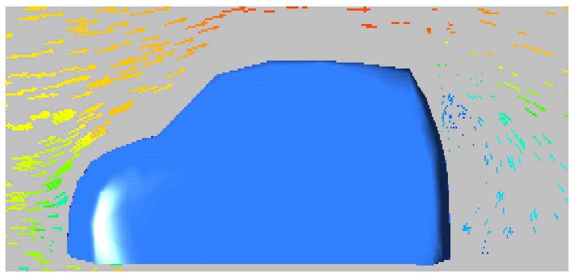

Fig. 8(b) Vel. vectors distribution of sim.1

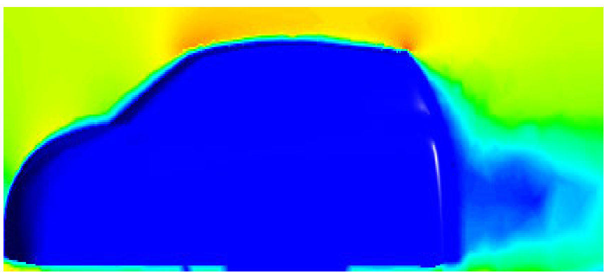

Fig. 8(c) Velocity distribution of sim.2

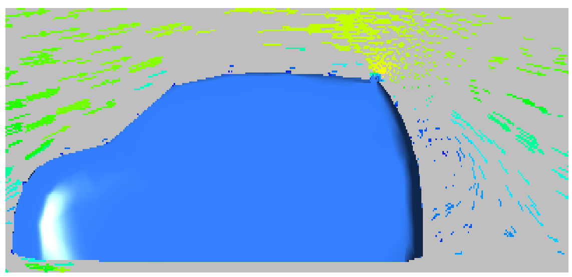

Fig. 8(d) Vel. vectors distribution of sim.2

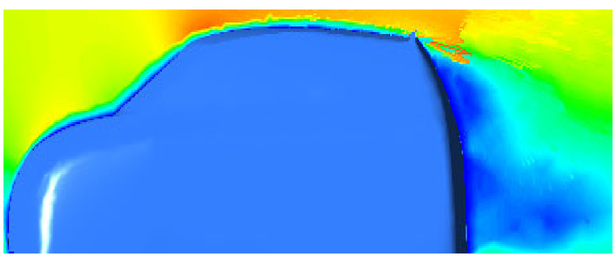

Fig. 8(e) Velocity distribution of sim.3

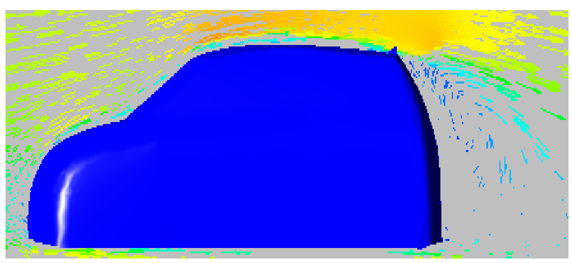

Fig. 8(f) Vel. vectors distribution of sim.3

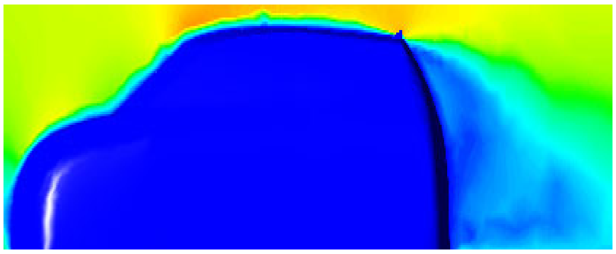

Fig. 8(g) Velocity distribution of sim.4

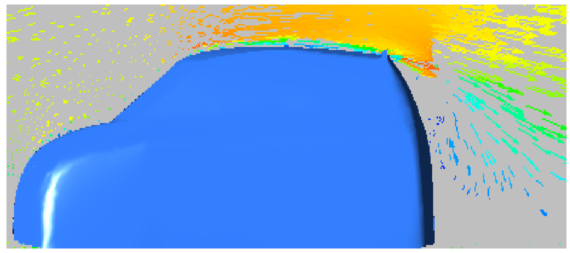

Fig. 8(h) Vel. vectors distribution of sim.4

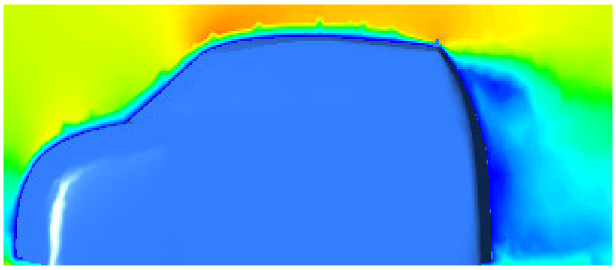

Fig. 8(i) Velocity distribution of sim.5

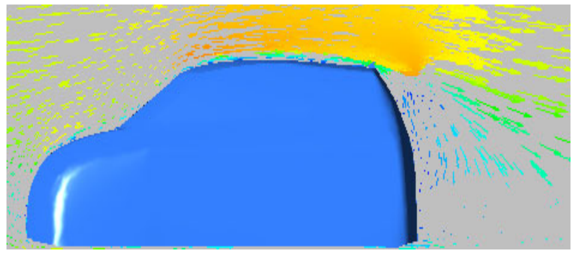

Fig. 8(j) Vel. vectors distribution of sim.5

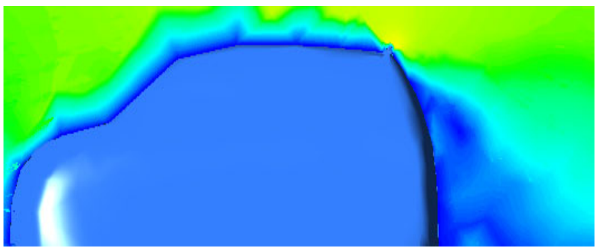

Fig. 8(k) Velocity distribution of sim.6

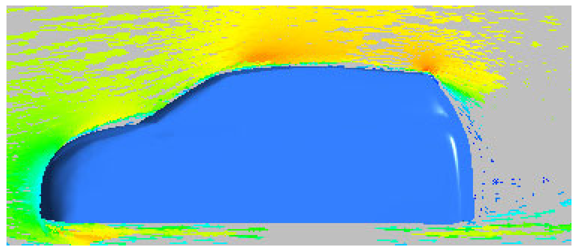

Fig. 8(l) Vel. vectors distribution of sim.6

From the figures, it has been found that there were recirculation zones behind the rear end of the vehicle. This is due to the created low-pressure zone at the rear end, as discussed in 4.1. By comparing the simulation figures, it is seen that the recirculation zone behind the rear end of simulation 1 (without VG, figure 8 (a and b)) is much closer to the rear end of the car compared to other simulations. It indicates the reverse flow of air occurs very near the rear end of the car. This reverse flow ultimately creates drag force. In the simulations 2 and 3 (figures 8 (c) to 8 (f)), as velocity vectors reversed away from the rear end of the car, the drag force decreased. On the other hand, it is seen from the velocity vectors of simulations 4, 5, and 6 (figure 8 (h), (j) and (l)) that at the roof of the car, air flow is also getting reversed, which increases the drag force.

Drag Coefficient

The values of the drag coefficient of all simulations are tabulated in table 3. Figure 9 shows the variation in drag coefficient over the number of VG.

TABLE 3

Drag Coefficient Simulation Results

Simulation Number	Number of VG	Drag Coefficient (C_D)
1	Without VG	0.2468
2	1	0.2183
3	2	0.2210
4	3	0.2319
5	4	0.2440
6	5	0.2442

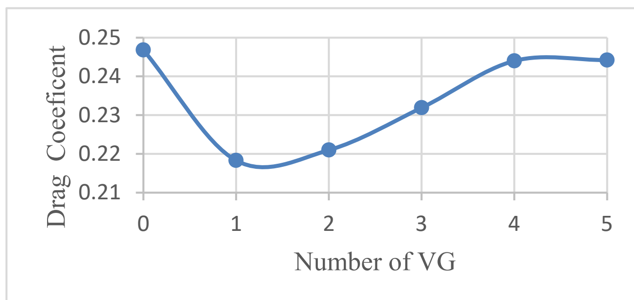

Fig. 9. Number of VG versus drag coefficient.

From table 3 as well as from figure 9, the drag coefficient of a car without VGs is higher compared to a car with 1 or 2 number of VGs. Further, with 4, 5, and 6 number of VGs, the drag coefficient increases. As discussed in sections 4.1 and 4.2, for simulation no. 1, low-pressure zones in the rear-end cause the reverse flow of air in that region and eventually the drag force created in this region.

With the 1 or 2 number VGs on the car, the low-pressure zone gets shifted away from the rear end. Hence, velocity is getting revered away from the rear end. It results in a drag coefficient in these cases being lower than in others.

The 4, 5, or 6 number VGs on the car act as a blunt body in a flow of air. That creates a low-pressure zone at the roof of the car, which results in bad aerodynamics and increases the pressure drag coefficient.

Conclusion

Numerical simulations have been performed on the hatchback car model without and with an increasing number of VGs. Its effects on pressure distribution, velocity distribution, and drag coefficient are investigated in this work. The low-pressure zone behind the moving vehicle is responsible for aerodynamic drag. A VGs were installed to control the low-pressure zone. It was found that without VG, a low-velocity zone is created near the rear end of the car, which causes a high drag force on the car.

The low-velocity zone is shifted away from the rear end of the car when VGs are used, resulting in a decreased drag coefficient. In this study, utilising 1 and 2 numbers of VGs lowered the drag coefficient by up to 11% as compared to without VG.

This study also gives insight on the effects of a number of VGs. It was observed that a greater number of VGs were behaving as blunt bodies in airflow in hatchback cars. This has an adversely effect on the pressure distribution on the car roof. As a result, the drag coefficient of five VGs is higher than the drag coefficient of one VG.

References

[1] Mathieu Roumeas , Patrick Gillieron and Azeddine Kourta 'Drag reduction by flow separation control on a car after body' International Journal For Numerical Methods In Fluids, 2009; 60:1222–1240.
https://doi.org/10.1002/fld.1930

[2] Zhigang Yang and Bahram Khalighi 'CFD Simulations for Flow Over Pickup Trucks' SAE Technical Paper Series, 2005-01-0547.
https://doi.org/10.4271/2005-01-0547

[3] Ram Bansal and R. B. Sharma 'Drag Reduction of Passenger Car Using Add-On Devices' Hindawi Publishing Corporation Journal of Aerodynamics Volume 2014, Article ID 678518.
http://dx.doi.org/10.1155/2014/678518.

[4] Md. Rasedul Islam, Md. Amzad Hossain, Mohammad Mashud, Md. Tanvir Ibny Gias 'Drag Reduction of a Car by Using Vortex Generator' International Journal of Scientific & Engineering Research, Volume 4, Issue 7, July-2013 ISSN 2229-5518

[5] S.M. Rakibul Hassan, Toukir Islam, Mohammad Ali, Md. Quamrul Islam 'Numerical Study on Aerodynamic Drag Reduction of Racing Cars' 10th International Conference on Mechanical Engineering, ICME 2013

[6] R. Himeno, K. Fujitani 'Numerical Analysis and Visualization of Flow in Automobile Aerodynamics Development' Journal of Wind Engineering and Industrial Aerodynamics, 46 & 47 (1993) 785-790

[7] Simon Watkins, Gioacchino Vino 'The effect of vehicle spacing on the aerodynamics of a representative car shape' Journal of Wind Engineering and Industrial Aerodynamics' 96 (2008) 1232–1239.
https://doi.org/10.1016/j.jweia.2007.06.042

[8] Diogo Barros, Jacques Bor, Bernd R. Noack, Andreas Spohn and Tony, 'Bluff body drag manipulation using pulsed jets and Coanda effect' Ruiz, Journal of Fluid Mech. (2016), vol. 805, pp. 422–459.
https://doi.org/10.1017/jfm.2016.508

[9] H. Viswanathan, 'Aerodynamic performance of several passive vortex generator configurations on an Ahmed body subjected to yaw angles' Journal of the Brazilian Society of Mechanical Sciences and Engineering (2021) 43:131.
https://doi.org/10.1007/s40430-021-02850-8

[10] Trebsijg van de Wijdeven, Joseph Katz 'Automotive Application of Vortex Generators in Ground Effect' Journal of Fluids Engineering February 2014, Vol. 136.
https://doi.org/10.1115/1.4025917

[11] S Y Cheng and S Mansor, 'Rear-roof spoiler effect on the aerodynamic drag performance of a simplified hatchback model', Journal of Physics: Conf. Series 822 (2017) 012008.
https://doi.org/10.1088/1742-6596/822/1/012008

[12] N. Ashton, A. West, S. Lardeau, A. Revell, 'Assessment of RANS and DES methods for realistic automotive models' Computers and Fluids 128 (2016) 1–15.
https://doi.org/10.1016/j.compfluid.2016.01.008

[13] Abdellah Ait Moussa, Justin Fischer, and Rohan Yadav 'Aerodynamic Drag Reduction for a Generic Truck Using Geometrically Optimized Rear Cabin Bumps' Hindawi Publishing Corporation Journal of Engineering Volume 2015, Article ID 789475.
https://doi.org/10.1155/2015/789475

[14] Darko Damjanovic, Drazan kozak, Marija Zivic, Zeljko Ivandic, Tomislav Baskaric 'CFD analysis of concept car in order to improve aerodynamics' Scientific and Expert Conference TEAM 2010, Kecskemet, November 4-5, 2010

[15] M. Rouméas, P. Gilliéron and A. Kourta, 'Drag Reduction by Flow Separation Control on a Car after Body', International Journal for Numerical Methods in Fluids, 60(2009) 1222–1240.
https://doi.org/10.1002/fld.1930

[16] Yifei Wang, Christophe Sicot, , Jacques Boree, Mathieu Grandemange, 'Experimental study of wheel-vehicle aerodynamic interactions', Journal of Wind Engineering and Industrial Aerodynamics Volume 198, March 2020, 104062

[17] Mark Pastoor Lars Henning Bernd R. Noack, Rudibert King ,Gilead Tadmor, 'Feedback shear layer control for bluff body drag reduction', Journal of Fluid Mechanics , Volume 608 , 10 August 2008 , pp. 161 – 196.
https://doi.org/10.1017/S0022112008002073

[18] Cheng, S.Y., Tsubokura, M., Nakashima, T., Nouzawa, T., Okada, Y., 'A numerical analysis of transient flow past road vehicles subjected to pitching oscillation', Journal of Wind Engineering and Industrial Aerodynamics Volume 99, Issue 5, May 2011, Pages 511-522.
https://doi.org/10.1016/j.jweia.2011.02.001

[19] Charles-Henri Bruneaua ,Emmanuel Creuséb, Patrick Gilliéronc, Iraj Mortazavia, 'Effect of the vortex dynamics on the drag coefficient of a square back Ahmed body: Application to the flow control', European Journal of Mechanics - B/Fluids Volume 45, May–June 2014, Pages 1-11.
http://dx.doi.org/10.1016/j.euromechflu.2013.11.003

[20] L.Salati, P.Schito, F.Cheli, 'Strategies to reduce the risk of side wind induced accident on heavy truck', Journal of Fluids and Structures Volume 8 8, July 2019, Pages 331-351. https://doi.org/10.1016/j.jfluidstructs.2019.05.004

[21] Sang Wook Lee, Hak Lim Kim, 'Numerical Study of Active Aerodynamic Control via Flow Discharge on a High-Camber

Rear Spoiler of a Road Vehicle' Applied Science, 2019, 9(22), 4783.
https://doi.org/10.3390/app9224783

[22] Alamaan Altaf, Ashraf A. Omar , Waqar Asrar, 'Passive drag reduction of square back road vehicles', Journal of Wind Engineering and Industrial Aerodynamics Volume 134, November 2014, Pages 30-43.
http://dx.doi.org/10.1016%2Fj.jweia.2014.08.006

[23] Xin-kai Li, Wei Liu Ting-jun, Zhang, Pei-ming Wang and Xiao-dong Wang, 'Analysis of the Effect of Vortex Generator Spacing on Boundary Layer Flow Separation Control', Applied Science Journal . 2019, 9, 5495.
https://doi.org/10.3390/app9245495

[24] Xin-Kai Li ,Wei Liu 1,Ting-Jun Zhang, Pei-Ming Wang and Xiao-Dong Wang, 'Experimental and Numerical Analysis of the Effect of Vortex Generator Installation Angle on Flow Separation Control' Energies 2019, 12(23), 4583.
https://doi.org/10.3390/en12234583

Address correspondence to: *Mr. Sanjay D. Patil, Assistant Professor, Department of Automobile Engineering, Government College of Engineering and Research, Avasari, Pune - Maharashtra.*
Ph: 09029719392
Email: sanjaypatil365@gmail.com; sdpatil.auto@gcoeara.ac.in

ARAI Journal of Mobility Technology
Volume 2 • Issue 2 • April–June, 2022, pp. 192-197
https://doi.org/10.37285/ajmt.1.2.4

Research Paper

Deep Learning Model for Prediction of Air Mass Deviation Faults

Karthik Chinnapolamada

RDI/CEP, Mercedes Benz Research and Development Private Limited, Embassy Crest Phase-2, Whitefield Road, Bangalore-560066, India

ABSTRACT

Major Systems of an internal combustion Engine are Air System, Fuel system, Exhaust system. Any malfunction in these systems increases emissions. OBD legislation mandates to monitor these systems for any faults and appropriate action should be taken in case of the any faults which increases vehicle emissions.

The idea of the paper is to find the Air mass flow deviation faults using datamining and machine learning based approach. Detection of fault is classifying whether system is faulty or not. Objective is to create a deep learning model using the available vehicle data to classify the system for a fault.

Three main inputs for the Air Mass flow in an internal combustion Engine are

1) Fresh Air which measure using Mass Air Flow sensor
2) Low Pressure EGR
3) High Pressure EGR

During vehicle lifetime, due to different real vehicle operating conditions and environmental conditions, deviation in the set point of air mass flow and actual mass flow are possible to an extent, which can affect vehicle emissions. Deviation in the Air Mass flow can be caused by intake Air mass, LP-EGR, HP-EGR. The Aim of the project is to create the deep learning model for Air Mass Flow Hi and Low faults using the available data, and associate the fault to the component in the Intake Air System.

KEYWORDS: OBD, LPEGR, HPEGR, Machine Learning, Emissions, Deep Learning, Air Mass Deviation, Internal Combustion Engine, Air Mass Flow, Hi and Low faults, Intake Air System.

Introduction

OBD refers to the On Board Diagnostics, which refers to Vehicles self-diagnosis, and reporting capability. Fulfilment of OBD-regulation is required worldwide for type approval of any vehicle and the regulations discussed in paper are based on California regulations, where the regulations are first introduced. Section 1968.2 of California code of regulations defines the OBD requirements for California. The purpose of this regulation is to reduce Motor Vehicle emissions by establishing emission standards and requirements for OBD.

- Legislative Requirements Mandates detection and reporting of Faults in Engine which increases the Emissions
- Malfunction of any components in the Intake Air System will have adverse effect on the emissions; hence detecting Air System Faults is a Mandatory requirement.
- Any deviation in the Intake Air Mass flow set point can increase the Emissions in Vehicle so OBD system shall able to detect and report any such deviation in Air Mass flow.
- Current approaches dependent on Empirical formulas for detection of Air Mass flow deviation faults.
- Idea is to apply AI and ML techniques for the prediction of Fault.

Purpose

The Objective of the Paper is to create a deep learning model, which can predict Intake Air System Mass flow deviation faults by making use of the available vehicle data

Scope of Project

- To predict Air Mass Flow deviation in the Internal combustion by making use of the existing vehicle data available
- Model shall be able to predict the cause of deviation in the Air Mass flow.

ABBREVIATIONS: LP - Low Pressure; HP - High Pressure; EGR - Exhaust Gas recirculation Valvel; OBD - On Board Diagnostics; AI - Artificial Intelligence; ML - Machine Learning

- Here Cause of Deviation refers to fault in Air Mass flow Sensor, Low pressure Exhaust gas recirculation valve and High pressure Exhaust gas recirculation valve.

Motivation

Lots of Vehicle measurements are available in the organization, the idea is to make use of the existing data to create Model which predicts the Air system Faults. This helps in making the better engine control and fault prediction and pinpointing of the Air Mass Faults more reliable.

Existing System

Current Systems depends on different physical parameters like Mass flow, Pressure, Temperatures at different points in the Engine to decide on the deviation in actual Mass flow and set point, classify whether the system has fault or not.

Proposed System

The new system should learn fault patterns from existing data and should predict the faults by analysing the input sample.

Features of the Proposed System

The System should be able to predict the below faults by analysing the input sample data

1. Air Mass Sensor High Flow
2. Air Mass Sensor Low Flow
3. Low pressure Exhaust Gas Recirculation High Flow
4. Low pressure Exhaust Gas Recirculation Low Flow
5. High pressure Exhaust Gas Recirculation High Flow
6. High pressure Exhaust Gas Recirculation Low Flow
7. No Fault

Process

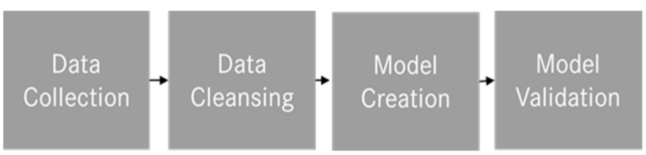

Fig. 1. Process flow.
(Created by Author to represent the Process flow in executing the project)

The whole process divided into four steps

1. Data collection – First step where all the required data for creating the model will be collected
2. Data cleansing – Raw data collected has to be processed to extract the required data and to the required format.
3. Model Creation- The processed Data has to be fed to the Machine Learning Algorithms for creating Data based Model
4. Model Testing – Testing of the Model created in Step 3

Data Collection

- Total Data collected :38.5 GB
- Data format: .mdf , .dat
- Data Source: Engine Control Unit
- Type of Data: Numerical
- Data contains recording of different Engine control signals like Engine Speed, Injection Quantity, Intake Air Mass flow, EGR rate etc.
- All these Signals are used by the Engine control unit software to control different Engine Actuators for Efficient Engine operation and to keep the Emissions in control
- Aim of the project is to identify signals which impact the Air system faults, analyze the behavior of these signals and implement the ML algorithm which gives the best results

Data Cleansing

Data cleansing or **data cleaning** is the process of detecting and correcting (or removing) corrupt or inaccurate records from a record set, table, or database and refers to identifying incomplete, incorrect, inaccurate or irrelevant parts of the data and then replacing, modifying, or deleting the dirty or coarse data (Source: Wikipedia).

A training and testing dataset created for training and testing the model.

The below steps are performed as a part of Data cleansing

- **Identification of the required variables(Features) –** Feature selection is one of the key steps in the whole process of datamining and it will have a huge impact on the performance of the model. Irrelevant features can negatively affect the performance of the model. Hence feature selection has to be done carefully to achieve the better prediction results. A total of 18 features selected, features are selected based on the expert opinion in the Air system, independent of current inputs for fault detection and effect of the feature on the fault itself.

TABLE 1
Features considered for the Model creation

Feature 1	Accelerator Pedal Position
Feature 2	Charge Air Cooler Down Stream Pressure
Feature 3	Charge Air Cooler Down Stream Temperature
Feature 4	Air Mass Per Stroke
Feature 5	Actual EGR Percentage
Feature 6	Boost Pressure
Feature 7	Set point EGR Percentage
Feature 8	Exhaust Flap Position
Feature 9	EGR Position
Feature 10	Engine Speed
Feature 11	Injection Quantity
Feature 12	EGR Differential Pressure
Feature 13	Swirl Valve position Demand
Feature 14	Turbine Input Temperature
Feature 15	Turbine Input Pressure
Feature 16	VTGA Position Demand
Feature 17	Throttle Position
Feature 18	Engine Torque Request

(Created by Author to represent the features selected for Machine Learning Model)

- **Labeling each Vehicle measurement with Fault class for each fault from 0 to 6**

  Each file has been recoded with a particular fault created. Labeling of each fault with corresponding fault class is primary step. This fault class serves as target class for training the model. Labeling of each training file has to be done carefully as wrong labeling of file affects the performance of the model. All the files used for training and testing are labeled with fault class before start of the analysis. All labeled files are further separated into different train set as the processing of whole data takes huge time for the analysis.

  After labeling files, each file needs to process for the features. Vehicle recordings, which only have all the required features, considered for the training and testing dataset creation. Each file is analyzed for the required features and files which has the required features are separated and used for training the model.

Fault Class	Fault
0	No Fault
1	Air Mass Sensor Low Flow
2	Air Mass Sensor High Flow
3	Low Pressure EGR Low Flow
4	Low Pressure EGR High Flow
5	High Pressure EGR Low Flow
6	High Pressure EGR High Flow

- **Filtering Samples**

  Not every sample in the files with required inputs considered for the training as not all required enable conditions met. Hence, each data sample added to the dataset only when the fault enable conditions met.

```
Not faulty Sample (class 0):
    IF (ANY of one Fault criteria is satisfied)
        Add Sample to the Dataset;
    Else
        Discard Sample;
    End
Faulty Sample (Other than class 0):
    IF (Particular Fault criteria is satisfied)
        Add Sample to the Dataset;
    Else
        Discard Sample;
    End
```

- **Identification of steady state conditions**

  Identified the Steady state condition by evaluating the different engine parameters and sample added to data set only if the steady state conditions met. Filtered all transients out of the data set. Sample space of 30 samples are taken for calculating the Moving average of Engine Speed and Injection quantity to verify the steady state

  $$n_{avg} = ((n_1 + n_2 + n_3 + \cdots \ldots + n_{30})/30)$$

  Ignore sample, which has a deviation of over 10% from moving average

  IF $|n_{avg} - n_1| \le 10\%$:

  Add Sample

  ELSE:

  Discard Sample

  'n' represents Engine Speed and Injection Quantity

- **Normalization of data**

  Normalization of data is one of the important steps in the data mining. Different features are recorded on a different scale and it is very important to bring all the feature to the same scale. Normalization is required to achieve this. Min-Max normalization applied to normalize data.

  Formula:

  $$x_{norm} = \left(\frac{(x) - (x_{min})}{(x_{max}) - (x_{min})}\right) . \left((x_{maxnew}) - (x_{minnew})\right) + \left((x_{minnew})\right)$$

  $$x_{normperc} = x_{norm} * 100$$

  x = *sample value*

  $x_{norm} = Normalized\ sample\ value\ in\ the\ range$ [0 1]

  $x_{normperc} = \ Normalized\ sample\ value\ in\ the\ range$ [0 100]

  $x_{max} = maximum\ value\ of\ x\ in\ the\ dataset$

  $x_{min} = minimum\ value\ of\ x\ in\ the\ dataset$

  $x_{maxnew} = new\ maximum\ value\ of\ x = 1$

  $x_{minnew} = new\ minimum\ value\ of\ x = 0$

  All the different features, which are in different, scale converted to the range 0 to 1 or 0 to 100% for training the model.

- **Outlier Detection**

  BOX plot drawn to detect the outlier. No sample removed from the dataset as all the data recorded in the vehicle and all scenarios represent the driving behavior.

- **Density plots**

  Density plots drawn to understand the distribution of data

  Transformations Techniques are used to correct the Skewness in the plots

- **Files with double faults**

  Files which more than one fault are discarded for the creation of dataset

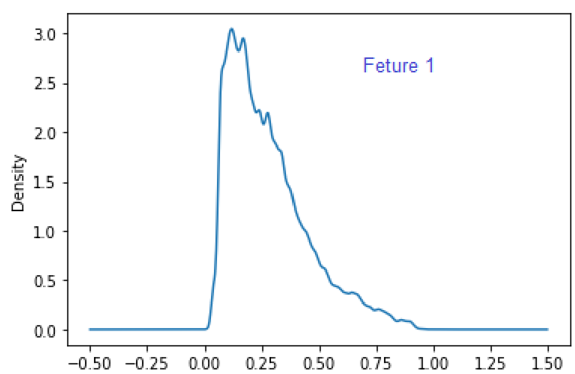

Before Transformation

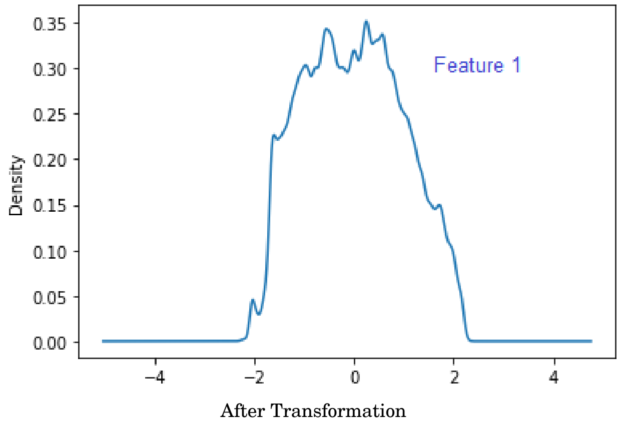

Fig. 2. Feature Transformation.

Model Creation

Neural network model

A multilayer perceptron comprises of multiple layers of logistic regression. Multi-layer perceptron is a feed forward neural network; Multi-layer perceptron model built fort classification of Air Mass deviation faults.

Neural Network Architecture

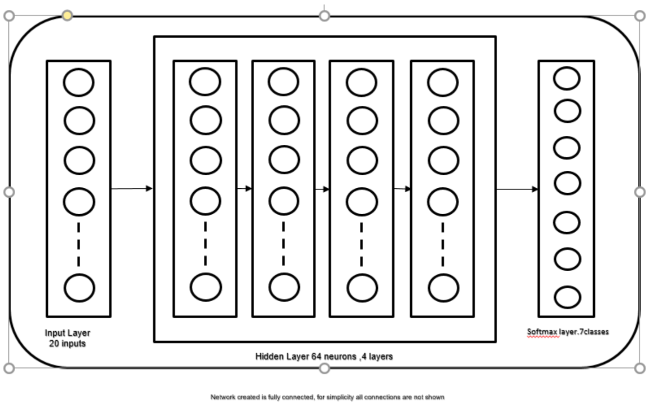

Fig. 3. Neural Network Architecture.

The above figure explains the architecture of the neural network.

Number of Inputs: twenty

Number Hidden layers: four

Number of neurons in each layer: sixty-four

Output Layer: Softmax

Number of output classes: seven

Note: In The architecture shown above, not all the connections shown for the sake of simplicity, but neural network is fully connected.

Soft Max function:

Softmax function calculates the probabilities distribution of the event over 'n' different events. This function will calculate the probabilities of each target class over all possible target classes. Later the calculated probabilities will be helpful for determining the target class for the given inputs.

$$\partial(z_i) = e^{z_i} / \sum_{j=1}^{K} e^{z_i}$$

Soft max function used at the output layer for the Multi class classification.

Neural Network Model –Step 1

- Created Fully connected Neural Network
- 32 neurons in each layer and 3 layers
- Tanh function is used as the activation function
- Number of neurons and layers decided based on trial and error basis
- Soft max layer at the output
- Trained network with 300 epochs with a batch size of 30000
- Trained the Model with the same dataset as the one used for the Decision Tree.
- No sampling techniques has been employed to capture the time dependence between the samples.
- A separate a set of files from the data are considered for the testing the model. The same data cleansing steps are performed on the test data files to create the test data set.

Results:

- Efficiency with the Test data is close to ~50%

Reason:

- Data is highly imbalanced and hence there is chance over fitting. So the model did not really performed well on the test data

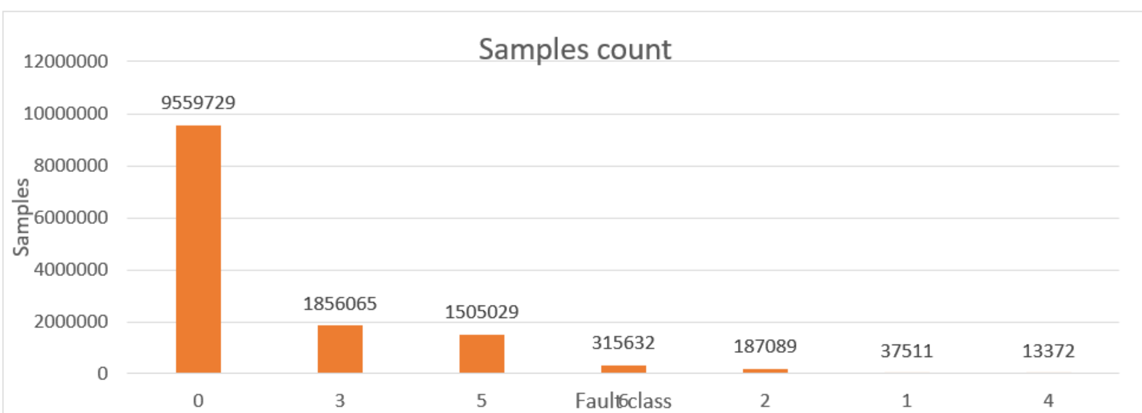

Fig. 4. Graph Representing Imbalance Dataset.

Neural Network Model –Step 2

Handling of Imbalance data

Class weights: It is clear from the figure 7, there is huge imbalance in the data. Class one and class 4-sample count are very less in comparison to the class 0 sample count. This can lead to over fitting; one of ways to increase the prominence for minority samples is adjust class weights of the minority classes. Class weights adjusted as per the sample count, more the number of samples less weight for the class.

TABLE 2

Class Weights

Class	Weight
0	0.02
1	0.25
2	0.15
3	0.06
4	0.3
5	0.1
6	0.12

Drop out of Neurons: After each layer of the neural network, 15% of the neurons are dropped out to avoid the over fitting of the model.

Number 15% is arrived by trial and error basis. Tried with different values between 5% and 25% and achieved better efficiency with 15% drop out of neurons.

Model Creation

Below three are the major changes performed in step 2 of neural network model creation

1. Adjusting class weights to handle imbalance data
2. Considering Fault criteria for the creation of data set. Followed same steps as mentioned in Data Cleansing
3. Drop out of neurons after the each layer to avoid over fitting of the Model

Test Data details

A separate a set of files from the original data considered for the testing the model. The same data cleansing steps performed on the test data files to create the test data set.

Neural Network Model details:

- Checked for the Fault Enable condition for each sample of the dataset
- For No Fault condition, sample is considered if at least one fault is enabled
- For Faulty sample, sample is added to dataset only when the specific fault is enabled
- Created Fully connected Neural Network
- 64 neurons in each layer and 4 layers
- 15% neurons dropped out after each layer to avoid overfitting
- Number of neurons and layers decided based on trial and error
- Soft max layer at the output
- Trained network with 300 epochs with a batch size of 30000
- Results:
- Efficiency with the Test data is close to ~61%
- Reason:
- Multiple files for the same driving pattern is considered.

With neural network model is step 2, efficiency of the model is not good and still model needs improvement. While analyzing the reason, found that multiple files for same scenarios are considered and tests covering different driving patterns needs to consider for the creation of data set. Hence decided further to analyze the impact different files considered for the dataset on the model creation.

Neural Network Model –Step 3

The whole data considered for creation of model predominantly has three kinds of files

1. Low ambient temperature recording
2. Recorded with Normal drive behavior
3. Standard driving cycles

Model Creation

Major change in step 3 is to consider the Standard drive cycle data for the creation of dataset.

Size of Data: 15 GB

Size of Data set after data cleansing 1.05GB

Test Data Details

A separate a set of file from the data are considered for the testing the model. Performed the same data cleansing steps test data files.

Created a test data of 500MB for testing the model

Model Details

Most of details are same

- Created Fully connected Neural Network
- 64 neurons in each layer and 4 layers
- Number of neurons and layers decided based on trial and error
- Soft max layer at the output
- Trained network with 300 epochs with a batch size of 30000
- Created a test data of 500mb
- Total number of test Samples:1906324

Results:

- Efficiency with the Test data is to ~92.55%

Plot accuracy versus Loss:

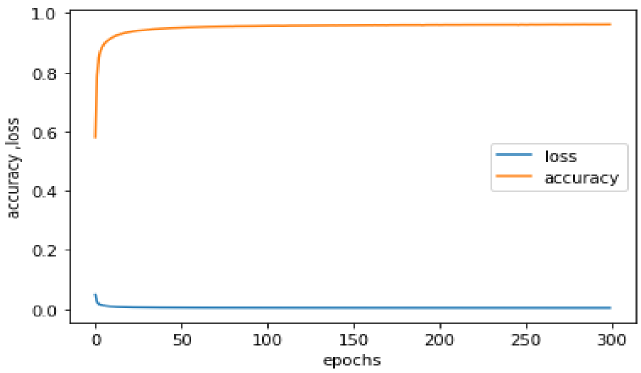

Fig. 5. Accuracy Loss versus Epochs.

Results on Test Data:

```
1906324/1906324 [==============================] - 66s 35us/step
Accuracy using MLP is
92.55703687667847
end of NN method evaluation

In [4]:
```

Fig. 6. Output.

Acknowledgements

My sincere thanks and grateful acknowledgement to **Mr. Tobias Erbes Manager, System & Technology HV Batteries, Mercedes-Benz AG** for his support in data collection, valuable suggestions and constant encouragement.

I take this opportunity to express my sincere thanks with deep indebtedness to my supervisor **Mr. Atul Gupta, Senior Program Manager, Mercedes Benz Research and Development India Private Ltd.** for his Valuable suggestions

Conclusion

Multi-Layer Perceptron Model for classifying Air Mass flow deviation in the Air System created successfully by making use of the available vehicle teste data and validated. An efficiency of 92.55% achieved with the current model. Further, Multi-Layer Perceptron Model can be improved by analyzing the reasons for the incorrect predictions by the model and model needs to be validated by collecting the test date from different vehicle operating conditions, different intensities of the fault level and across different engines.

References

[1] Tom M. Mitchell, Machine Learning, The McGraw-Hill Companies, Inc. International Edition. 1997. http://www.cs.cmu.edu/~tom/mlbook.html

[2] Christopher M. Bhisop, Pattern Recognition & Machine Learning, Springer, 2006. ISBN: 978-1-4939-3843-8. https://link.springer.com/book/9780387310732

[3] Julie Main, Tharam Dillon and Simon Shiu: A Tutorial on Case-Based Reasoning. https://dl.acm.org/doi/10.5555/357410.357787

Address correspondence to: *Mr. Karthik Chinnapolamada, Sr. Tech Lead, RDI/CEP, Mercedes Benz Research and Development Private Limited, Embassy Crest Phase-2, Whitefield Road, Bangalore*-560066, *India.*
Phone: 09901028983
E-mail: karthik.chinnapolamada@daimler.com

ARAI Journal of Mobility Technology
Volume 2 • Issue 2 • April–June, 2022, pp. 198-204
Research Paper
https://doi.org/10.37285/ajmt.1.2.5

Development and Implementation of Remote Duty Cycle Data Acquisition and Analysis

Sathish Kumar P., Kumar P. and Dayalan P.
Ashok Leyland Technical Centre, Vellivoyalchavadi, Chennai – 600103, India.

ABSTRACT

In the competitive automotive industry, launch of a new vehicle has become a norm to stay ahead, also the vehicle manufacturers are competing in terms of increased warranty on the new launch. Hence it is imperative for rigorous validation of new vehicle in very short period and requires to map customer usage pattern in least possible time.

This work is based on an extension of internet of things (IOT), which provides a tool of capturing vehicle duty cycle by using combination of analog and digital sensors with appropriate ADC. The system is enabled with algorithm/ coded to log result, whenever measured physical parameter goes above/below predetermined level. The work involves implementation of an auto start and auto shutdown of the system based on vehicle ignition. Thus, this paper presents a system that is capable of continuous, real time recording and edge computing (auto post processing) physical quantity and ensures complete elimination of human interface, thereby enabling Remote Data Acquisition, Analysis and Reporting system (Proposed system). The proposed system is fit and forget and cost-effective solution, it can be fitted in any number of vehicles to acquire data for large number of kilometers to map system level usage pattern. Against the conventional method with limited kilometers of data to map customer pattern. The present work is an implementation of Remote Data Acquisition, Analysis and Reporting system in measurement of required vehicle parameters of temperature and humidity in field working conditions.

KEYWORDS: Drag force; Vortex generator (VG); Aerodynamics forces; Flow separation; Velocity distribution; Pressure distribution; CFD.

Introduction

The global method for vehicle validation in automobile industry includes collection of road load data acquisition at different customer site and extrapolation of the collected data to predict the life of a vehicle component. But the quantum of the data used to predict the life is limited to only certain distance in certain geographical location while vehicle is used at all locations. There is a need for extensive data acquisition which maps the vehicle usability in maximum possible geographical condition for high level of confidence. But the current methodology of data acquisition is manual, laborious, costly, with this it is difficult to acquire data for all the geographical locations. Also, data acquisition and data post processing activity are carried out in series; which leads to prolonged product validation cycle.

The accomplishment of the vehicle durability assessment starts with understanding precisely about the load that the vehicle will undergo during their anticipated lifetime. RLDA/Duty Cycle is an excellent method to measure vehicle response for different working condition. The RLDA/Duty Cycle includes acceleration, deceleration, displacement, force and any other physical parameter or the combination of the parameters of the vehicle system. Depending on the vehicle system physical parameter is selected.

The proposed work presents an Internet of things (IOT) based system which includes raspberry pi coupled with a signal converter, GSM connectivity, power control circuit and processing algorithm. This system has wide accessibility as the user with internet connection can download/view the data/result from anywhere across the globe. Another important feature of this design is the reprogrammable and open source nature of the product; the program/application can be flashed remotely to incorporate the improvements in the underlying algorithm to suit the requirement.

The proposed system can be installed in many vehicle parallelly, as shown in Fig.1. with that it has an upper hand over the current method in terms of extent of data used to predict life/validate the system and the extrapolated results will be close to the real-life application. Vehicle validation depends on its subsystem validation, temperature and humidity are selected for the presented work.

ABBREVIATIONS: IOT - Internet of Things; RLDA - Road Load Data Acquisition; ADC - Analog to Digital Converter; GSM - Global System for Mobile; GPS - Positioning System

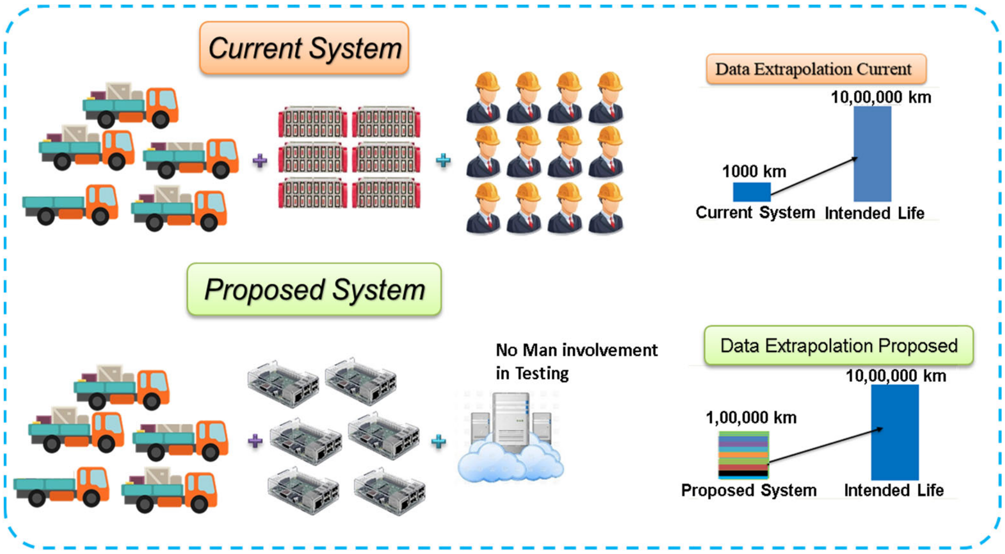

Fig. 1. Extent of data collection in current and proposed method.

Current Method of Data Acquisition for Duty Cycle Measurement

The important parameters for any duty cycle are required related measurement parameters which is useful to get insights for the particular duty cycle. Example parameters are temperature, pressure, speed, strain, force, displacement and humidity etc. Each duty cycle requires different set of parameters to perform the exercise. Fig.2 shows the current method for measurement data for duty cycle. The sensors for different measurement parameters are connected to the data logger.

Working of the system

The input sensors connected to the data loggers are handled by the test engineer and data is acquired during the vehicle movement. Acquired signals are checked for signal anomalies (if any) and are corrected. Then measured signal is calculated using pre-determined algorithms and software's and result is published in presentable format. Since data loggers available in the market are very costly, it needs a human interface to ensure safe operation of the system.

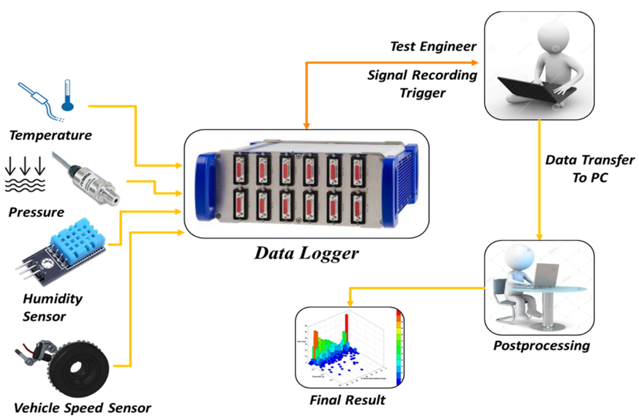

Fig. 2. Process flow for current method of duty cycle measurement.

The current method of data acquisition is laborious, costly and time-consuming and it is very difficult to use such a system to map customer usage pattern from all the geographical condition. Also, human interface is required for raw data handling and post processing of the data.

Proposed In-House Developed System Design and Architecture for Duty Cycle

The system is developed in-house with a concept of modularity. Major components of the system are made up of modules with integrated circuits. Each of these modules has a special function to perform in the system. There are various readily available, and few specifically developed modules used to actualize the project. Various components and modules are listed below in hardware subsystem design. The c and python programming languages are used to log the data, analyze, post process and upload the result to server.

Hardware Subsystem Design

1. **Raspberry pi:** It is used as the base system.
2. **Power Trigger Circuit:** Ignition is connected to raspberry pi and auto start stop module, auto start stop module includes a microcontroller which ensures power supply to the raspberry pi based on the ignition status.
3. **ADC or Signal Converters:** It is coupled to the raspberry pi to log different signal. Such as temperature board or ADC board
4. **Temperature, Humidity and Displacement sensor** are connected to the system for duty cycle inputs
5. **GPS module** is used to obtain geographical details of the vehicle movement
6. **GSM module** along with serial communication module used to upload the data to the cloud or server.

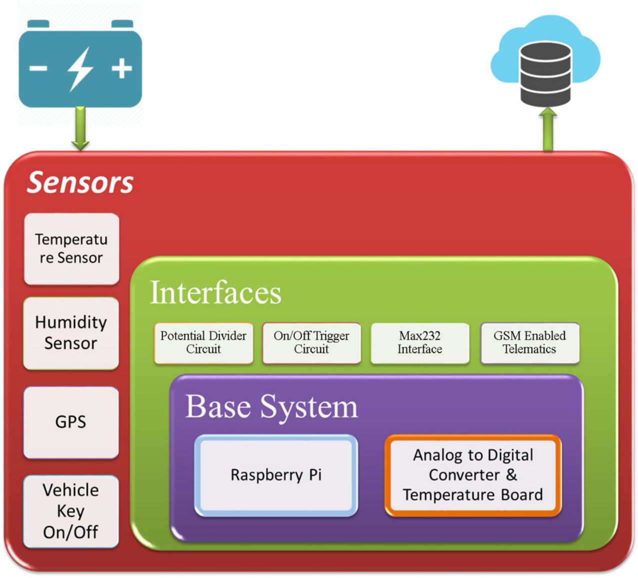

Fig. 3. Hardware details.

Software Subsystem Design

The software can be broadly divided into two parts data logging and data analyzing.

1. **Data logging:** - An application is developed in C or python language which records data from sensors through ADC at 1000 Hz sampling rate.
2. **Data analyzing:** - An application is developed using python which checks for the abnormality in the recorded data and calculates predetermined parameters as per the algorithm.
3. Both the applications are compiled and made auto executable during the boot-up of raspberry pi.

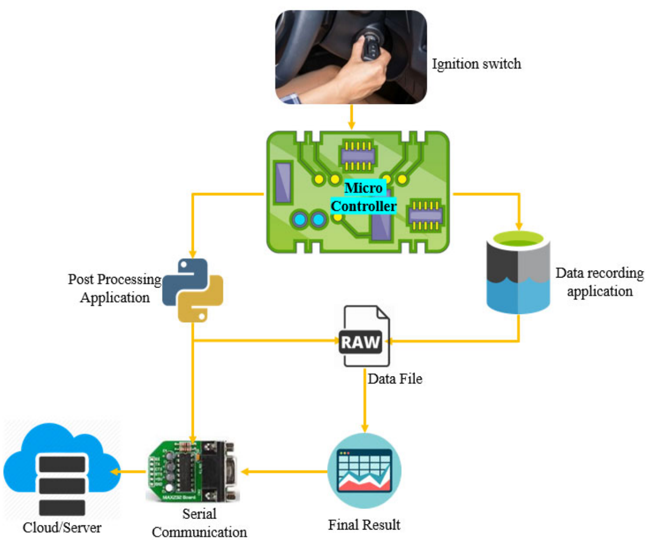

Fig. 4. Software flow for data recording and post-processing.

Working of the System

The raspberry pi is powered by the power trigger circuit, when the ignition is switched on and raspberry pi boots data logging and post processing application is activated. Concept of parallel computing is used to log sensor (connected to ADC) input by data logging application and parallelly post processing application computes the desired output results to the server based on the measured parameter. The raspberry pi (base system) which has been programmed, sends the temperature and humidity output to the GSM telematics, through serial communication and then the result gets uploaded to server. Once the vehicle is switched off, the system stops logging the data, it ensures that the last logged data is post processed and required results are sent to the server, and then switches off itself. Hence the system is fool proof and works without any human interface. Fig.5 shows the proposed process for duty cycle measurement.

System Validation

Dedicated calibration system used in the industry is used to validate the system. Calibration master and proposed systems are connected in the temperature calibration system for capturing temperature values. Simultaneous data acquisition was carried in both the systems during temperature increments. Data acquired from calibration master is compared with proposed system. Whereas in the proposed system, data is acquired and uploaded to the server.

Temperature values on both the system are then compared with temperature increment values (Refer Figure 6). Based on comparison, it is evident that the proposed system is in line with the existing proven system available in the industry.

Humidity sensor is checked by single point verification with calibrated humidity meter in ambient and dry air condition and found in line with the humidity meter. Displacement sensor is calibrated using the proposed system with respect to known displacement. After internal validation, the product is installed in field vehicle for real time.

Results and Discussion

After internal validation, the product is installed in field vehicle for real time measurements. Test data were acquired in on-road test vehicle. Measurement captured in proposed remote data acquisition system is processed internally and analyzed output is uploaded in cloud. Temperature data is measured in engine mount of vehicles mentioned in Figure 7 to study temperature distribution of engine mount in different category of vehicles

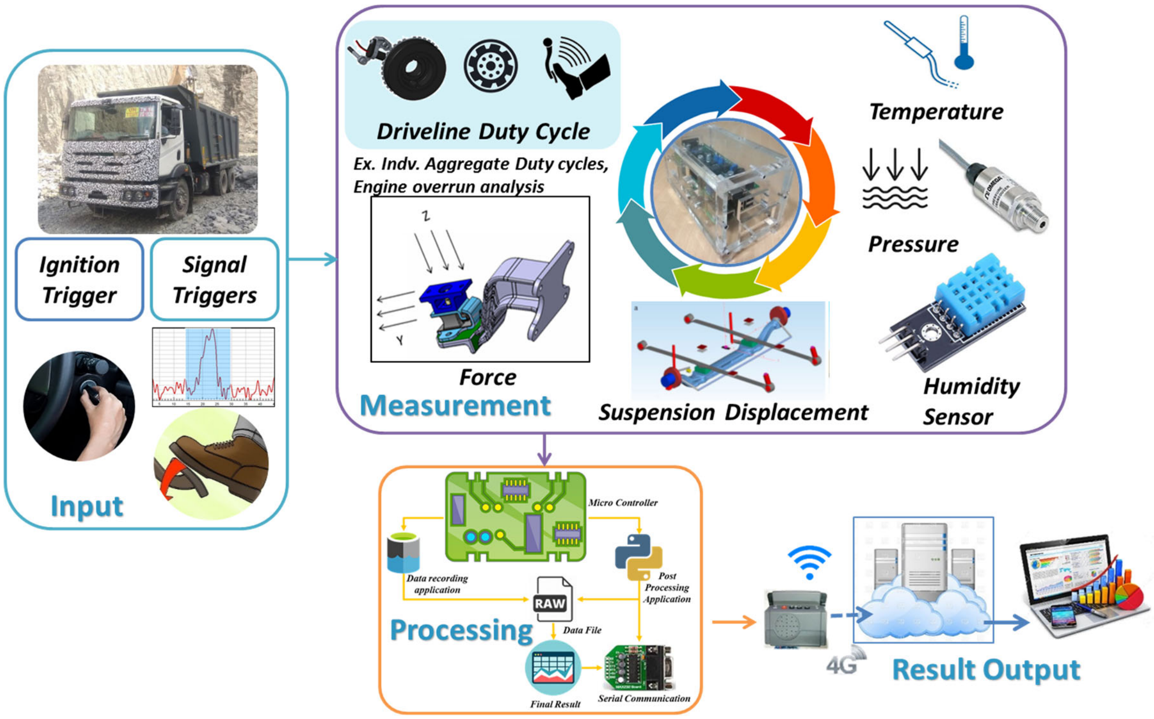

Fig. 5. Process flow for proposed method of duty cycle measurement.

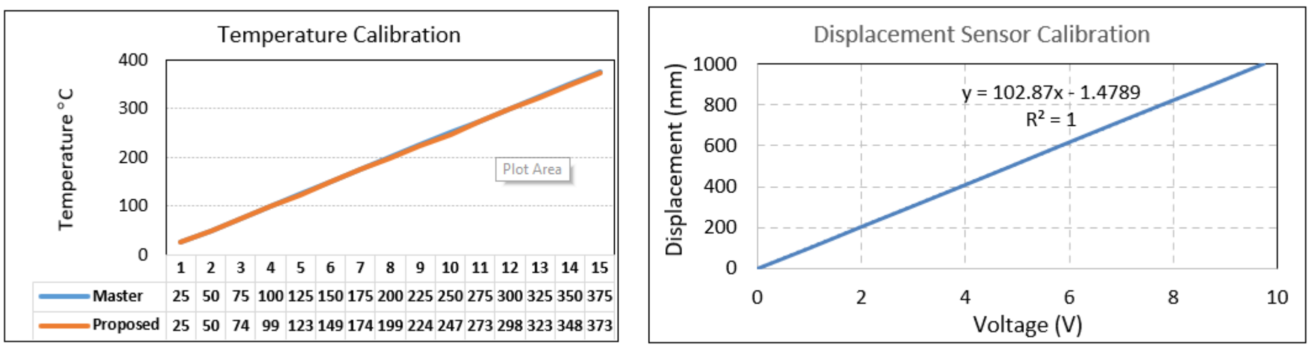

Fig. 6. Calibration and comparison of temperature and displacement value system.

Vehicle Model	Field Trial Details	Covered (Km)	Time (Hrs)
Vehicle A - MHCV	Route A	2000	30
Vehicle B - MHCV	Route B	3000	54
Vehicle C - MHCV	Route C	1400	21
Vehicle D - ICV	Route D	9000	180
Vehicle E - Passenger	Route E	2000	100

Fig. 7. Representative vehicle images and details of proposed system validation.

Processed output is then converted to graphical representation for ease of viewing, as shown in Fig 8. This provides information on temperature distribution throughout vehicle running condition in different weather and road events.

Humidity is measured inside the air tank of vehicle to study the humidity of air in different vehicle operating conditions. Humidity sensor and mounting image is shown in Fig 9.

Humidity measurement of vehicle air tank in vehicle running condition in continuous road operation shown in Fig 10.

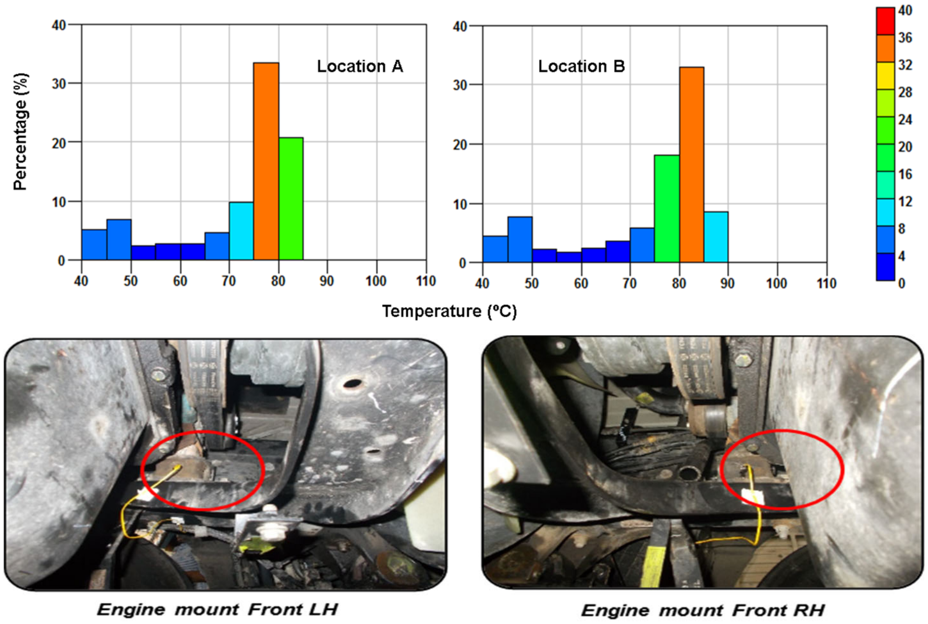

Fig. 8. Temperature measurement location and processed output results.

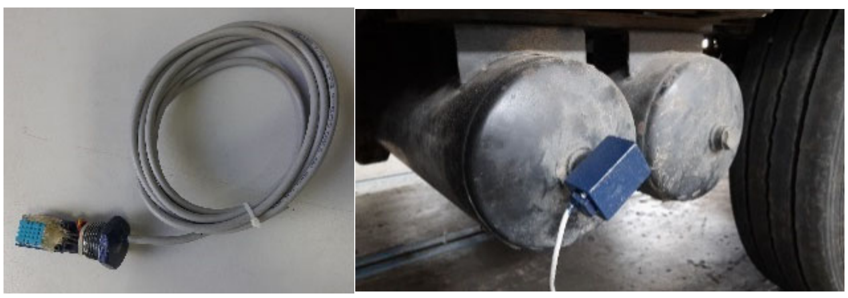

Fig. 9. Humidity sensor and mounting image.

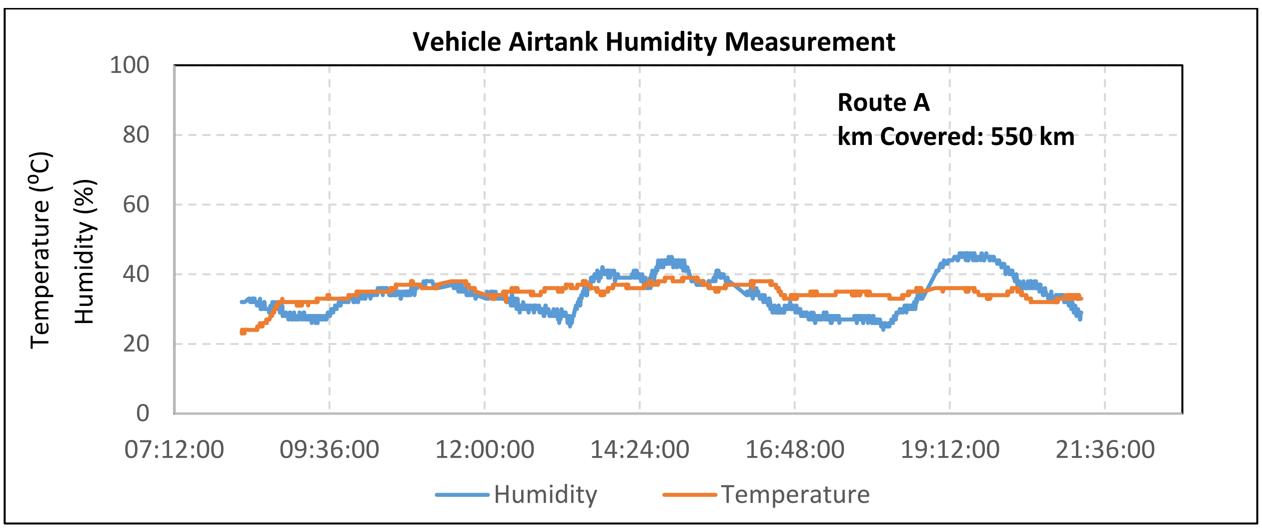

Fig. 10. Humidity measurement results vehicle operating condition.

Similar to temperature and humidity, displacement or any other analog voltage signals can be measured using the proposed remote data acquisition system. In figure 11 displacement sensor mounting and output distribution plot is shown. Raw measured displacement data is converted automatically in post processing and distribution output is stored.

The proposed system is cost effective, it can be installed in many vehicles in different operating conditions and data collated from all the regions can be used as a duty cycle input to validate the system.

Automated Post Processing of Signals

Measured signals using proposed system output data are analysed automatically and only processed output data are shared in the cloud. The measured data are usually larger in size due to higher measurement samplings and longer time recording. So handling of large amount of raw data outputs in remote and cloud is extremely difficult. Based on individual parameters measured, different analysis techniques are written in python code. Raw data recordings are captured in 1 Hrs of segment intervals and saved temporarily. Python code written in such a way that after every intervals of signals saved, post processing analysis code will be triggered and analysed.

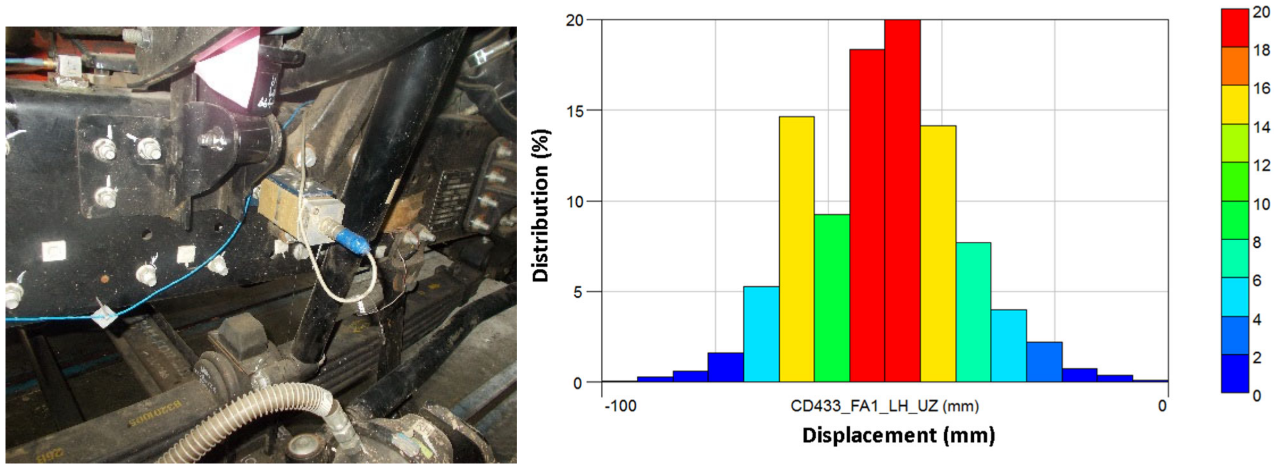

Fig. 11. Displacement measurement results in field vehicle running condition

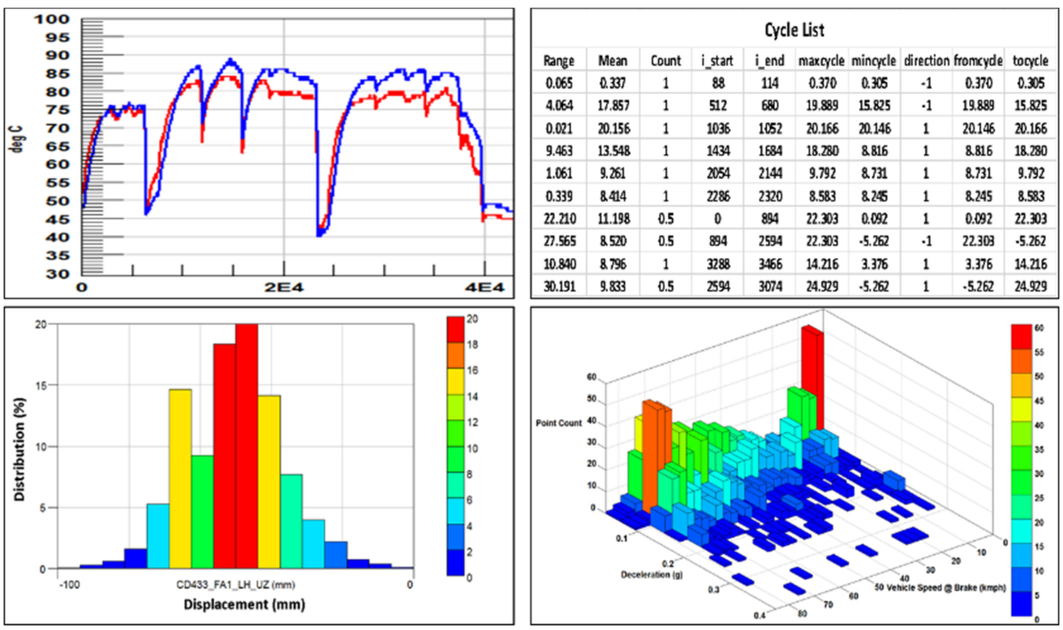

Cycle List									
Range	Mean	Count	i_start	i_end	maxcycle	mincycle	direction	fromcycle	tocycle
0.065	0.337	1	88	114	0.370	0.305	-1	0.370	0.305
4.064	17.857	1	512	680	19.889	15.825	-1	19.889	15.825
0.021	20.156	1	1036	1052	20.166	20.146	1	20.146	20.166
9.463	13.548	1	1434	1684	18.280	8.816	1	8.816	18.280
1.061	9.261	1	2054	2144	9.792	8.731	1	8.731	9.792
0.339	8.414	1	2286	2320	8.583	8.245	1	8.245	8.583
22.210	11.198	0.5	0	894	22.303	0.092	1	0.092	22.303
27.565	8.520	0.5	894	2594	22.303	-5.262	-1	22.303	-5.262
10.840	8.796	1	3288	3466	14.216	3.376	1	3.376	14.216
30.191	9.833	0.5	2594	3074	24.929	-5.262	1	-5.262	24.929

Fig. 12. Representative plots for automated processing results.

Automated post processing analysis takes care of converting raw data into required output results. Example, displacement signals are measured in 100 Hz (samplings per second) and recorded throughout vehicle running condition. This provide in GB size of raw data for a day. Handling this would be difficult in cloud, hence in post processing raw data is analysed and converted to peak and valley with index. Also rainflow distribution cycles are calculated for individual patches and temporary data is deleted. This post processed output data reduces data size drastically. Analysed output data are continuously collated and generates a rich data bank for product validation. All required results are provided directly without any additional requirement of manual post processing.

Advantages and Challenges

The system replaces the conventional data logger which requires human interface for data recording, data handling and post processing. Whereas the proposed system eliminates human interface for the above said activities. Unlike conventional IoT system which is limited to low frequency data acquisition, the proposed system is capable of handling high sampling (1000 Hz), real time post processing and Internet of thing-based data sharing to cloud opens many opportunities for the system in the field of RLDA.

1. The advantages of the proposed system are,
   a. Disruptive technology to replace high cost data acquisition system
   b. More amount of data collected from different terrain
   c. Post processing and data handling time is eliminated
   d. The system can be used for the measurement of different parameters and the capability of the system shown below
      i. Temperature study
      ii. Displacement study in suspension and other aggregates
      iii. Torque duty cycle
      iv. Critical strain location
      v. Force measurement on different aggregates
      vi. Road profile measurement
   e. Cost effective solution, the price of the system is Rs. 20,000 while data loggers available in the market costs minimum Rs. 5 lakhs.
   f. No human interface required in data logging
   g. Extended warranty based on customer usage pattern
2. The challenges with the system are,
   a. Not suitable for severe environmental conditions
   b. Ability to withstand for only lesser shock loads
   c. Lesser robust compared to existing dedicated systems

Fig. 13. Collated data from different terrain.

Future Scope

1. Bringing automation of handling the output and use of big data analytics to map terrain wise vehicle utilization
2. Increased channels for recording different parameter duty cycle together

Increasing system reliability for tough terrains Ability to withstand high shock loads.

Acknowledgements

The authors would like to thank the management of Ashok Leyland Ltd., for the extended support in the project. We would like to thank Mr. Balakrishnan D and Mr. Srinivasa Chandra, Ashok Leyland ltd., for supporting and guiding us in various stages of the project.

References

[1] Aniedu A. N., Ufoaroh S. U., Okechukwu G. N.. & Oranugo C. O. (2016), "Real Time Data Acquisition and Logging Using Gsm Technology", Advances in Multidisciplinary Research Journal. Vol. 2. No. 2, Issue 1 Pp 85-100, https://www.researchgate.net/publication/307477633_Real_Time_Data_Acquisition_and_Logging_Using_Gsm_Technology

[2] Peng Liu; Guojun Dai; Tingting Fu, (2007) "A Web Services Based Email Extension for Remote Monitoring of Embedded Systems," Software Engineering, Artificial Intelligence, Networking, and Parallel/Distributed Computing. SNPD 2007. 8, The ACIS International Conference on, vol.2, pp.412-416, July 30 -Aug. 1 2007. https://doi.org/10.1109/SNPD.2007.453

[3] Wijetunge, S.P.; Wijetunge, U.S.; Peiris, G.R.V.; Aluthgedara, C.S.; Samarasinghe, A.T.L.K, (2008) "Design and Implementation of a Bluetooth based General Purpose Controlling Module," Information and Automation for Sustainability, 2008. ICIAFS 2008. 4th International Conference on, vol., no., pp.206-211, 12-14 Dec. 2008. https://doi.org/10.1109/ICIAFS.2008.4783997

[4] Zhong, Xiaoyang & Liang, Yao. (2016). Raspberry Pi: An Effective Vehicle in Teaching the Internet of Things in Computer Science and Engineering. Electronics. 5. 56. 10.3390/electronics5030056. https://doi.org/10.3390/electronics5030056

[5] P Bhaskar Rao, S.K. Uma "Raspberry PI Home Automation with Wireless Sensors Using Smart phone". IJCSMC, Vol. 4, Issue. 5, May 2015, pg.797 – 803. https://www.ijcsmc.com/docs/papers/May2015/V4I5201599a70.pdf

[6] Jawad, B. and Nagy, K., "Remote Data Acquisition Using Audio, Video and Data Transmission," SAE Technical Paper 2001-01-2467, 2001, https://doi.org/10.4271/2001-01-2467.

Address correspondence to: *Mr. Sathish Kumar P., Ashok Leyland Technical Centre, Vellivoyalchavadi, Chennai – 600103, India.*
Ph: 09840136834
E-mail: SathishKumar.P22@ashokleyland.com

ARAI Journal of Mobility Technology
Volume 2 • Issue 2 • April–June, 2022, pp. 205-213
Research Paper
https://doi.org/10.37285/ajmt.1.2.6

Aerodynamic Effect on Stability and Lift Characteristics of an Elevated Sedan Car

Amrutheswara Krishnamurthy and Suresh Nagesh

PES University, Bangalore-560085, Karnataka, India

ABSTRACT

There is a strong interaction between air and vehicle components. Aerodynamics plays a significant role in a vehicle's fuel efficiency. The contact patch load between the tire and road is directly related to the vehicle load. In this research, the lift forces generated due to the additional wing attached to the car model with different spans and heights of the wing location from the car body is considered for study. The loads due to change in Angle of Attack (AOA) and their effect on the tire loads are studied. The upward vertical force produced from aerodynamic loads reduces the wheel load of the car virtually. A tire's coefficient of friction would decrease with upward vertical force. This balance load implies that a lightweight car would make more efficient use of its tires than a heavier car. ANSYS Fluent is used for the Computational Fluid Dynamics (CFD) study. The validation of airflow characteristics, lift and drag forces from simulations are done with wind tunnel testing data. Varying the angle of attack, wingspan, height between the car and the wing's lower surface, one can increase the capacity of the payload by 10% or fuel efficiency by 10% to 20%.

KEYWORDS: Aerodynamics,,Navier Stoke equation, Nozzle effect, Car-wing, Drag, Lift.

Introduction

Aerodynamics plays a vital role in the fuel efficiency and stability of the vehicle. The airfoil in sedan cars are utilized to create adequate stability; however, the fuel efficiency decreases. Stability is required to steer the vehicle at high speeds. While the vehicle is moving with constant velocity, the aerodynamic forces and the tire contact patch almost remain constant. More the contact patch, more stability and less fuel efficiency, and vice versa. The entire vehicle load transfer to the road via the contact patch between the road and tire. The vertical load [[5]] includes lift force and downward force. Force on each tire is proportional to vertical load and significantly influences the longitudinal and lateral forces

The idea to use a wing or Airfoil fitted to the Car at the Center is to make use of the space between the Car's upper surface and the lower surface of the Airfoil to cause a Venturi nozzle effect [11]. The difference between the lower pressure on the Wing's top surface and high pressure at the upper surface of the Car's body creates upward lift force. The Wing attached starts from the center position of the Car and extended until the rear end of the Car.

In the study performed by Ahmed et al., the ground vehicle type of bluff body [1] was analyzed. In an open wind tunnel test section, pressure measurements and force measurements were done. The drag comes from the slant [6], [24], and the vertical base surface of the rear end. Numerical investigations by Emmanuel Guilmineau [8], [9] show that the angle of the rear window has significant effects on the characteristics of the wake flow. The drag always affects the fuel consumption and minimizes with the proper aerodynamic shape of the vehicle. The work by W Hucho [10] shows that a vehicle's aerodynamic shape is resisting the airflow in highways, and pressure drag contributes to total drag as a major, which consumes about 50% of the vehicle's fuel at highway speeds. The low level of drag loads and increased lift loads adds to the fuel efficiency. In race car aerodynamics [12], [29], the lift forces in –ve z-direction pushes the Car downward with the negative angle of attack.

It is vitally important to design new era cars with good aerodynamic shape [13], [15] to reduce fuel consumption as much as possible. If it is an electric vehicle [17], increasing the range to avoid frequent charging on highways is very advantageous. The engine's efficiency, idle time reduction, the torque required to drive the wheel at a higher speed would also affect the fuel efficiency. This current study focused on the aerodynamic forces. This type of car design uses air stream as additional fuel, renewable energy.

The authors in the current paper studied the Car attached to a wing at the top surface of the Car and studied the aerodynamic forces. The novelty of the research is without increasing the coefficient of drag, with AOA less than 4 deg, lift forces are generated due to nozzle effect. The weight of the Car could be reduced virtually using the lift forces. The performed experiments and study revealed that increasing the wingspan increases the lift forces. The angle of attack is one of the parameters, and increasing the AOA, lift and drag forces significantly increased. The contact patch loads calculated using the lift and drag forces generated show that loads on the tires decrease. These loads help to evaluate the lateral and longitudinal loads at the contact patch. These loads would help to design a liter vehicle and improve fuel efficiency.

Tire Load Interaction

The main forces acting at the tire-road contact patch are longitudinal forces [2], [7], [19] lateral forces, and self-alignment torque. The ratio gives the coefficient of friction

$$\mu = \frac{F_{tx}}{(F_v)} \qquad \ldots(1)$$

Ftx is the force in the X direction, F_v, the vertical load. Therefore, the ratio μ is friction coefficient [28] depends on tire slip resulting from contact patch due to vertical load.

In the Pacejka [21] tire model, lateral force and aligning torque are calculated based on slip angle and longitudinal force, mainly dependent on normal force Fz which is transferred to the tire, ignoring the camber angle.

The overall tire deflection estimates by the vertical load divided by the vertical stiffness. The Tire deflection, longitudinal force, lateral force, and slip are depending on the vertical load on the wheel. The vehicle's power must be equal to the power of the driving wheels.

Fig. **1** shows the general schematic diagram of six DOF vehicle models.

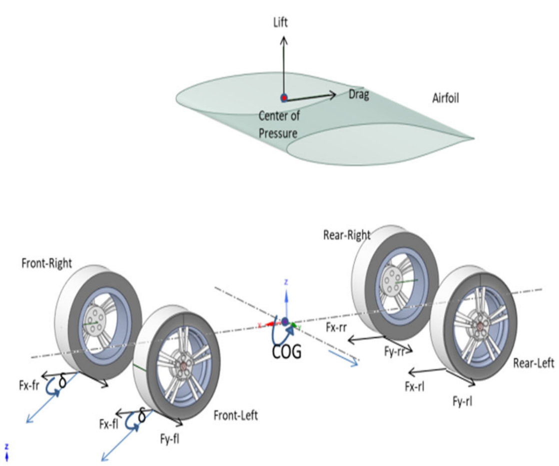

Fig. 1. The schematic diagram of six DOF vehicle model.

The basic equations describing the vehicle dynamics [4], [18] are as follows.

$$a_x = \frac{1}{m}[((Fx_{fl} + Fx_{fr})\cos\delta) - ((Fy_{fl} + Fy_{fr})\sin\delta) + (Fx_{rl} + Fx_{rr})] \qquad \ldots(2)$$

$$a_y = \frac{1}{m}[((Fx_{fl} + Fx_{fr})\sin\delta) + ((Fy_{fl} + Fy_{fr})\cos\delta) + (Fy_{rl} + Fy_{rr})] \qquad \ldots(3)$$

$$\frac{dr}{dt} = \frac{1}{I_{zz}}[((Fx_{fl} + Fx_{fr}) * a * \sin\delta) + ((Fy_{fl} + Fy_{fr}) * a * \cos\delta) - (Fy_{rl} + Fy_{rr}) * b - ((Fx_{fl} + Fx_{fr})\cos\delta * twf * 0.5 - ((Fx_{rl} - Fx_{rr}) * twr * 0.5] \qquad \ldots(4)$$

$$a_x = \dot{v}_x - v_y r \qquad \ldots(5)$$

$$a_y = \dot{v}_y + v_x r \qquad \ldots(6)$$

Where

v Speed of the Car
a Acceleration
r Yaw rate
F Force
δ Steering Angle

The indices refer to wheels

FL Front left
FR Front right
RL Rear left
RR Rear right
a Distance from CoG to the front axel
b Distance from CoG to the rear axel
twf Front track width
twr Rear track width
Izz Inertia around z-axis for the yaw movement

$$F_{wheels} = \frac{T_{Engine\ torque} * i_{Gear\ ratio} * \eta_{efficiency}}{r_d r_{dynamic}} = F_{Total\ Force} \qquad \ldots(7)$$

$$= F_{Airdrag} + F_{Rolling\ resistance} + F_{Inertia} + F_{Slope} \qquad \ldots(8)$$

As the vehicle speed increases, the load on the tires, rolling resistance, and drag forces [3] also increase. The drag mainly depends on the frontal design and area of the Car. Adding the Wing does not increase the frontal area significantly; however, it depends on the angle of attack. An increase in AOA results in higher drag force and less lift force.

$$F_{Air\ drag} = \frac{Cd_{coefficient\ drag} * S * \rho_{air} * \vartheta^2}{2} \qquad \ldots(9)$$

$$F_{Rolling\ resistance} = m_{(Kerb\ weight+Passengers)} * g * f_{rr} * \cos\propto \qquad \ldots(10)$$

frr is coefficient of rolling force, let us assume Slope angle

$$\alpha = 0 \quad F_{Inertia} = m_{(Kerb\ weight+Passengers)} * a * v \qquad \ldots(11)$$

Under constant acceleration, the term $F_{Inertia}$ ignored.

The lift force is not going to affect the frontal area calculations.

$$F_{lift} = \frac{Cl_{coefficient\ lift} * S * \rho_{air} * \vartheta^2}{2} \qquad \ldots(12)$$

The basic dynamic equation has the mass m in the denominator, which reduces due to the lift force.

The contact patch load for the front wheel is given by

$$F_{ContactPatch\_load} = \frac{m * g * (1 - \frac{CG}{WB}) *}{2} + F_S - \frac{F_{lift}}{4} + \frac{F_{Air\ drag * COG}}{4} \qquad \ldots(13)$$

Where Fs is the vertical suspension load, WB is the wheelbase. Drag loads due to Airfoil are transferred to the CG to calculate loads at the tire contact patch. As a result, the total load decreases due to the lift loads, reducing Fz loads and reducing the torque required to drive the wheels.

A setup for measuring the aerodynamic forces in a wind tunnel consists of a mechanism suitable for rigidly fixing the car model's position with the desired orientation up to ±30 degrees relative to the airstream. The wind tunnel facility has a maximum jet velocity speed of up to

45 m/s, and it is of an open-return design. The cross-sectional dimension of the nozzle area where the test model was placed is 600mm square. It has a glass window for visual observation of flow phenomenon. Wind tunnel equipped with a platform-type external strain gauge balance on which the model is to be mounted. All forces and moments were measured using a 3-component balance system. The model is fixed at the center position in this wind tunnel configuration, as shown in Fig. 3.

CFD

(a) **Meshing details:** The water-tight geometry has been used in the analysis from the Ansys space claim. The CFD mesh is generated using the following method. More fine resolution meshes were used around the vehicle. A body of influence is created around the vehicle, and a finer mesh size of 4 mm is used. Similarly, one more body of influence is created around the Airfoil with a small mesh to capture the flow separation and study the lift forces. Inflation layers are created around the Airfoil with the growth rate of 1.2. about the CFD model has 60 millions elements and 10 millions nodes for the purpose of analysis. Mesh independent study has been performed prior to finalizing this mesh type and size. Polyhedral mesh is used for discretization.

Computational fluid dynamics (CFD) analysis [8], [14], [25], [26], [27] is carried out to compare the results. The turbulence model k-ω SST model [16] is used in analyzing the flow characteristics of this computational problem. The default boundary conditions used in the CFD [17], [20], [22], [23] analysis.

The Turbulence Kinetic Energy model is calculated as shown in equation 14.

$$\frac{\partial k}{\partial t} + U_j \frac{\partial k}{\partial x_j} = P_k - \beta k\omega + \frac{\partial}{\partial x_j}\left[(\nu + \sigma\nu_T)\frac{\partial k}{\partial x_j}\right] \qquad \ldots(14)$$

(b) **NACA 66(2)015:** Symmetrical NACA 66(2)-015 Airfoil is attached to the car body. NACA 662-015 Airfoil has greater laminar flow than the 4 and 5 series, and this type of Airfoil has low drag. The minimum pressure location is at 0.6 chord length. CFD analysis is done to study the lift generated with various angles of attacks ANNEXURE – B:

The Y ordinate matches the centerline of the car body. The X ordinate of the Center of the pressure of the Wing measures the same as the Center of Gravity's (CG) Y ordinate. Due to this, there won't be any moment acting on the front and rear wheel axel. Only lift force reduces the load virtually on the car body, which reduces the overall load acting on the tires. The gap between the Airfoil and the Car's top surface is maintained so that the airflow is not affected, as shown in

Fig. 4. Only the Wing's angle of incidence is modified, where the Car is parallel to the x-axis.

Table 1 presents the coordinates used for the NACA 662015 symmetrical airfoil. At the same time, importing the coordinate points into the Fluent, adding one more point with Y ordinate as 0 to create a closed-end for the Airfoil as shown in the table. Units are in mm.

TABLE 1.

The coordinates of the NACA 662015 airfoil are attached to the car body.

X_Cord	Y_Cord	X_Cord	Y_Cord
0.00	0.0000	95.00	-0.5660
0.50	1.1220	90.00	-1.4800
0.75	1.3433	85.00	-2.5300
1.25	1.6753	80.00	-3.5980
2.50	2.2353	75.00	-4.2987
5.00	3.1000	75.00	-4.2987
7.50	3.7813	70.00	-5.5760
10.00	4.3580	65.00	-6.3720
15.00	5.2860	60.00	-6.9593
20.00	5.9953	55.00	-7.2833
25.00	6.5433	50.00	-7.4500
30.00	6.9560	45.00	-7.4953
35.00	7.2500	40.00	-7.4300
40.00	7.4300	35.00	-7.2500
45.00	7.4953	30.00	-6.9560
50.00	7.4500	25.00	-6.5433
55.00	7.2833	20.00	-5.9953
60.00	6.9593	15.00	-5.2860
65.00	6.3720	10.00	-4.3580
70.00	5.5760	7.50	-3.7813
75.00	4.2987	5.00	-3.1000
80.00	3.5980	2.50	-2.2353
85.00	2.5300	1.25	-1.6753
90.00	1.4800	0.75	-1.3433
95.00	0.5660	0.50	-1.1220
100.00	0.0000		

Test Model

In this study, a 1:18 scaled car model used is the Porche Panamera model, and technical details were taken from the Techart [30] and Porche website [31]. The model used in the windtunnel lab is a die-cast metal miniature scaled model but a very detailed, available in the market. The CAD data of the same was replicated using CATIA for the CFD analysis. The model is attached with the Airfoil with different wingspans at different heights.

The following parameters were studied.

Starting with a 100mm wingspan increased up to 300 mm in steps of 50mm. (100mm, 150mm, 200mm, 250mm, and 300mm) in total, five wings were fixed to the car body.

The distance between the Car's top surface and the Wing's lower surface for the aerodynamic effect is studied. Initially, it was 25 mm and then increased the height to 25mm, i.e., 25mm, 50mm, and 75mm. The angle of incidence varied as 0º, 5º, 8º, 15º degrees. However, the

Airfoil has a stalling angle of 16º; hence the study is limited to 15º.

Fig. 2. The Wind tunnel test facility.

Fig. 3. The Car body with the Airfoil attached in the wind tunnel test.

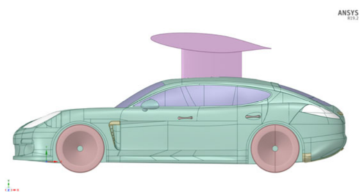

Fig. 4. Geometrical model of the Car body with the Airfoil attached.

Fig. **3** shows the scaled model in the wind tunnel lab with the Wing fixed on the top.

Fig. **4** shows the geometrical model used in the analysis.

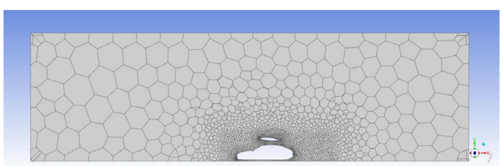

Fig. 5. The CFD model of the Car body with the Airfoil attached.

Fig. 6. The Pressure plot of the CFD model of Car.

Fig. **5** shows the polyhedral mesh with symmetrical modeling. Fig. **6** shows the pressure plot from the CFD simulation.

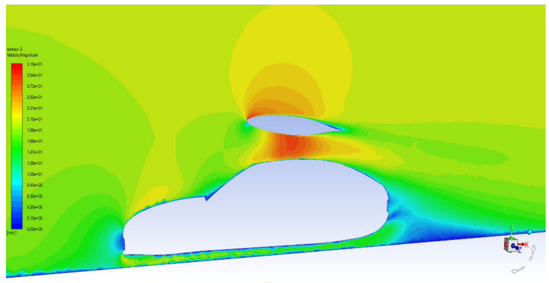

Fig. 7. The Velocity plot of the CFD model of Car.

Fig. **7** shows the velocity plot from the same simulation where drag remains the same, but the lift force is improved.

Results and Discussion

(a) **Wind Tunnel Results:** Results obtained from the CFD study and results from the wind tunnel tests are discussed in detail here. The graph shown in Fig. **8** depicts that an increase in the wingspan increases the lift force for a given airflow velocity. In this experiment, AOA is kept constant at 5º degrees, and the wingspan is varied, and the airflow velocity increased from 1m/s to 20m/s.

Table 2 presents the lift forces measured in the WindTunnel test with the different wingspans attached to the car body where the angle of attack is kept constant.

TABLE 2.

The Wind tunnel test result values of the car model with airfoil attached

Velocity	**100mm**	**150mm**	**200mm**	**250mm**
(m/s)	Lift (N)	Lift (N)	Lift (N)	Lift (N)
1.14	0.03	0.02	0.03	0.01
2.3	0.03	0.02	0.01	0.09
4.15	0.06	0.05	0.12	0.24
5.76	0.12	0.13	0.29	0.37
7.3	0.17	0.25	0.48	0.85
9.07	0.25	0.35	0.77	1.01
10.7	0.34	0.46	1.04	1.81
12.2	0.48	0.61	1.37	1.91
13.01	0.52	0.72	1.61	2.22
13.9	0.64	0.92	1.78	2.52
14.76	0.69	1.09	1.95	2.79
15.9	0.88	1.16	2.21	3.12
16.5	1.05	1.29	2.45	3.40
17	1.14	1.36	2.71	3.80
18	1.21	1.46	2.91	4.23
19	1.29	1.56	3.04	4.43

The results show in Fig. **9** are the results of the experiments done in the wind tunnel for the Car attached with the Wing, of span 100mm and Wing alone analyzed using the CFD software Fluent. The investigation was carried out by varying the air velocity from 1m/s to 20 m/s keeping the angle of attack at 5 deg. This lift force increase shows that the nozzle effect obtained from the lift is higher than the only Wing lift forces.

The graphs in Fig. **10** depict the relationship between the Wing attached to the Car and the aerodynamic forces. Observed that when the angle of attack is less than 10°, an upward force is generated and increases with the angle of attack. Here in this experiment Wing span used is 200mm, and varied the angle of attack is 5 and 8 degrees. The lift loads increase 22% when the angle of attack is changed from 5 degrees to 8 degrees, with the vehicle's speed is around 70kmph.

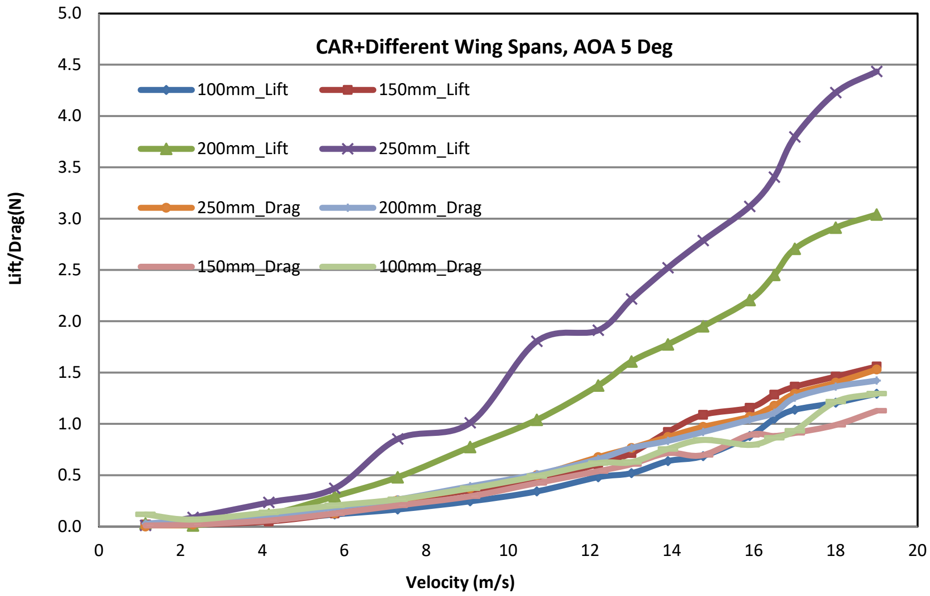

Fig. 8. Lift vs. velocities for symmetric Airfoil attached to CAR with different wingspans.

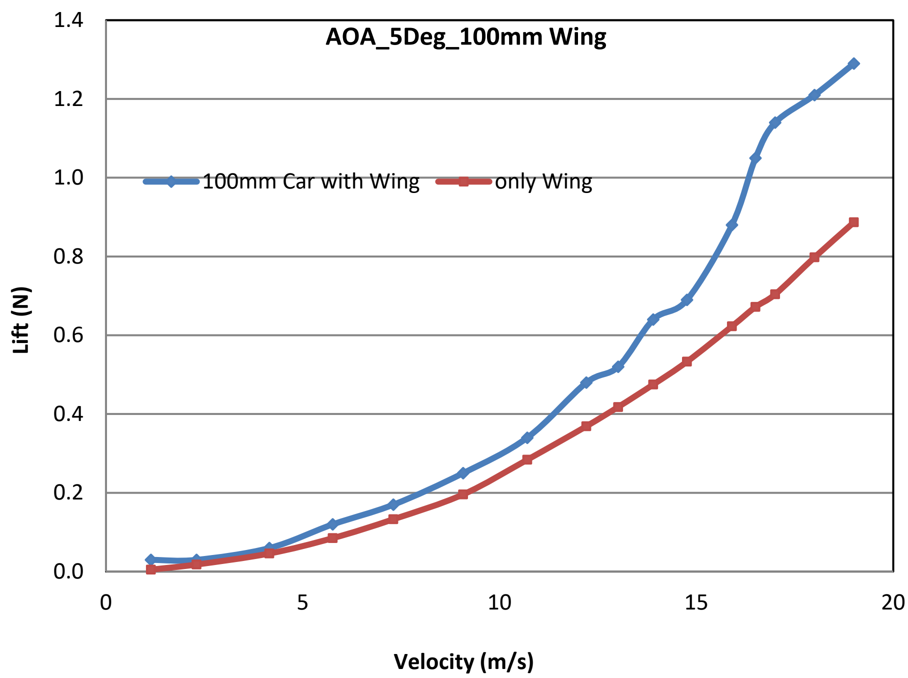

Fig. 9. Lift vs. velocities for Airfoil attached to CAR and Only Wing without a car.

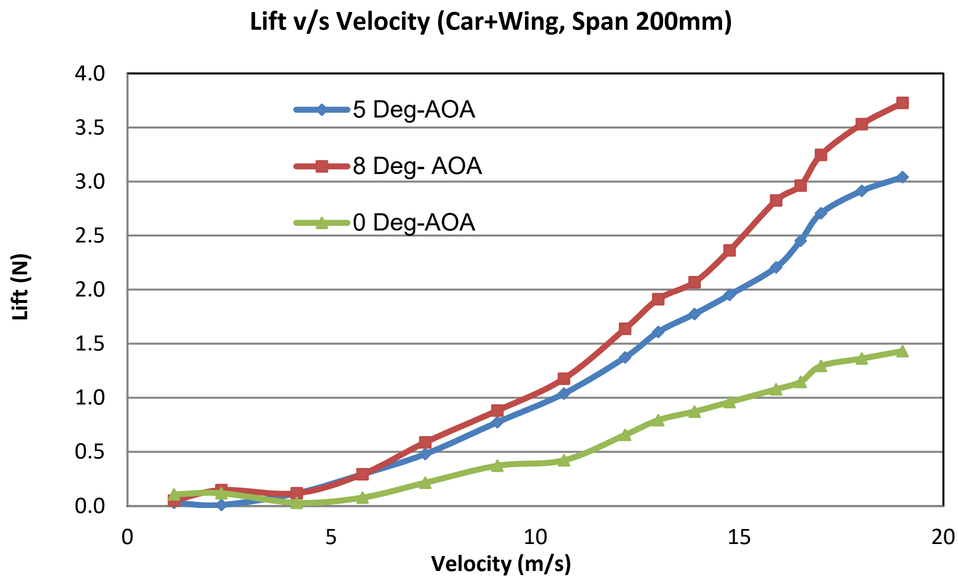

Fig. 10. Lift vs. velocities for symmetric Airfoil attached to CAR with different angles of attack.

Further, Fig. **11** shows that the lift forces generated decrease when the height between the Wing's lower surface and the car body increases. In this experiment, height is varied from 25 mm to 50 mm. and velocity from 1m/s to 40 m/s. The distance from the ground level is increased by 24% approximately. The lift loads generated decreased by 8.3% at the speed of 40m/s with the angle of attack 8 degrees. This curve shows that the nozzle effect reduces, and hence the total lift generated decreases as the height increases. The results shown in this curve are related to wind tunnel experiment results. The height increased to 75mm, and the results are much more similar to 50mm; hence, the optimum height is essential to utilize the nozzle effect.

CFD Results validation

We used high-performance computing machines for the CFD analysis. The results obtained from CFD analysis and Wind tunnel experiments are compared here in Fig. **12**. The CFD results for 3D Wingspan 250mm with 8 Deg of AOA and Wind Tunnell results showed an error of ±1.5% in Wind tunnel results.

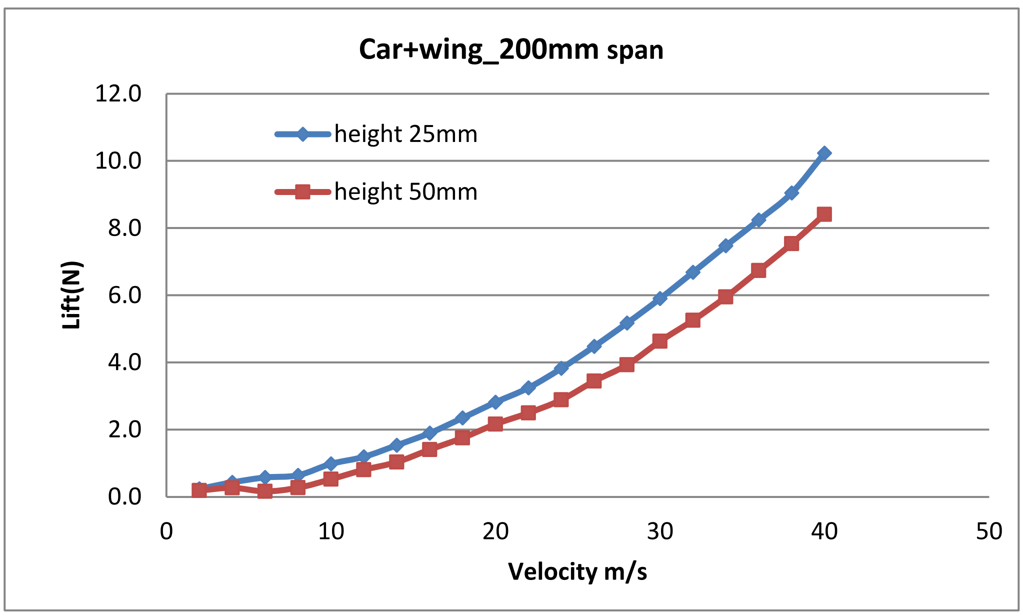

Fig. 11. Lift vs. velocities for symmetric Airfoil attached to CAR with a different height between Car and the Airfoil.

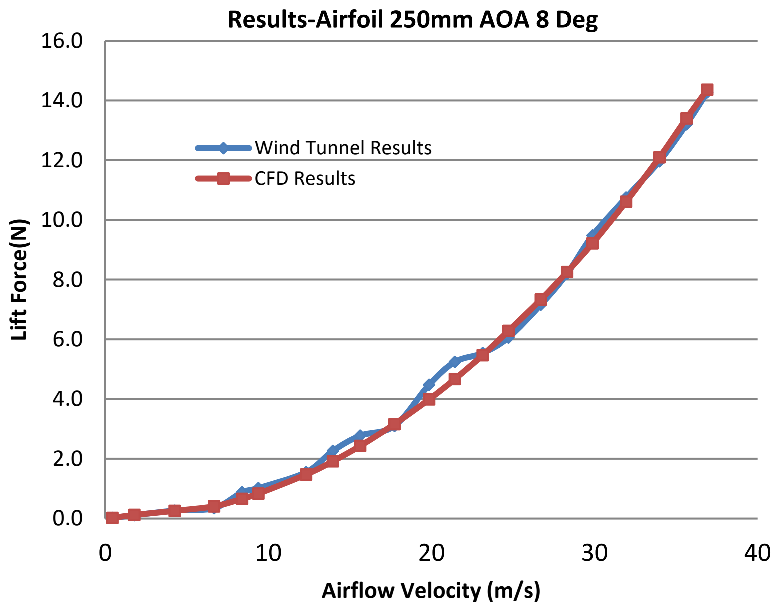

Fig. 12. Error in Measurements, Lift vs. velocities for Airfoil with wingspan 250mm and AOA 8 Deg.

Experiments were performed and compared using the wind tunnel to study the behavior with different wingspans attached to the car body. The aerodynamic lift loads from the Airfoil to the load balance measurement are transferred through the car body, as depicted in Fig. 3. The Car is mounted to strain gauge balance at the Center of the car bottom and through which aerodynamic loads are transferred and measured. This mounting depicts that a car with the airfoil attachment could pass the lift forces to wheel axels. Longitudinal forces and lateral forces are related directly as per equation 13. As Fz (vertical) loads reduce, the fuel efficiency increases; however, the lift is directly proportional to the square of the vehicle's velocity. The more the lift force, the more the vehicle gets into the unstable mode. Hence study has been done up to 130kmph of airspeed in the wind tunnel test. In general increase in lift and a decrease in drag are shown to increase fuel efficiency.

Since the Car model used in this study is a 1:18 scaled model. The NACA 662015 airfoil of a 200mm wingspan is up-scaled to normal dimensions, i.e.18, and with that, the wingspan measures to be 3.6m. Wingspan was analyzed using CFD, which shows that it generates 2775N lift force at 36m/s airspeed and 5º of AOA. After converting this lift force into kg, it is almost 282kg, virtually reducing weight. The car models of this size have a Kerb weight of approximately 2450kg. Hence the airlifted weight would be 11.5%. In turn, reduction in fuel consumption per 100km = 282 x (0.4/100) = 1.1 L/100km.

Summary/Conclusions

A Car fitted with a simple wing on the top surface with different wingspans and AOA is studied in this paper. The measured load depicts the increase in wingspan influences the lift loads. Computed contact patch loads due to virtually decreased weight, aerodynamic drag, and lift loads show that the loads on each tire reduced. The Venturi nozzle effect generates lift force at zero degrees of angle of attack and no drag. The lift loads reduce the loads on the contact patch, which adds to the 10% fuel efficiency.

Acknowledgement

Sunshine Measuring Instruments Pvt Ltd partially supported this research by providing the wind tunnel setup and the models. We are also grateful to Dr. TR Sitharam and Dr. Prabhu for their guidance.

References

[1] Ahmed, S., Ramm, G., & Faltin, G. (1984). Some Salient Features Of The Time-Averaged Ground Vehicle Wake. SAE Technical Paper Series, 473–503. https://doi.org/10.4271/840300

[2] Baffet, G., Charara, A., & Lechner, D. (2009). Estimation of vehicle sideslip, tire force and wheel cornering stiffness. Control Engineering Practice, 17(11), 1255–1264. https://doi.org/10.1016/j.conengprac.2009.05.005

[3] Bayındırlı, C., & Çelik, M. (2018). The Experimentally and Numerically Determination Of The Drag Coefficient Of A Bus Model. International Journal of Automotive Engineering and Technologies, 7(3), 117–123. https://doi.org/10.18245/ijaet.486409

[4] Department of Automatic Control Lund Institute of Technology, & Gerard, M. (2006). Tire-Road Friction Estimation Using Slip-based Observers (ISRN LUTFD2/TFRT--5771--SE). http://lup.lub.lu.se/luur/download?func=downloadFile&recordOId=8847816&fileOId=8859385

[5] Dominy, R. G. (1992). Aerodynamics of Grand Prix Cars. Proceedings of the Institution of Mechanical Engineers, Part D: Journal of Automobile Engineering, 206(4), 267–274. https://doi.org/10.1243/pime_proc_1992_206_187_02

[6] Gaylard, A., Kabanovs, A., Jilesen, J., Kirwan, K., & Lockerby, D. (2017). Simulation of rear surface contamination for a simple bluff body. Journal of Wind Engineering and Industrial Aerodynamics, 165, 13–22. https://doi.org/10.1016/j.jweia.2017.02.019

[7] Gillespie, T. D. (1992). Fundamentals of Vehicle Dynamics. SAE International.

[8] Guilmineau, E. (2014). Numerical Simulations of Flow around a Realistic Generic Car Model. SAE International Journal of Passenger Cars - Mechanical Systems, 7(2), 646–653. https://doi.org/10.4271/2014-01-0607

[9] Guilmineau, E. (2018). Effects of Rear Slant Angles on the Flow Characteristics of the Ahmed Body by IDDES Simulations. SAE Technical Paper Series, 001–0010. https://doi.org/10.4271/2018-01-0720

[10] Hucho, W., & Sovran, G. (1993). Aerodynamics of Road Vehicles. Annual Review of Fluid Mechanics, 25(1), 485–537. https://doi.org/10.1146/annurev.fl.25.010193.002413

[11] Huminic, A., Huminic, G., & Soica, A. (2012). Study of aerodynamics for a simplified car model with the underbody shaped as a Venturi nozzle. International Journal of Vehicle Design, 58(1), 15. https://doi.org/10.1504/ijvd.2012.045927

[12] Katz, J. (2006). AERODYNAMICS OF RACE CARS. Annual Review of Fluid Mechanics, 38(1), 27–63. https://doi.org/10.1146/annurev.fluid.38.050304.092016

[13] Kim, I., & Chen, H. (2010). Reduction of aerodynamic forces on a minivan by a pair of vortex generators of a pocket type. International Journal of Vehicle Design, 53(4), 300. https://doi.org/10.1504/ijvd.2010.034103

[14] Mansour, H., Afify, R., & Kassem, O. (2020). Three-Dimensional Simulation of New Car Profile. Fluids, 6(1), 8. https://doi.org/10.3390/fluids6010008

[15] Matsumoto, D., Kiewat, M., Haag, L., & Indinger, T. (2018). Online Dynamic Mode Decomposition Methods for the Investigation of Unsteady Aerodynamics of the DrivAer Model (First Report). International Journal of Automotive Engineering, 9(2), 64–71. https://doi.org/10.20485/jsaeijae.9.2_64

[16] Menter, F. R. (1994). Two-equation eddy-viscosity turbulence models for engineering applications. AIAA Journal, 32(8), 1598–1605. https://doi.org/10.2514/3.12149

[17] Nabil, T., Helmy Omar, A. B., & Mohamed Mansour, T. (2020). Experimental Approach and CFD Simulation of Battery Electric Vehicle Body. International Journal of Fluid Mechanics & Thermal Sciences, 6(2), 36. https://doi.org/10.11648/j.ijfmts.20200602.11

[18] Milliken, W. F. (1995). [Race Car Vehicle Dynamics (Premiere Series)] [Author: William F. Milliken] [December, 1995]. SAE International.

[19] Olson, B., Shaw, S., & Ste'pa'n, G. (2003). Nonlinear Dynamics of Vehicle Traction. Vehicle System Dynamics, 40(6), 377–399. https://doi.org/10.1076/vesd.40.6.377.17905

[20] Romijn, T., Hendrix, W., & Donkers, M. (2017). Modeling and Control of a Radio-Controlled Model Racing Car. IFAC-PapersOnLine, 50(1), 9162–9167. https://doi.org/10.1016/j.ifacol.2017.08.1726

[21] Ružinskas, A., & Sivilevičius, H. (2017). Magic Formula Tyre Model Application for a Tyre-Ice Interaction. Procedia Engineering, 187, 335–341. https://doi.org/10.1016/j.proeng.2017.04.383

[22] Strangfeld, C., Wieser, D., Schmidt, H. J., Woszidlo, R., Nayeri, C., & Paschereit, C. (2013). Experimental Study of Baseline Flow Characteristics for the Realistic Car Model DrivAer. SAE Technical Paper Series, 2342–2350. https://doi.org/10.4271/2013-01-1251

[23] Targosz, M., Skarka, W., & Przystałka, P. (2018). Model-Based Optimization of Velocity Strategy for Lightweight Electric Racing Cars. Journal of Advanced Transportation, 2018, 1–20. https://doi.org/10.1155/2018/3614025

[24] Tunay, T., Sahin, B., & Ozbolat, V. (2014). Effects of rear slant angles on the flow characteristics of Ahmed body. Experimental Thermal and Fluid Science, 57, 165–176. https://doi.org/10.1016/j.expthermflusci.2014.04.016

[25] Varney, M., Passmore, M., Wittmeier, F., & Kuthada, T. (2020). Experimental Data for the Validation of Numerical Methods: DrivAer Model. Fluids, 5(4), 236. https://doi.org/10.3390/fluids5040236

[26] Varshney, H. (2017). Aerodynamic Drag Reduction of Tractor-Trailer using Wishbone Type Vortex Generators. International Journal for Research in Applied Science and Engineering Technology, V(IX), 1833–1846. https://doi.org/10.22214/ijraset.2017.9266

[27] Viswanathan, H. (2021). Aerodynamic performance of several passive vortex generator configurations on an Ahmed body subjected to yaw angles. Journal of the Brazilian Society of

Mechanical Sciences and Engineering, 43(3), 25–31. https://doi.org/10.1007/s40430-021-02850-8

[28] Wang, R., & Wang, J. (2013). Tire–road friction coefficient and tire cornering stiffness estimation based on longitudinal tire force difference generation. Control Engineering Practice, 21(1), 65–75. https://doi.org/10.1016/j.conengprac.2012.09.009

[29] Zhang, X., Toet, W., & Zerihan, J. (2006). Ground Effect Aerodynamics of Race Cars. Applied Mechanics Reviews, 59(1), 33–49. https://doi.org/10.1115/1.2110263 Haslam, E. Shikimic Acid Metabolism and Metabolites, John Wiley & Sons: New York, 1993.

[30] Techart for the Panamera models. (n.d.). Techart. https://www.techart.de/en/models/panamera/techart-for-970/

[31] Porsche Panamera 4S. (n.d.). Porsche AG - Dr. Ing. h.c. F. Porsche AG. https://www.porsche.com/international/models/panamera/panamera-models/panamera-4s/

ANNEXURE – A:

Boundary conditions

Velocity Inlet	
Velocity Specification Method	Magnitude and direction
Velocity Magnitude	30 m/s
X-Component of flow direction	1
Specification Method	Intensity and Viscosity Ratio
Back Flow Turbulent Intensity (%)	5
Back Flow Turbulent Viscosity Ratio	10
Reference Values	
Compute from	Inlet
Area (m^2)	0.25617m^2
Density (kg/m^3)	1.225
Viscosity (kg/m-s)	1.7894E-05
Reference Zone	
Solution Methods	
Scheme	Coupled
Gradient	Least Square Cell Based
Pressure	Second Order
Momentum	Second Order Upwind
Turbulent Kinetic Energy	Second Order Upwind
Specific Dissipation Rate	Second Order Upwind

ANNEXURE – B:

CFD analysis of the NACA662015

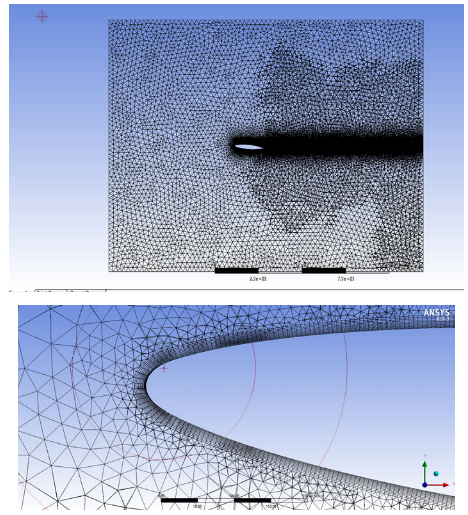

CFD Mesh

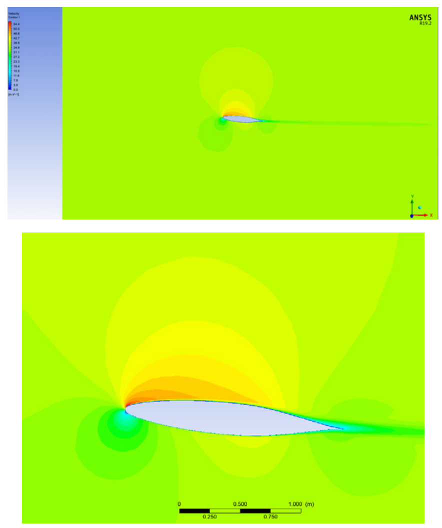

Velocity Contour

Address correspondence to : *Mr. Amrutheswara Krishnamurthy, Research Scholar, PES University, Bangalore-560085, Karnataka, India*
Email: amruthisac@gmail.com
Phone: 09900523702

ARAI Journal of Mobility Technology
Volume 2 • Issue 2 • April–June, 2022, pp. 214-219
Research Paper
https://doi.org/10.37285/ajmt.1.2.7

Design & Development of Electro Hydraulic Control Valve for Integration of Hoist and Steering System of a Dump Truck (35t)

Sathyarayana H. D., Kamasani Bujji Babu, Renukaraj Y. M., Ankit Shrivastava and Mahadevan B.

Research & Development, BEML, Ltd, Mysuru, Karnataka, India.

ABSTRACT

The intent of this paper is to propose a system to control the steering operation and hoist operation of the Dump truck through combination of electro hydraulic valves and priority valve housed in Integrated manifold block. Electro hydraulic control valve(EHCV), and Electronic controller unit (ECU) for steering and hoist operation of the dump truck. The orbitrol valve consists of load sensing line, when the Orbitrol valve sense an effort on the steering wheel by the operator, the load sensing line will give a feedback signal to the electro hydraulic valve, which will divert the pressurized hydraulic oil to the steering system for steering operation, else the hydraulic oil is available for hoist operation. The hoist operation is control through Electronic Controller Unit (ECU). If there is no signal from the controller for hoist operation the hydraulic oil will flow back to tank. The Electronic controller will energize the combination of solenoid operated valves, depending upon the input received from operator through the momentary switch (Raise Switch, Lower/Float Switch, Hold Switch) mounted inside the cabin, which will allow the flow of pressurized hydraulic oil to the hoist cylinder for body raise and lower operation through electro hydraulic control valve. The electronic controller memorizes the signal from momentary switch and energizes the solenoids as per the logic till the next input signal receive by controller.

KEYWORDS: Electro Hydraulic Control Valve (EHCV) Steering Control Unit (SCU), Electronic Controller, Load Sensing Unit, Priority Valve, Dump Truck.

Introduction

In the existing hoist system, hoist operation is carried out through air over hydraulic system. As air is the primary source for hoist operation, operator has to wait for the pressurized air to build up required for hoist operation. The system having external priority valve to control the flow of pressurized oil for hoist or steering operation. With the recent advancement in the hydraulic system the hoist and steering operation along with priority valve is integrated into the single unit. The introduction of Electro Hydraulic Control Valve (EHCV) in dump truck will control the hoist and steering operation. The EHCV unit consist of inbuilt priority valve which will provide the pressurized oil for steering or hoist operation depending upon the operator input.

Objective

- To reduce the operator effort require for steering operation using EHCV.
- To easily control the position of dump body by using EHCV, ECU and momentary electric switch
- To provide safety for hoist operation during equipment movement.
- Modular family concept to increase the interchangeability of individual valves.
- To make Hoist system more reliable and rugged.
- Soft buttons/switches to apply / release Hoist system.

Steering System:

The steering system consists of Steering Wheel, Steering Control Unit (SCU) and Electro Hydraulic Control Valve (EHCV) for steering operation of the dump truck. The SCU consists of load sensing valve, which is connected to the electro hydraulic control valve (EHCV). When the SCU sense an effort on the steering wheel by the operator, the load sensing line will get pressurize (125bar) and will give a feedback signal to the electro hydraulic control valve. The priority valve in EHCV will sense the load from SCU then it will divert the

ABBREVIATIONS: ECU - Electronic Control Unit; EHCV - Electro Hydraulic Control Valve; SCU - Steering Control Unit.

pressurized oil (125bar) from pump to steering cylinder through SCU for steering operation.

Hydraulic circuit with Electro Hydraulic Control Valve (EHCV) of the dump truck is shown in Figure 1.

The Pressure & Oil flow details of EHCV are below

1. Controlled flow from Priority valve is of 76 lpm
2. Maximum input flow to the valve is 202 lpm
3. Relief pr. for steering circuit is 125 bar
4. Hoist relief pressure is 175 bar

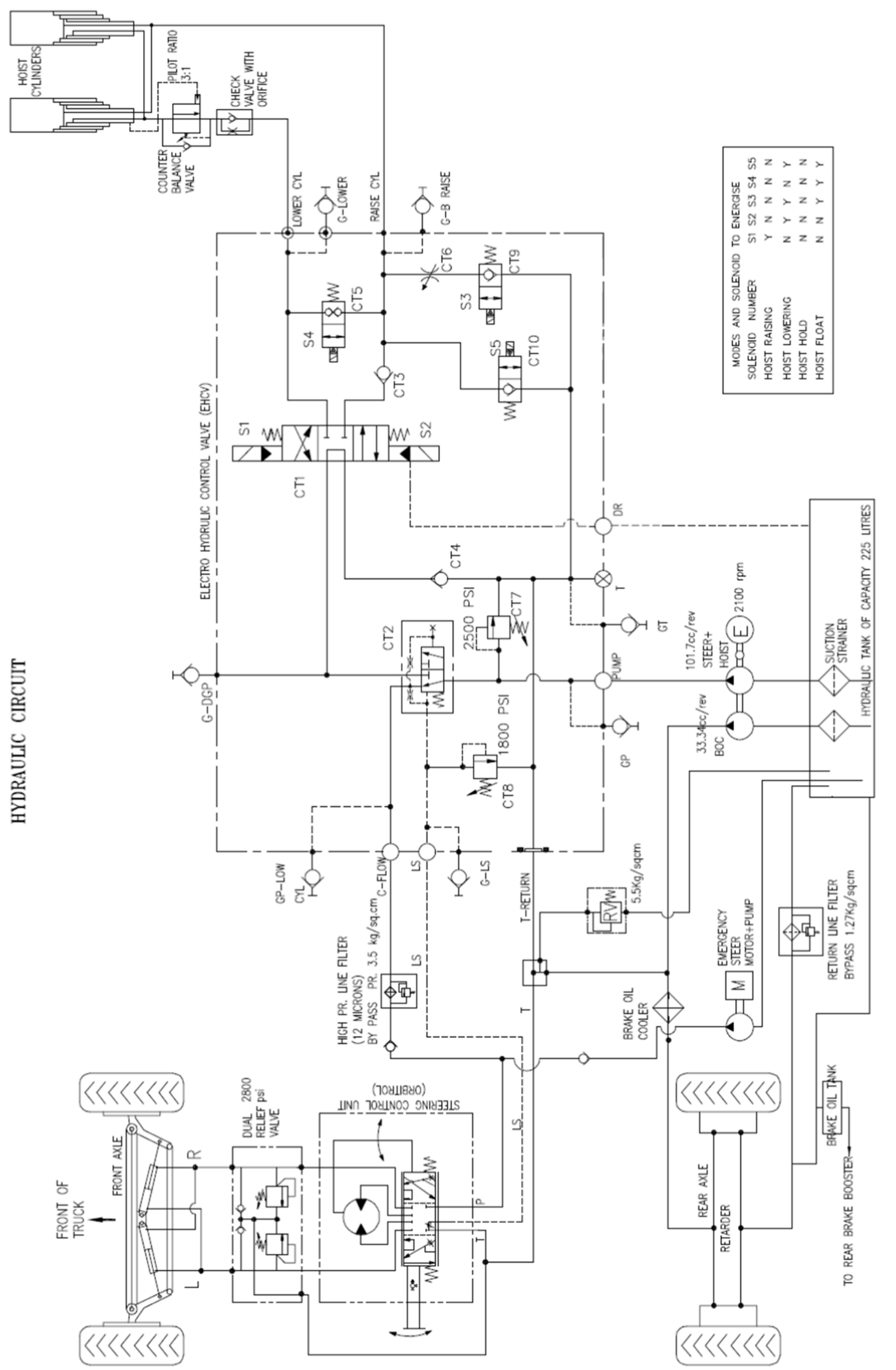

Fig. 1. Hydraulic circuit of dump truck.

Hoist System:

The hoist system is used to control the position of dump body. The hoist system consist of momentary hoist switch button (Raise, Lower/Float, Hold), Electronic Controller Unit (ECU), and Electro Hydraulic Control Valve (EHCV). The Electro Hydraulic Control Valve with five solenoid S1, S2, S3, S4 and S5 valve is used for hoist operation (Refer Table-I). During hoist operation the pressure on the load sensing line from SCU is zero. As there is no demand for steering operation, the pressurized oil is available for hoist operation. Based on the input from the operator for hoist operation priority valve in EHCV will divert the pressurized oil to hoist cylinder. When there is No load from SCU and no command from operator for hoist operation then the pressurized oil will be diverted back to tank.

Raise Operation:

When the Raise Switch is pressed by the operator the ECU will receive the signal, which will generate a command to energize S1 solenoid on EHCV for raising the body. The EHCV will divert the pressurized oil (175 bar) to hoist cylinder for dump body raise operation.

Lower Operation:

When the operator press the Lower/Float Switch, the signal will be received by ECU, which will generate a command to energize S2, S3, S5 solenoid valve on EHCV. The EHCV will divert the pressurized oil (175 bar) to hoist cylinder for dump body lower operation. The operator has to continuously press the lower button for lowering the body. During the lower operation hydraulic pump is loaded and body will come to rest position by pressurized oil within less time.

Float Operation:

When the operator press and release the Lower/Float Switch, the ECU will generate a command to energize S3, S4, S5 solenoid on EHCV which will divert the pressurized oil from hydraulic cylinder to tank to lower the body due to gravity. During float operation hydraulic oil from the pump is sent back to tank via EHCV and the pump is not loaded. The time taken by the body to come to rest position is more in float operation compare to lower operation.

Hold Operation:

When the operator press the Hold switch the ECU, will de-energize all the solenoid of EHCV and the dump body will remains in hold position.

TABLE I

Operation	S1	S2	S3	S4	S5
Raise	Y	N	N	N	N
Lower	N	Y	Y	N	Y
Float	N	N	Y	Y	Y
Hold	N	N	N	N	N

Salient Features of Control Valve:

Following are the features of cartridge type hoist control valve.

1. Solenoid operated cartridge type control valve.
2. Elimination of air system and its related components.
3. This is a custom designed valve using cartridge valve.
4. The valve is functionally identical to the existing spool type control valve.

Engineering of EHCV on dump truck

Electro Hydraulic Control valve (EHCV) was fitted on dump truck.

Following are the pressure relief settings made available on the EHCV.

Steering & Hoist line Relief Settings:

Steering & Hoist relief pressures was set to 125 bar & 175 bar respectively by pressure adjustment procedure.

Fig. 2. Hoist line relief Pressure adjustment screw.

No- Load Testing:

The dump truck was initially tested in no load condition and the steering & hoist operation is working satisfactorily. The dump body hoist & lowering time are recorded.

Body Raise time : 12 $\pm$ 2 sec

Body Lowering time : 17 $\pm$ 2 sec

Load testing:

Dump truck was loaded with mud to its rated payload of and load test was carried at the test track shown in Figure 2.

Fig. 3. Loading of Dump Truck.

Following are the data captured during load trials of dump truck fitted with EHCV and is mentioned in the graphs.

1. Steering effort(Graph.no.01)
2. Steering Pressure during lock to lock (Graph.no.02
3. Hoist pressure during body raising (Graph.no.03)
4. Temperature of the hydraulic oil Graph.no.04)

Fig. 4. Steering effort measurement.

Advantages of EHCV:

Following are the Advantages of cartridge type hoist control valve :

1. Ease of enabling safety interlocks to avoid accidents shown in Figure 05 & Figure 6.
2. Electrically operated: Elimination Pneumatic components.
3. Improved Operator Comfort: No need to hold the switches continuously for hoisting and independent of air system.
4. Easy serviceability: Individual cartridge valve can be replaced.
5. Diagnostics: Ease of diagnostics, pressure measuring ports along with minimess couplings are provided in block.
6. Manual lowering : Manual override option provided to lower the dump body in case of pump or engine failure.
7. Hoist assist ports: are provided to operate dumping/hoisting during engine or pump failure
8. Inbuilt load sense relief valve for Steering circuit.
9. Ease of introducing interlock option.

Fig. 5. Accident due to forward movement of truck with body in raised condition

Fig. 6. Accident due to Roll over of truck while dumping(Hoist operation).

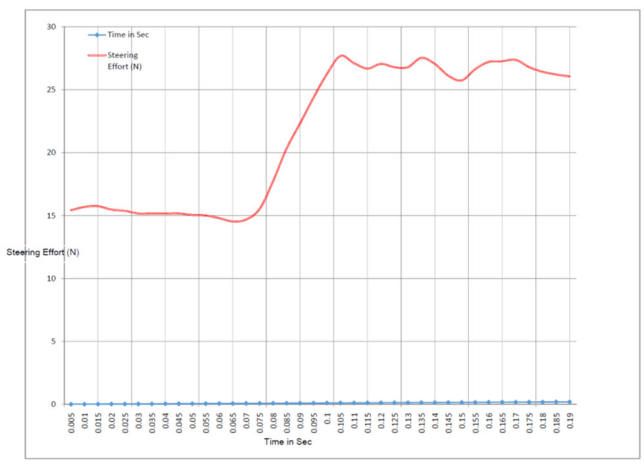

Graph 1. Steering Effort.

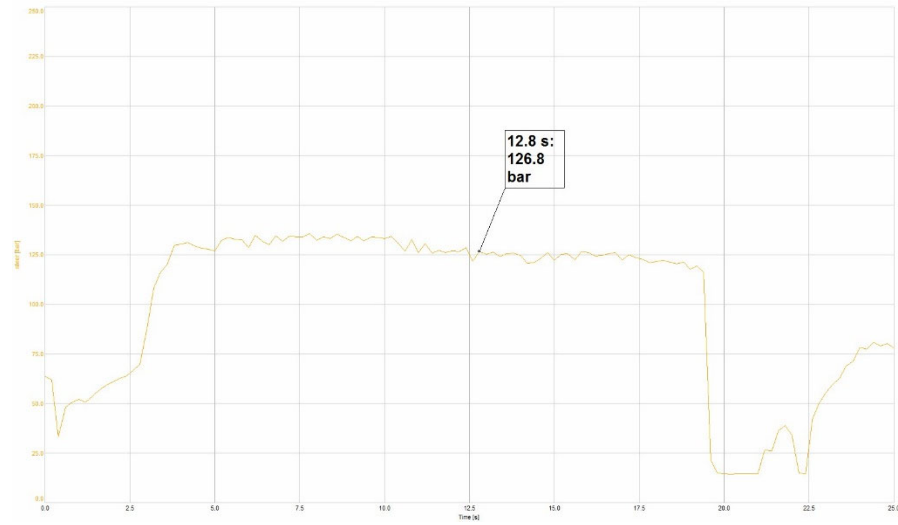

Graph 2. Steering pressure measurement during lock to lock operation.

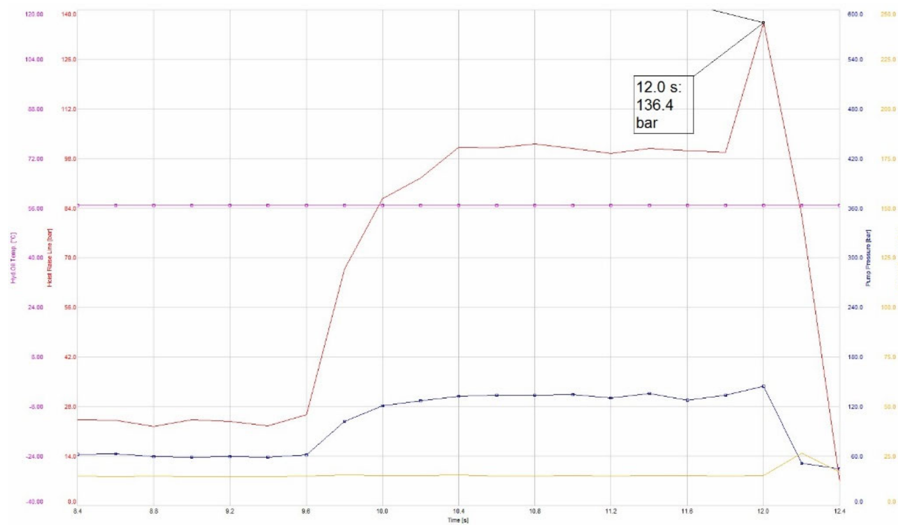

Graph 3. Hoist Pressure while dumping.

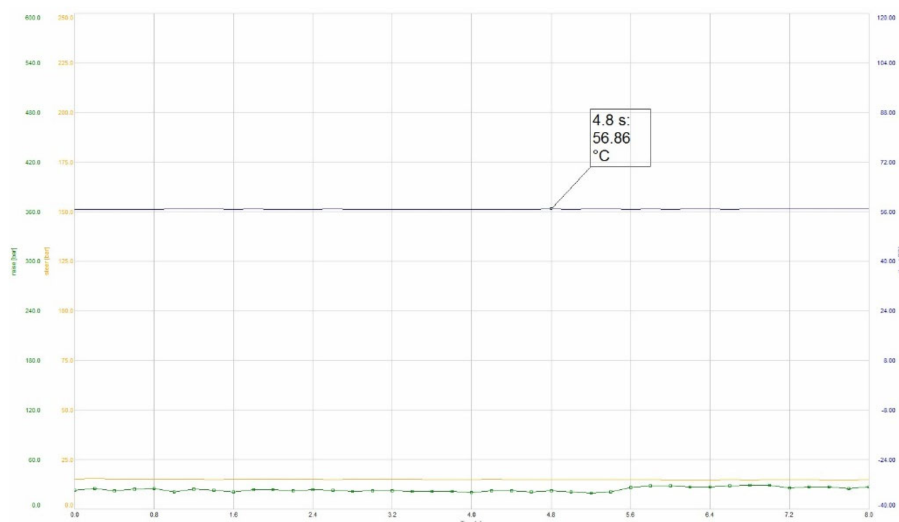

Graph 4. Hydraulic oil temperature.

TABLE 1:

Comparison of the EHCV with pneumatically operated hoist control valve -test results

Sl.No.	Parameter	Pneumatically controlled Hoist valve	Electro hydraulic control valve (EHCV)
01	Total no. of linkages to operate hoist valve	04	No linkages, only electrical wire harness
02	Waiting time to operate hoist	02 min to build pneumatic pressure to 8bar initially	No waiting time, since controlled electrically.
03	Reliability	Less reliable	More reliable
04	Body raising time	15 sec	12 sec
05	Lowering time	19 sec	17 sec
06	Hoist relief pressure	175 bar	175 bar
07	Response of hoist system	slow	fast
08	Provision for interlocks	Difficult to make interlocks	Easy for making interlocks

Conclusion

EHCV is more reliable and modular type when compared to other type of hoist control valves which are operated by pneumatic. EHCV allows to enable safety interlocks for the dump truck. Also it is easy for diagnosis of the problem in the hoist circuit. Safety interlocks will help to avoid accidents. The average steering effort measured is around 20N against the recommended maximum steering effort of 115 N as per ISO 5010

Literature Survey

The following researches deal with the on/off solenoid valves used for hoist valves.

01. Malaguti and Pregnolato.Proportional control of on/off solenoid operated hydraulic valve by nonlinear robust controller. Proceedings of the 2002 IEEE international symposium.

They investigated about continuous and proportional control of on/off solenoid driving spool directly by nonlinear control using variable structure control VSC and using solenoid model to estimate spool position. Magnetic model of solenoid and hydraulic flow forces of valve were carried out without to use FEM techniques. The spool position was estimated without a sensor by using the derivative of current method.

02.Venkatesh Babu, K.Sathish kumar. Design and fabrication of dump truck tilting system. International journal of pure and applied Mathematics volume116 no.14 2017, 327-334 ISSN(printed version):1311-8080.

Presented about the types of dump body tilting doors and their design.

References

[1] Jaroslav J. Taborek. Mechanics of vehicles. Cleveland, Penton, 1957.

[2] Barry Robinson, Guidance on Brake Testing for Rubber-tyred Vehicles Operating in Quarries, Open Cast Coal Sites and Mines. OPERC and MPQC, January 2013, Editor: Professor David J. Edwards ISBN: 978-1-906977-06-1

[3] ISO 3450 third edition 1996-04-01. Earth-moving machinery — Braking systems of rubber-tyred machines — Systems and performance requirements and test procedures. https://www.iso.org/standard/20731.html

[4] ISO 5010:2019. Earth-moving machinery — Wheeled machines — Steering requirements. https://www.iso.org/standard/68453.html

[5] Mobile Hydraulic Tips. https://www.mobilehydraulictips.com/

Address correspondence to : *Mr. Sathyarayana H. D., Assistant General Manager, Research & Development, BEML, Ltd, Mysuru, Karnataka, India*
Email: gwsatya@beml.co.in; https://www.bemlindia.in
Phone: 09972165295

ARAI Journal of Mobility Technology
Volume 2 • Issue 2 • April–June, 2022, pp. 220-227
Research Paper
https://doi.org/10.37285/ajmt.1.2.8

On Using Kriging Response Surface Method for EV Battery Pack Structural Response Prediction and Mass Optimization

Deepak Sreedhar Kanakandath, Sankha Subhra Jana and Arunkumar Ramakrishnan

Battery Durability & Fatigue, Tata Consultancy Services, Creator ITPL, Bangalore, Karnataka, India.

ABSTRACT

Structural response of battery packs in electric vehicles when subjected to road loads is an important factor that decides its performance and life during normal operation. In this paper a kriging response surface model is built using a Design of Experiment (DOE) run dataset to predict structural response and global modal frequency metrics of the battery pack. Using this Response Surface Model (RSM), we can rapidly optimize the battery pack design with respect to structural response and achieve significant mass reduction. This method reduces turnaround times for design optimization in early stages of battery pack design.

KEYWORDS: Battery pack, Random vibration response, Kriging method, MDO, Optimization, RESS, Electric Vehicle, Battery pack, Multi-disciplinary optimisation, Mass optimisation, Response surface model, Automotive, CAE, Finite element method.

Introduction

As the demand for electric vehicles rise, the need for battery packs that provide better driving range as well as enhanced performance also increases. With larger battery packs, the response of the pack to road shocks and vibrations is a key metric that is analyzed to ensure longevity of the pack and safety of the customers. This study considers the use of kriging-based Response Surface Models (RSM) to develop the capability to predict the vibration response of a battery pack, subsequently aiding in mass optimization. Kjell and Lang, 2013 [1] summarizes different battery vibration test standards applicable for Li-ion batteries. The major goals of this study are to:

- Build a response surface model of the battery pack vibration response behavior using Kriging response surface method
- Predict response, global modes, and mass of the battery pack for different component gauge variations using the RSM
- Achieve mass reduction for the battery pack using prediction functions from kriging
- Contribute to Multi-Disciplinary Optimization (MDO) activities using this prediction capability

Simulation Loads and Considerations

Battery vibration test standards

Various standards specify test procedures that emulate the effect of sustained road loads on battery modules and packs, which ultimately affect the performance and life of the Rechargeable Energy Storage System (RESS). To perform such test cases, either sine-sweep method or random vibration is used.

SAE J2380 standard for vibration testing of electric vehicle battery uses road load data measured through 100,000 miles of vehicle operation (Figure 1), which is condensed to a power density spectrum that shows the combined effect of shock loads at various G-levels. The test procedures specified in the document requires a 3-axis shaker table capable of generating accelerations up to 1.9Gs, over a frequency range of 10 to 200Hz as per SAE J2380, 2013 [2].

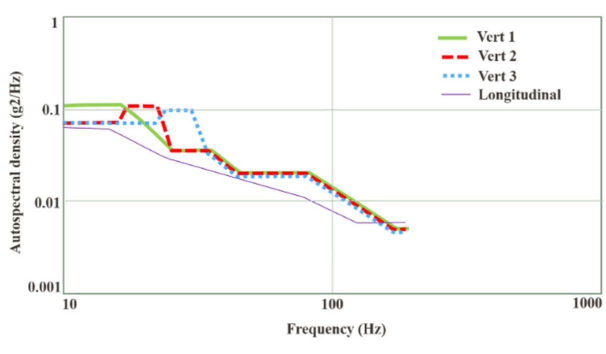

Fig. 1. SAEJ2380 random vibration spectra.

During the test, the battery is checked for loss of electrical isolation, resonance conditions, voltage fluctuations as well as thermal failure conditions. The manufacturer can include further measurements for compliance with their additional requirements. Overall, the tests ensure compliance of the battery structural and performance integrity to road-load conditions for a vibration profile up to standard response G_{rms} targets. **USABC procedure #10** specifies similar requirements for random vibration tests, with an added provision for sine-sweep. The sine-sweep excitation is applied at the vehicle resonant frequency, specified by the U.S. Advanced Battery Consortium (USABC) within the range from 10Hz to 30 Hz, as per USABC, 1996 [3]

The test standards serve as guidelines for studying the structural response of a battery pack. A battery module that is compliant with these standards would perform nominally at input vibration levels less than maximum specified in the test standard. Hence, we should ensure that the same levels feed into the mechanical hold down locations for the modules (say bolting regions), ensuring pack life and consistent battery performance over expected road load conditions.

RLDA & vRLDA road profile input

Road Load Data Acquisition (RLDA) is a method used to measure vehicle response in chosen driving environments. Hooper and Marco, 2014 [4] explains battery pack vibration measurement instrumentation and road surface classifications. The measured data is a result of monitoring important parameters that affect vehicle driving performance such as air and tire resistance and rolling speed. RLDA generates large amounts of data that is compressed into a Power Spectral Density (PSD) profile, which gives an overview of the shock load intensities over a frequency spectrum.

Schudt et al. , 2011 [5] demonstrates the Virtual Road Load Data Acquisition (vRLDA) capability that is leveraged to generate virtual road load data well ahead of any tangible hardware build. Since measured data is seldom available for Battery Electric Vehicles (BEVs), it is a common practice to use road profile data from generic cars or trucks along with vRLDA data to form a derived curve that is assumed to have close conformance with actual vehicle road load response behavior. This input profile curve is used to analyze the structural response of the pack.

Vibration response simulation in FEA

Simulation of structural response is conducted using a CAE solver with the selected PSD profile input. The Finite element (FE) model of the battery pack is solved to figure out the modal frequencies and vibration response to generate peak response results in G_{rms} at the regions where the modules are connected to the battery pack enclosure (Figure 2). The RESS to vehicle attachment points are constrained.

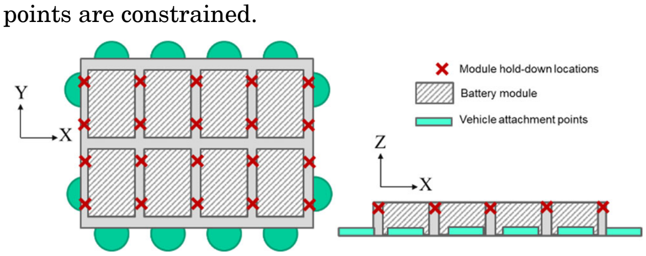

Fig. 2. Representation of the battery pack model.

Performance targets are specified based on the ability of the battery module to retain structural and operational integrity. If the G_{rms} response levels measured at the connection location (Figure 3) is greater than the target value it is tested for using any of the mentioned standards (decided based on standards and manufacturer preferences), the analysis is concluded a failure. However, in our study, the battery pack is already compliant to standard targets, and we aim at reducing mass from the structure to optimize it further.

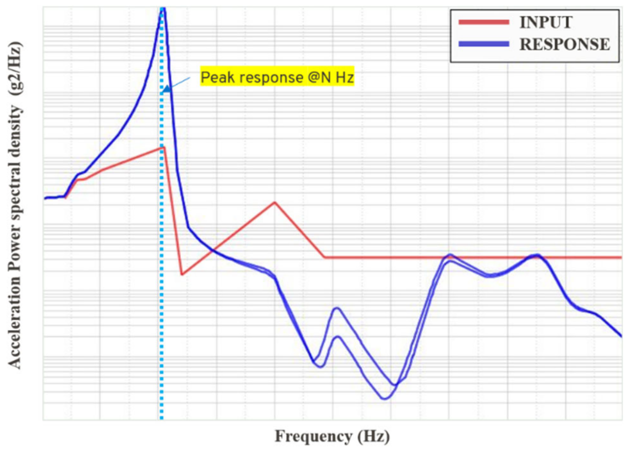

Fig. 3. Output Acc (Y) vs Frequency (x) response curve at a measured point (module hold-down location).

Besides the peak response targets, the first three global frequency modes of the battery pack are also recorded to ensure that it is sufficiently displaced from the dominant vehicle resonant frequency.

Response Surface Modelling

The main goal of this study is to predict the structural response of a battery pack instantaneously without running recurring simulations to support MDO activities. Rather than running multiple analysis to validate each optimized battery pack FE configuration, a Low Fidelity Model (LFM), otherwise known as a metamodel is created as an RSM that can predict a similar result in a less computationally intensive way, as explained by Martin and Simpson, 2004 [6]. Creating the LFM requires data samples from reality, and in our case the reality is substituted by a High-Fidelity Model (HFM) which is the Finite Element Analysis method used for response simulation. To sample data from various sites, we run a Design of Experiments (DOE) procedure, to generate multiple input FE models. To fit the metamodel, a Kriging surface method is used.

Kriging method

The Kriging method is a statistical interpolation technique, consisting of a parametric regression model and a nonparametric stochastic model. The stochastic parameters are defined using design of experiments (DOE) data obtained here by solving FE models generated according to a generated DOE matrix, explained in Zhaoyan et al., 2015 [7]. This method finds its origins in Geostatistics, pioneered by a South African mining Engineer named Danie G. Krige. Kriging was used to model underground mineral concentrations using data from just a few core drill samples.

The method can accomplish response prediction at any point, as well as assess the local uncertainty called Kriging variance on the response. Magnitude of variance determines certainty of the prediction.

In traditional multi-order regression fits, the form of the curve is assumed early before the fitting is done. Kriging considers outputs of a system as a random process and is comprised of two parts: A linear regression component that projects the general trend of the data, and a probabilistic component that estimates the deviation from measured data. [[7]].

[[7]] $\hat{y}(x) = \boldsymbol{f}^T(x)\boldsymbol{\beta} + Z(x)$

The stochastic component in kriging, denoted by Z(x), assumes that the errors in predicted values at interpolation locations must always be a Gaussian distribution (Figure 4). Discussion regarding selection of kriging form (choice of Spatial correlation function (SCF)) and using univariate SCF for each input dimension is explained in [[7]].

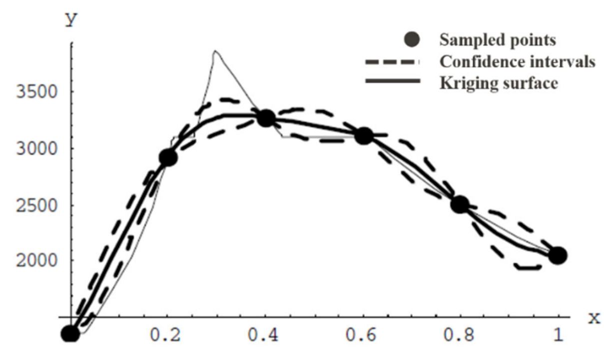

Fig. 4. Example of a kriging model. Dotted lines indicate confidence intervals.

Various research material is available for application of Kriging methodology in CAE optimization in finite element models. Dong et. al, 2019 [9] demonstrates the use of Kriging based optimization in the design of the hull-structure of an autonomous underwater vehicle. Finite element models are run to find the maximum von-mises stress, buckling load of the shell structure, and the sample values are used to build the response surface model. Kachinowski and Fu, 2005 [8] shares information about a Kriging-based error reduction approach used in vehicle occupant restraint system design, in vehicle structure CAE. In this study, we generate and solve multiple DOE models from a baseline battery pack model to create an output dataset. The kriging method is used to fit RSMs, which are then cross validated with the same input dataset using a "leave-one-out" method. The RSM is then used to predict vibration response for a given configuration of the pack built using controlled component gauges, and possibility of mass optimization is investigated.

Input parameters for DOE

A host of input parameters may be chosen to tune with in the battery pack model, such as component gauges, material, parametrized component features etc. These parameters will essentially function as the "knobs" to control for the user to optimize the model once the RSM is generated. In earlier phases of the pack design, the component designs are comparatively crude, and thus simple gauge reduction or material changes are enough to enable optimization studies. Here the input parameters are set as component gauge variations.

The components are grouped into nine different blocks based on baseline gauge values and/or depending on how they are attached to the structure (Figure 5). Gauge blankets are selected based on how much control we require in the system during prediction. All components within a gauge blanket are set to the selected gauge in each DOE model.

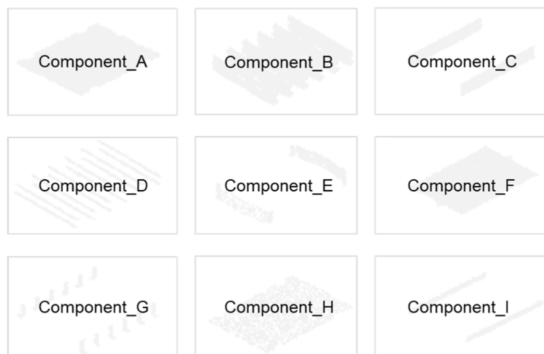

Fig. 5. Blanket gauge groups for components.

DOE matrix

Selection of input variable bounds: The DOE matrix is generated based on user-specified levels of gauges (Table 1), considering the gauge variables as discrete. This would ensure that generated gauges in DOE models do not have unrealistic values that have practical implications in manufacturing. Also, it should be noted that any change in gauge would apply to all components within the group, and it is not possible to vary gauges for specific components in a group once they are assigned to a design variable input. Assigned gauge levels for each variable are shown in table 1.

TABLE 1

DOE input parameters and discrete gauge value levels

Gauge_blanket	Code	Type	Levels (mm)
Component_A	P1	Q	1/1.2/1.4/1.5/1.6/1.7
Component_B	P2	Q	0.7/0.8/0.9/1/1.1/1.2
Component_C	P3	Q	0.7/0.8/0.9/1/1.1/1.2
Component_D	P4	Q	0.7/0.9/1.1/1.2/1.3/1.4
Component_E	P5	Q	1.8/1.9/2/2.1/2.2
Component_F	P6	Q	1/1.1/1.2/1.3/1.4
Component_G	P7	Q	0.8/0.9/1/1.1/1.2
Component_H	P8	Q	1/1.2/1.4/1.5/1.6/1.7
Component_I	P9	Q	1.5/1.7/1.9/2/2.1/2.2

Experiment design method: A Strength-Two Orthogonal array design is used to generate the DOE matrix, with the above shown nine input variables. The key feature of this method is that it produces a set of samples that yield uniform sampling in any *t*-dimensional projection of an *n*-dimensional design space where (t<n) as explained by Giunta et al., 2003 [10]. Orthogonal array sampling produces a design sample subset from a library of stored array samples, and a pre-defined number of DOE points are output for use. An example for a 2-strength OA in a 3-dimensional design space is shown in figure 6.

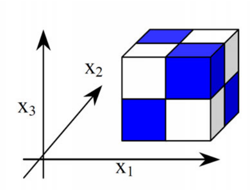

Fig. 6. Each of the shaded bins contain one sample. The figure represents a 3-dimensional, 2 strength OA [10]

In this scenario with 9 input variables, 64 DOE points are selected as optimum, below which the correlation value with the full array starts to deteriorate. An example of the generated DOE matrix is shown in table 2.

TABLE 2

DOE points in the generated matrix (all gauges in mm)

Point	Comp A	Comp B	Comp C	Comp D	Comp E	Comp F	Comp G	Comp H	Comp I
1	1	1.2	0.8	1.1	2.2	1	1.2	1	2
2	1.7	0.7	0.8	1.4	1.8	1.3	0.8	1.6	1.7
.	.	.	.	..	.	.	.	.	.
64	1.4	0.9	0.8	1.2	1.9	1.2	0.9	1.4	1.9

Size of the dataset does have an impact on the quality of surface fits, but too many input design variables would require a very large number of DOE runs that will consume excessive computing resources and time. For this problem, 64 DOE models are generated. These 64 models, along with the baseline model are used to generate the RSM.

Generating FE models using the doe matrix

The CAE preprocessing software Hypermesh™ was used to generate the DOE models in the selected solver format. From the baseline model, the property "PSHELL" cards (Figure 7) are isolated, and the gauge values are fed as a spreadsheet file to a tcl/tk script. This generates and exports all required DOE models to a directory of choice. The files are submitted as batch to an HPC cluster to solve.

```
$HMNAME PROP
1081"XXXXXXXX_001_XXXX_XXXX_FRT_UPR_LH_aa_00mm" 4
$HWCOLOR PROP                1081      11
PSHELL      108111909510 0.7     11909510        11909510        0.0
$HMNAME PROP
1083" XXXXXXXX_001_XXXX_XXXX _Bkt_FRT_UPR_bb_00mm" 4
$HWCOLOR PROP                1083      11
PSHELL      108310304210 1.2     10304210        10304210        0.0
```

Fig. 7. PSHELL property generated by script for DOE models

Doe results

The out and .pch files after solver modal and response runs are parsed to extract relevant output information to build the RSM model. Python and tcl scripts enable file parsing and result extraction. Global modes are extracted based on effective mass fraction participating in a frequency mode. A certain threshold value of 20%-30% is decided, according to which global modes are extracted from the result file (Figure 8). Generally, frequency modes having less than 20% mass participation would be local modes having no real effect on the battery pack.

#	Freq	Xt	Yt	Zt	Xr	Yr	Zr
2	58.79	3.7E-05	2.4E-06	0.7653	2.5E-05	0.731	2.7E-06
4	64.45	0.00044	0.02978	2.7E-05	0.4918	0.00022	0.02831
10	72.48	0.5248	0.00067	0.00118	5.24E-07	0.00552	0.00066
53	115.4	5.23E-08	0.4953	1.2E-05	0.2229	8.9E-06	0.3907

Fig. 8. Extracted global modes for a DOE point. Effective mass fractions in each DOF are shown.

Similarly, the peak response value in G_{rms} is also extracted in X (fore-aft), Y (lateral) and Z (vertical) directions, along with the corresponding frequencies. (Figure 9). The mass of each DOE model is directly computed from Hypermesh™ at the time when all the DOE models are initially generated.

DOE #	Max X	Max Y	Max Z	Freq X	Freq Y	Freq Z
1	1.8	0.78	0.91	76	114	67
2	1.78	0.83	1	75	111	62
3	1.87	0.79	0.87	74	112	65
4	1.79	0.77	0.84	76	114	68
5	1.86	0.79	0.92	74	111	64
6	1.8	0.81	1	75	112	63
7	1.77	0.78	1.03	74	113	62

Fig. 9. Extracted response results and corresponding frequencies for the first seven DOE points

RSM Generation and Cross Validation

To generate a kriging surface, all design variables (gauge buckets 1-9) and result outputs (10 outputs) are used. A general structure of the RSM is summarized in figure 10.

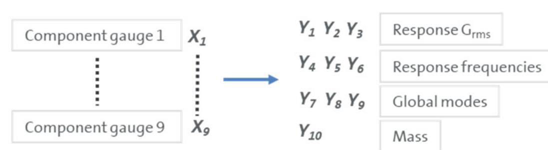

Fig. 10. General structure of the RSM used for prediction

The RSM is cross validated using the "leave-one-out" method. Here, the actual value of each point in the DOE space is predicted using a surface comprising of all other points in the space. An ideal case would have all points in the Predicted vs Actual value plots group around the 45-degree line (Figure 11). In this case, the plot for output variable "Freq Y" shows most dispersion, but we may ignore it because our battery pack model shows comparatively mild response conditions in the lateral vehicle direction.

The error vs point number plot (Figure 12) shows the error in prediction for all the 65 DOE points we have selected to generate the RSM. Outlier data points can easily be identified from this plot. Similarly, error plots for all outputs are analyzed.

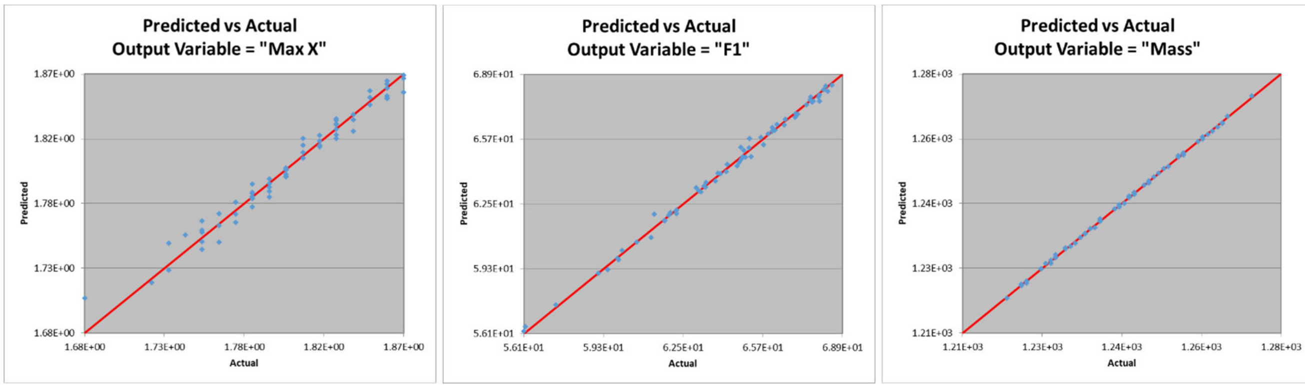

Fig. 11. Predicted vs Actual value plots using "leave-one-out" cross validation technique for Max X response, First modal frequency, and Mass.

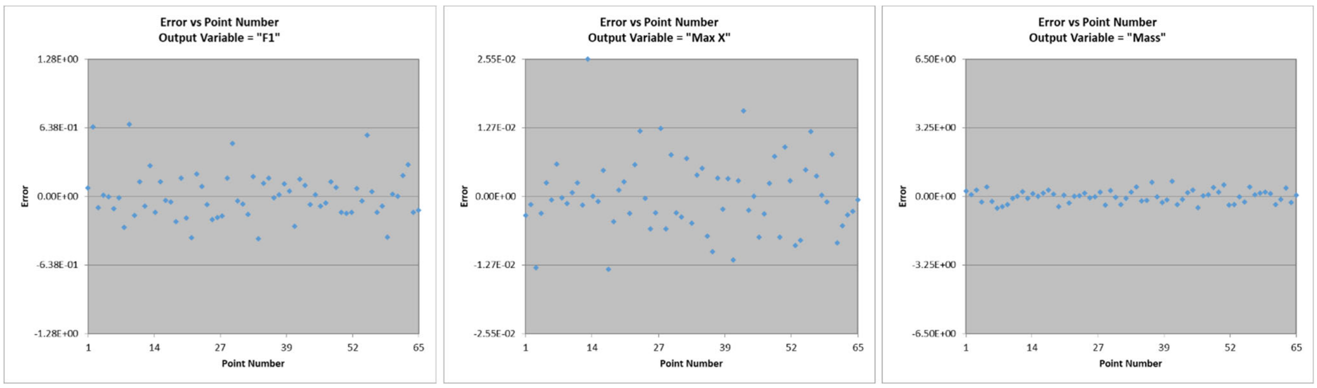

Fig. 12. Error vs Point number (DOE) plot for Max X response, First modal frequency, and Mass.

The mean squared errors (Table 3), calculated from variance of output from the regression fit as in Kachnowski, B et al. [[7]], calculated as a fraction of output range are shown below:

TABLE 3

Mean squared errors for outputs after cross validation

Output param	Param-code	Mean squared error as a fraction of Y range (%)
Global mode 1 (Hz)	F1	1.70
Global mode 2 (Hz)	F2	8.08
Global mode 3 (Hz)	F3	6.02
Peak response in X (G_{rms})	Max X	3.68
Peak response in Y (G_{rms})	Max Y	5.56
Peak response in Z (G_{rms})	Max Z	1.98
Peak X resp. Frequency (Hz)	Freq X	5.83
Peak Y resp. Frequency (Hz)	Freq Y	9.99
Peak Z resp. Frequency (Hz)	Freq Z	2.68
Mass of battery pack	Mass	0.46

Analysis of variance (ANOVA)

The analysis of variance studies the influence of inputs parameters on the outputs. By performing ANOVA, we can figure out the percentage contributions of each input parameter for the DOE and effectively tune the model for further optimization.

The design variables P1, P7 and P8 show significant contributions in peak response and first global frequency mode outputs (Figure 13). This knowledge can be used to refine and/or eliminate the design variable inputs in further studies. Convergence analysis gradually adds data points as the model is checked for percent contributions, finally reaching a point where no further addition of points show increase or decrease in percent contributions in an input parameter. This also helps to validate the DOE space size that is used to build the RSM. The convergence chart for one of the output parameters (Max X – Peak response in the X direction) is shown in Figure 14.

When multiple input parameters have an interaction with each other, the effect on changing one parameter on the output differs with the value of the other (Figure 15). Whenever this value is more than 5%, it is plotted as an interaction plot that plots main effect of both parameters when the other is kept constant at its lower or upper bounds. The main effect plot (Figure 16) illustrates the nature of variation of the output when the input parameters are varied from 0% (the lower bound) to 100% (the upper bound). Here, parameter P2 is found to have no effect until it approaches the upper bound value. Except parameters P1, P7 and P8 others are found to have no real significance in predicting value of "Max X". Although these inferences may not reflect in real life design choices, it can be used to streamline the RSM in future iterations.

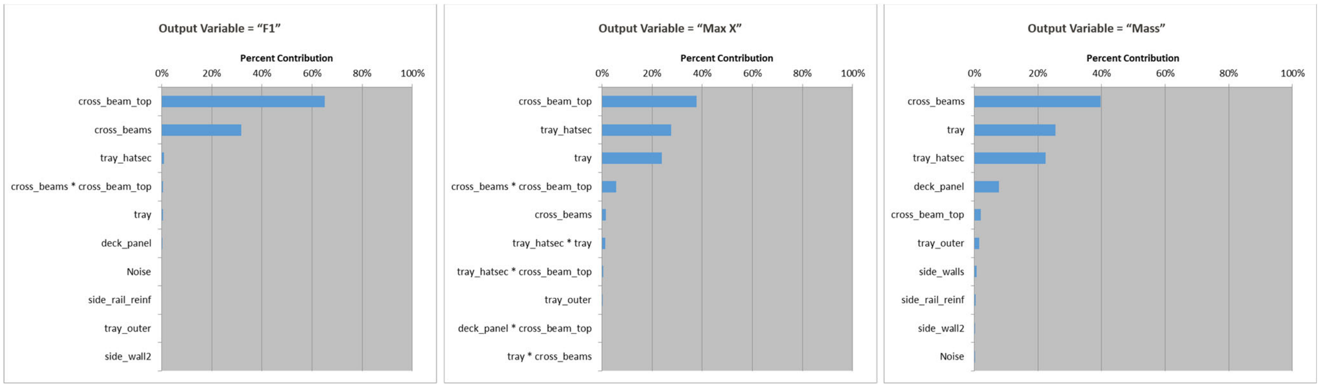

Fig. 13. ANOVA percent contributions for input variables P1-P9 and their interactions, for Max X response, First modal frequency, and Mass

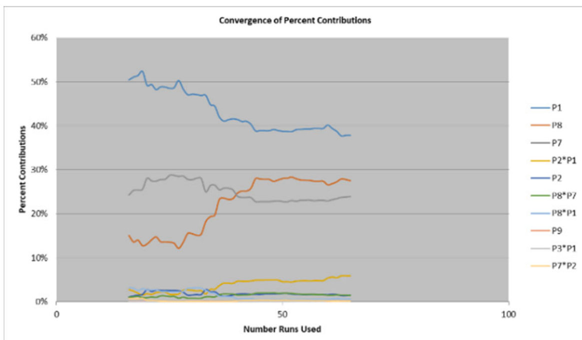

Fig. 14. Convergence of percent contributions for output "Max X".

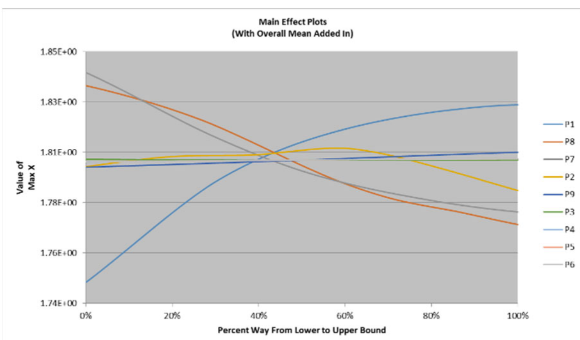

Fig. 15 Main effect plots for all inputs P1-P2 for output Max response X.

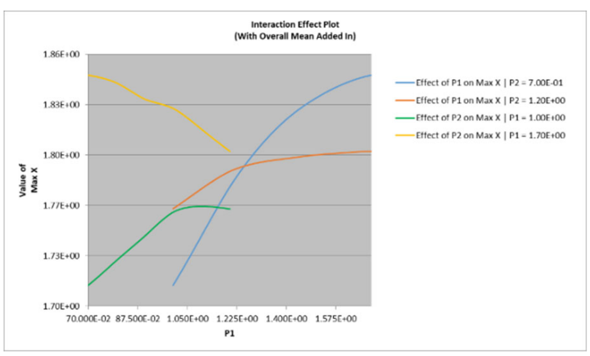

Fig. 16. Plot showing interaction between P1 and P2.

Here, increasing gauge of parameter "P2" when "P1" value is kept at its lower bound tends to increase the peak X-response value of the pack, and vice versa when kept at the upper bound. Similarly, it is ideal to analyze all variable interactions for all outputs to gain valuable insight into the RSM characteristics.

RSM Correlation and Mass Optimization

The Response surface model generated using Kriging method enables export of prediction functions, to a specified confidence level (95%). Prediction functions are generated and exported for each of the ten output/Reponses. Using these functions, a dashboard is generated in excel (Figure 17) where for any user-input value of DVs (Design variables – gauges), all required responses can be predicted instantly. However, as the gauge bounds depart the bounds used for building the RSM (the DOE bounds), the prediction results tend to deviate.

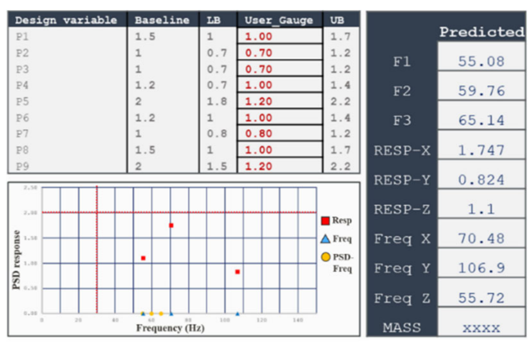

Fig. 17. Excel dashboard for response and modal prediction for the battery pack (Sample shown).

Correlation of predicted results are checked by solving FE models with the thickness gauge values used for prediction and comparing the results. Two such sets of gauges are shown in the table below and were selected by were selected on a consensus from relevant stakeholders (Table 4). The difference in results between predicted and FEA outputs are found to match closely, as the cross-validation results also suggested (Table 5).

TABLE 4

Proposed gauge combinations for correlation models

Gauge_blanket (mm)	Design proposal 1	Design proposal 2
Component_A	1.00	1.00
Component_B	1.10	0.60
Component_C	0.80	0.60
Component_D	1.20	1.20
Component_E	1.20	1.80
Component_F	1.20	1.00
Component_G	0.90	0.80
Component_H	1.00	1.00
Component_I	1.20	1.20

TABLE 5

Correlation result data that to show RSM reliability (Mb is mass of the baseline model battery pack)

Outputs	Proposed gauges #1		Proposed gauges #2	
	Prediction	Actual	Prediction	Actual
F1 (Hz)	54.36	55.1	55.8	55.8
F2 (Hz)	59.19	59.9	62.62	61.8
F3 (Hz)	63.26	69.7	74.8	71.8
Max X (G_{rms})	1.7	1.76	1.72	1.7
Max Y (G_{rms})	0.817	0.95	0.81	0.83
Max Z (G_{rms})	1.142	1.02	1.09	1.1
Freq X (Hz)	70.28	69	71.8	72
Freq Y (Hz)	109.1	105	111.5	108
Freq Z (Hz)	54.75	55	55.36	56
Mass (Kg)	M_b-35	M_b-35	M_b-76	M_b-77

A detailed optimization set up may be performed using an established multi-objective optimization technique like the Pareto front, that can quickly generate a set of feasible solutions. This is however a future scope for the study, and mass optimization here is performed through a simple excel data solver that uses outputs from the Kriging RSM predict functions to generate optimum gauge values. The range of optimization may be controlled by varying the thickness bounds (Table 6), provided they do not deviate too much from the DOE bounds.

TABLE 6

Constraints and objectives used for Mass optimization of the battery pack

Parameter	Type	Objective	Target	Lower bound	Upper bound
Gauge1-9	Input			Yes	Yes
Modal Frequency 1-3	Output	-	Vehicle modal Target	-	-
Response X/Y/Z	Output	-	Target Grms for battery module integrity	-	-
Peak response Frequencies X/Y/Z	Output	-	-	-	-
Mass	Output	Minimize	-	-	-

The optimal design obtained within DOE bounds was up to 36kg lesser than the baseline battery pack mass. This mass reduction is a significant result since we can maintain pack modal and road response performances. This prediction interface can now be used in MDO operations as a quick check for estimating modal and response behavior of the battery pack. MDO also involves stakeholders from other CAE disciplines like safety and crash.

Conclusion

The study conducted here reinforces the use of a metamodel approach using kriging RSM in the design optimization of a battery pack. Since the pack already meets target response requirements, an opportunity is presented for mass reduction using prediction functions of the RSM model. Careful selection of Input design variables that can effectively influence the behavior of the pack are crucial when building the RSM. After generation of the RSM, it is cross validated to ensure model credibility, as well as analysis of variance (ANOVA) is performed to determine if any further streamlining is required while selecting input variables. Multiple gauge proposals were made, and the predicted values were correlated with analysis runs. With the validated RSM, we can quickly predict peak vibration response, global frequency modes as well as mass of the battery pack for ideally all gauge variations of the input parameters. This greatly reduces turnaround time in MDO activities, where validation with respect to modal frequencies and vibration response of the pack are available instantly. This method may be used in the initial stages of the battery pack design when there is maximum room for improvement.

References

[1] G. Kjell and J. F. Lang, "Comparing different vibration tests proposed for li-ion batteries with vibration measurement in an electric vehicle," 2013 World Electric Vehicle Symposium and Exhibition (EVS27), Barcelona, 2013, pp. 1-11.doi:10.1109/EVS.2013.6914869 http://ieeexplore.ieee.org/stamp/stamp.jsp?tp=&arnumber=6914869&isnumber=6914705

[2] Surface vehicle recommended practice, "SAE standard J2380 - Vibration testing of Electric Vehicle Batteries", issued 1998-01, revised 2013-12, Superseding J2380 MAR2009 https://saemobilus.sae.org/content/J2380_201312/

[3] USABC Electric Vehicle Battery Test Procedures Manual, Revision 2, January 1996. Report No.DOE/ID-10479, Rev. 2. http://avt.inl.gov/energy_storage_lib.shtml

[4] Hooper, James & Marco, James. (2014). Characterizing the in-vehicle vibration inputs to the high voltage battery of an electric vehicle. Journal of Power Sources. 245. 510-519. http://dx.doi.org/10.1016/j.jpowsour.2013.06.150

[5] Schudt, J., Kodali, R., Shah, M., and Babiak, G., "Virtual Road Load Data Acquisition in Practice

at General Motors," SAE Technical Paper 2011-01-0025, 2011, https://doi.org/10.4271/2011-01-0025.

[6] Martin, J. and Simpson, T., "On Using Kriging Models as Probabilistic Models in Design," SAE Technical Paper 2004-01-0430, 2004, https://doi.org/10.4271/2004-01-0430.

[7] Zhaoyan Lv, Zhenzhou Lu, Pan Wang, A new learning function for Kriging and its applications to solve reliability problems in engineering, Computers & Mathematics with Applications, Volume 70, Issue 5, 2015, Pages 1182-1197, ISSN 0898-1221, https://doi.org/10.1016/j.camwa.2015.07.004

[8] Kachnowski, B. and Fu, Y., "Experience with Response Surface Methods for Occupant Restraint System Design," SAE Technical Paper 2005-01-1306, 2005, https://doi.org/10.4271/2005-01-1306

[9] Dong H, Song B, Wang P. Kriging-based optimization design for a new style shell with black box constraints. Journal of Algorithms & Computational Technology. September 2017:234-245. doi:10.1177/1748301817709601

[10] Giunta, A. & Wojtkiewicz, Steven & Eldred, Michael. (2003). Overview of modern design of experiments methods for computational simulations. AIAA. 0649. 10.2514/6.2003-649. https://arc.aiaa.org/doi/10.2514/6.2003-649

Address correspondence to *Mr. Deepak Sreedhar Kanakandath, Senior CAE Engineer, Battery Durability & Fatigue, Tata Consultancy Services, Creator ITPL, Bangalore, Karnataka, India*
Email: deepaksreedhar.k@tcs.com
Phone: 08867016122

ARAI Journal of Mobility Technology
Volume 2 • Issue 2 • April–June, 2022, pp. 228-232
Research Paper
https://doi.org/10.37285/ajmt.1.2.9

Comparison of Numerical Methods for Thermal Performance Evaluation of Circuit Protection Devices in EV Application

Avadhoot Kittur[1], Dikhsita Choudhary[1] and Robert Michael Slepian[2]

[1]*Modelling and Simulation CoE, Eaton Technologies, Survey No. 77, Plot No. 1, Cluster C, Wing 1, EON Free Zone, Kharadi, Pune – Maharashtra.*

[2]*Eaton Corporation, Bloomfield, New Jersey, United States.*

ABSTRACT

With the growing demand of electric vehicles, design of circuit protection devices is now an important consideration in automobile industry. Modern day circuit protection devices have been constantly undergoing miniaturization due to requirement of minimizing the foot print for use in electrical vehicles and aerospace applications. This size reduction makes thermal management one of the most important aspects of their design. Use of numerical model to predict heat transfer can significantly reduce the cost and time required in testing physical prototypes.

In this paper, three different approaches for numerically predicting temperature rise of circuit breakers are discussed and compared from the point of view of accuracy and computational effort. The three methods are 1) Finite volume based analysis in which conjugate heat transfer inside and outside the breaker is modelled by solving Navier-Stokes equations 2) Finite element based heat conduction model in which convection is modelled as boundary condition instead of solving for fluid motion, and 3) Thermal network based model which uses electrical analogy of heat transfer to solve a thermal resistance network.

In the first two iterative models mentioned above, heat generation from current-carrying parts is calculated by solving Maxwell's equations of electromagnetics by Finite element method. Eddy current losses and temperature dependence of electrical conductivity is considered in the calculation of heat loss. In all three methods, electrical and thermal contact resistances are added at appropriate locations based on analytical calculations. All three methods have been validated with temperature rise test results.

In this paper, the heat loss and temperature of a molded case circuit breaker have been predicted by all three methods discussed above. It is observed that the Finite volume-based method is the most accurate amongst the three methods. It can computationally predict air motion and air temperature at critical locations. However, this additional accuracy comes at the cost of added effort in terms of additional mesh count and computation. The Finite element-based method gives good accuracy but does not predict air temperature. The analytical network-based model is less accurate compared to other methods and relies on product expertise and experience.

Based on the study, the following recommendations are made: 1) The finite element-based method is best suited to evaluate designs which do not alter flow pattern significantly 2) The finite volume method is recommended to evaluate effect of flow altering design changes 3) The network-based model is recommended for initial evaluation of correct cross sections of current carrying members.

KEYWORDS: Thermal management, Computational Fluid Dynamic, Thermal Network Analysis, Contact resistance, electrical contacts

Introduction

In present-day world, circuit protection devices form an integral part of all electrical systems including electric vehicles. From single-wire fuses to large switchgears, circuit protection devices find their way into every electrical installation, isolating the circuits from overcurrent conditions due to short circuit or overload.

Power loss from current carrying devices is converted into heat. Hence, they are required to satisfy strict temperature rise requirements by certificating bodies like IEC and UL. As technology is progressing, one of the major development areas of these devices is reduction of material hence increasing their ampacity. To satisfy the temperature regulations, the designs of these current carrying parts need to be optimized.

Experimental setups for every design iteration being a costly affair, numerical and analytical models are widely adopted nowadays to predict temperature rise. Lot of research has gone into building numerical models for heat load and temperature prediction.

For DC applications heat loss from conductors can be calculated as a multiplication of electrical resistance and squared current value. For AC applications, due to electromagnetic effects, there is an additional heat generation. For such cases, a set of electromagnetic equations need to be solved for calculating heat loss. Resistance offered to current is a direct function of the temperature rise in the components hence electromagnetic and thermal model needs to be coupled.

Temperature rise due to this heat generated is predicted by numerous methodologies in literature. In one approach, FEM is used to solve steady-state heat transfer equation to predict temperature rise. In such methods, dissipation of heat due to convection is approximated by assuming values of heat transfer coefficient. Weichart and Steinhauser [1] have used an FEM based tool to evaluate temperature on current conducting parts on a low voltage switchgear. Frei and Weichart [2] later used similar model in their work to predict temperature on non-current conducting parts like plastic casing in addition to current carrying parts. FVM is used solve all the conservation equations of mass, momentum and energy to predict temperature. In such analysis, a detailed study of air motion around the current carrying parts is possible. Heat transfer by convection is predicted accurately, unlike FEA based method. Bedkowski et al. [3] in their work shows a good validation of temperature rise prediction in a low voltage switchgear by a coupled electromagnetic- FVM model with experimental results. Xiao Yu, Fan Yang, Gao Bing *et al.* [5] have used coupled electromagnetic and thermal analysis to predict hot spot in vacuum bottle of vacuum circuit breaker. They observed that contact resistance between current carrying components can have significant effect on temperature rise. Accurate estimation of contact resistance thus, becomes necessary.

Molitor, F., Shoory, A., Sologubenko, O., Kaufmann, P. et al. [6] performed FEA based simulations to predict hotspots in busplates and contacts. They discuss the importance of capturing skin and proximity effect for accurate estimation of current distribution and hence ohmic losses.

The two methods discussed above, although helps in cost saving, require additional time in preparing the numerical models of each design iteration. Many researchers have used analytical models involving thermal network theory to approximate temperatures. Such models are based on the analogy between thermal and electrical resistances. Cherukuri [4] in his work has elaborately described how such a model can be employed to predict temperature rise in the design phase.

Literature has all three of the methods employed extensively in predicting temperature on circuit protection devices. There is very limited work wherein comparison of results predicted by all three methodologies has been made. The present work takes the case of a molded case circuit breaker and studies temperature prediction using all three methodologies described above. Results predicted are compared with actual experimental test results. The advantages and disadvantages of using each model are discussed.

Numerical Methods

Numerical analysis of circuit protection devices involves solving two different physical phenomena. Maxwell's equations for electromagnetics are solved for calculating heat generation due to electromagnetic effects in FEM based tool. The temperature rise due to this heat generated is calculated by solving (a) Steady-state heat transfer equation, in the FEM based approach, (b) equations of momentum, continuity, energy, turbulence and radiation in the FVM based approach. The network-theory based approach calculates analytically the Joule heat and heat due to eddy currents and predicts the temperature rise considering all three modes of heat transfer, viz. conduction, convection and radiation in the form of resistances.

Finite volume method based approach

Geometry and mesh: The circuit protection device used for the study is a Molded Case Circuit breaker (MCCB) which is a low voltage device. Fig. **1** shows the current carrying parts of the breaker.

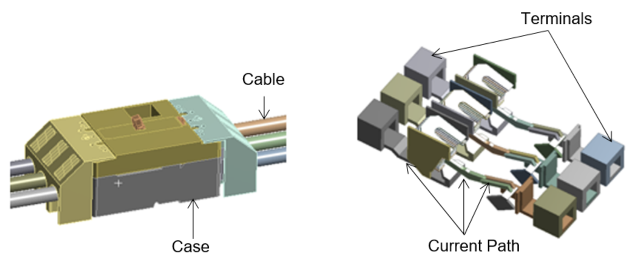

Fig. 1. MCCB Geometry.

The electromagnetic model used to predict heat generation in both the iterative approaches, was developed in ANSYS Maxwell tool. The mesh generation in this tool was carried out by adaptive discretization algorithm which utilizes the principle of energy conservation.

For Finite Volume Method, an air domain around the MCCB was modeled. Use of hexahedral cells for the CFD model ensured better accuracy and a reduced mesh size. Prism cells with higher aspect ratio were used in the fluid volume near solid walls to accurately capture boundary layer phenomena. The effect of change of density due to change in air temperature is captured by ideal gas equation.

Governing equations: For all types of flows involving heat transfer, ANSYS Fluent solves conservation equations for mass, momentum and energy. The steady-state conservation equations for mass, momentum and energy are:

$$\nabla.(\rho \boldsymbol{v}) = S_m \quad \ldots(1)$$

$$\nabla.(\rho \boldsymbol{v}\boldsymbol{v}) = -\nabla p + \nabla.(\bar{\bar{\tau}}) + \rho g + F \quad \ldots(2)$$

$$\nabla.\left(\boldsymbol{v}(\rho E + p)\right) = \nabla.\left(k_{eff}\nabla T\right) + S_h \quad \ldots(3)$$

$$E = h - \frac{p}{\rho} + \frac{v^2}{2} \qquad \ldots(4)$$

$$h = \sum_j h_j Y_j \qquad \ldots(5)$$

$$h_j = \int_{T_{ref}}^{T} c_{p,j} dT \qquad \ldots(6)$$

where,

p is the static pressure

$\bar{\bar{\tau}}$ is the stress tensor

ρg is the gravitational body force

F is the external body force

k_{eff} is the effective conductivity

S_h is the volumetric heat generation due to current flow through the conductors.

Table 1 below shows the values of k_{eff} and for materials used in simulation.

TABLE 1

Values of $\boldsymbol{k_{eff}}$ for materials used in simulation

Parameter	Value
k_{eff}	390 W/mK (for copper) 0.3 W/mK (for plastics)

Values of other parameters are computed by the simulation model at various nodes.

The source term S_h in the energy equation is obtained by solving Maxwell's equations in the FEM based solver ANSYS Maxwell. The solver considers skin and proximity effects due to eddy currents set up due to electromagnetic induction.

To capture air flow around intricate shaped bodies inside the circuit breaker, k-ε turbulence model is chosen.

Radiation of heat inside the breaker is captured by the surface-to-surface model which assumes that all walls of the breaker are diffuse.

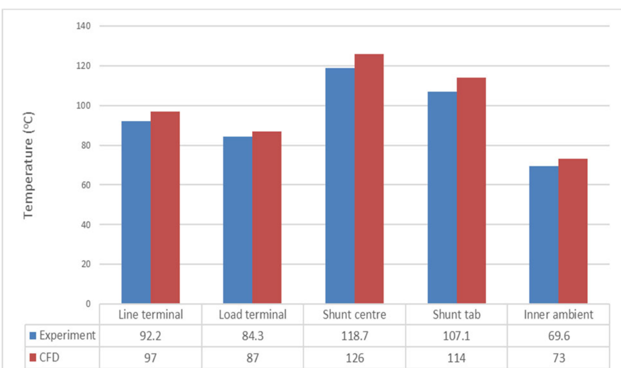

Fig. 2 Comparison of temperature predicted by FVM method with experiment.

Fig. 2 shows comparison of temperature predicted by FVM with experiment. This methodology predicts temperatures quite accurately on the current path with a maximum deviation of 80C. Also, fluid temperatures can be accurately predicted as air flow is solved by solving Navier Stokes equations numerically. Fig. 3 shows air velocity vectors colored by temperature on the air domain surrounding the current path. This output can be useful to predict air temperature near the electronic components inside the switchgear. This methodology is best recommended when internal convection has a significant contribution in overall heat dissipation. Problems involving thermal performance evaluation of heat sinks, flow through vents/ louvres, forced convection by fans, blowers etc. can be best studied using this methodology.

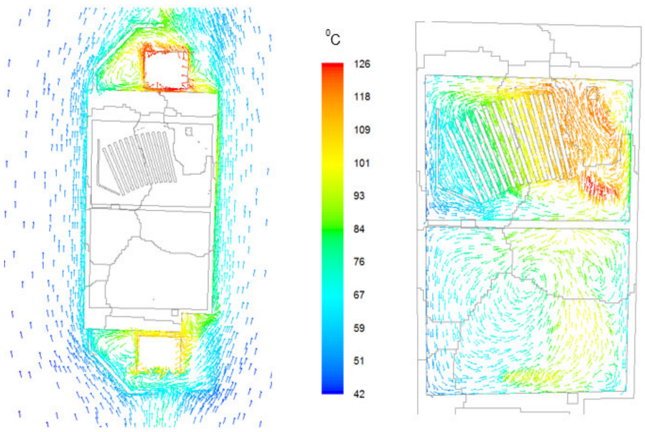

Fig. 3. Velocity vectors colored by temperature inside and outside the MCB

Finite element-based Methodology

Products like MCCBs, MCBs usually have small internal air cavities and no vents for air circulations. Natural convection and radiation from external casing surfaces and cables are the major modes of heat dissipation in these products. If simulation objective is to optimize the dimension of current carrying parts, then FEA based approach proves time effective. In this tool, only the conduction equation is solved while convection is treated as a boundary condition by providing empirically estimated heat transfer coefficients This section gives details of this methodology for the same MCCB discussed above.

Heat generation due to current flowing through MCCB is first predicted by electromagnetic analysis carried out in ANSYS Maxwell like the method discussed above. The heat loads are imported to ANSYS Steady state thermal module where various modes of heat transfers are computed. Temperature from thermal analysis is again fed back into Maxwell where electrical conductivity is modelled as a function of temperature. This iterative process is continued until the temperature changes in two successive iterations are less than 1%.

Boundary Conditions

Convection from external surfaces to ambient: The casing and the cable dissipate heat to ambient by convective heat transfer. Heat transfer coefficients are calculated based on empirical correlations and modelled as function of surface temperature. The reference temperature used to compute heat dissipation by this mode is the ambient temperature.

Radiation: Both internal and external radiation are modelled using radiosity method after computing view factor for all participating surfaces by hemicube method.

Internal convection: surfaces enclosed within the casing exchange heat via convection through internal air. This effect is captured by creating a pilot node with assumed temperature. The internal surfaces dissipate

$$Q_i = h_i A_i (T_i - T_{pilot\ node}) \qquad \ldots(7)$$

The pilot node temperature is then obtained iteratively by ensuring the total heat generation in the domain is equal to total heat dissipation.

Results and Discussion

Fig. **4** shows comparison of test results with simulation. As can be seen, the methodology can predict temperatures on current path within 10° C on current path but cannot predict the temperature rise on the casing sides accurately.

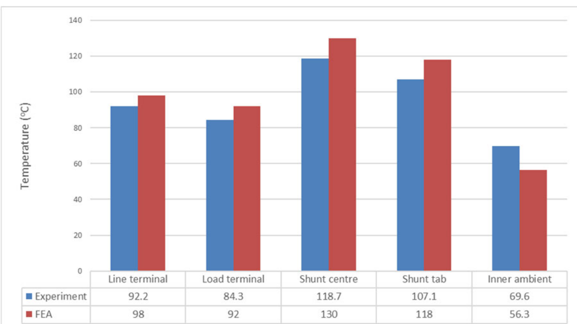

Fig. 4. Comparison of temperature predicted by FEA method and experiment

Another limitation of FEA based methodology is the inability to predict air temperature within the casing. Air temperature within the casing is important to determine to ensure reliability of electronic components inside the breaker.

Considering these limitations FEA methodology is best suited where temperature rise along the current part is only of interest. It is recommended to use CFD based model when accurate estimation of air or casing temperature is required.

Thermal Network Model

During the concept generation stage of product development using a full-fledged FEA or CFD based model may prove unviable as the detailed CAD models and inputs may not be available also the time to evaluate minor changes in dimensions is large using the first two methods. In such scenario, analytical model built using thermal resistances can prove effective.

Thermal network model involves constructing a thermal resistance network of electrical device under consideration using analogy between current flow and heat transfer. The temperature difference is equivalent to potential difference in electrical circuits while heat flow is equivalent to current flow. Thermal resistance is then given by equation

$$R_{th} = \frac{\Delta T}{Q} \qquad \ldots(8)$$

Resistance offered by conduction, convection and radiation is then given by equations

$$R_{cond} = \frac{L}{KA} \qquad \ldots(9)$$

$$R_{conv} = \frac{1}{hAs} \qquad \ldots(10)$$

$$R_{rad} = \frac{1}{h_r As} \text{ where } h_r = 4\varepsilon\sigma {T_{avg}}^3 \qquad \ldots(11)$$

Where R_{th}, R_{cond} , R_{conv} and R_{rad} denote the thermal resistance, conduction resistance, convection resistance and radiation resistance respectively. L, A and As denote Length, Cross sectional area and surface area of the component. h and h_r denote the values of convection and radiation heat transfer coefficients respectively. ε,σ and K denote emissivity, Stephen Boltzmann constant and thermal conductivity respectively.

Following Values are used for these parameters

TABLE 2

Parameters for thermal network model

Parameter	Value
K	390 W/mK (for copper) 0.3 W/mK (for plastics)
ε	0.05 for metals, 0.9 for plastics
σ	5.670374419 × 10-8 W/m^{2}K^4
h	Calculated based on empirical correlations

A network can be built using these resistances in which components are represented by their conduction resistance connected to nodes where temperature is to be determined. The heat dissipation due to convection and radiation can be represented by their respective resistance. Fig. **5** shows one such network constructed for an ACB

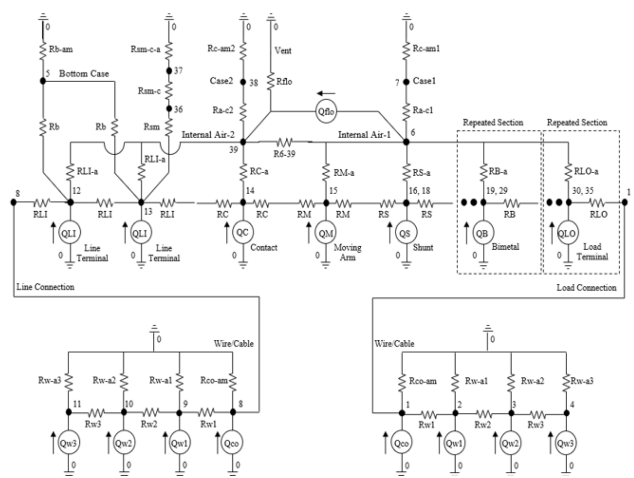

Fig. 5. Schematic of network model for MCCB

By equating total heat flow at each node to zero we can get set of simultaneous equation which can then be solved to get temperatures at the nodes.

Figure 6 shows comparison between temperature rise predicted by network model and test data for an MCCB. Compared to CFD or FEA based model the accuracy is low in this model although the trend of temperature rise across various components is captured correctly. Thus, this kind of analysis can be used for concept evaluations during initial stages of product development.

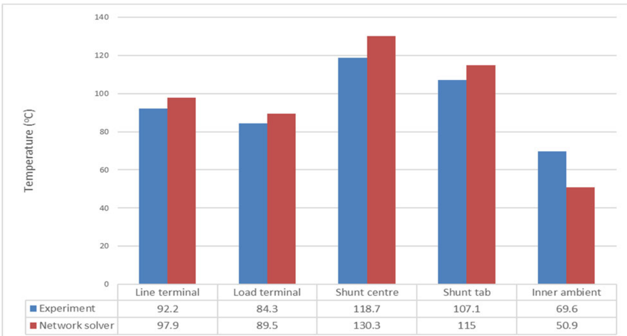

Fig. 6. Comparison of temperature predicted by network model and experiment

Comparison and Comments

Fig. 7 shows comparison of temperature predicted by the three methods discussed above.

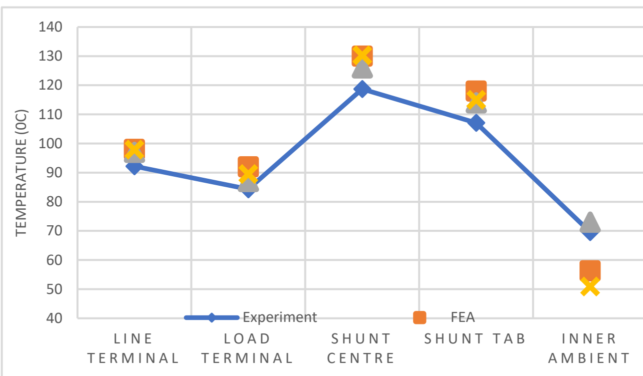

Fig. 7. Comparison of temperature predicted by three methods with experiment

Figure 7 shows comparison of temperature predicted by the three methods discussed above. It can be seen that, for simple switchgears with small air cavities and no vents all the three methods can predict the temperature rise on current carrying components with fairly good accuracy. CFD has a clear advantage in predicting air temperatures near area of interests as air flow is accurately captured. If vents are present or forced convection heat transfer is involved CFD proves to be considerably more accurate than other two methods but at the cost of higher meshing and computational effort. Network-based solver is accurate if the cross section of current carrying parts is constant and does not involve complex curved shapes.

Conclusion

Three methods to predict temperature rise in circuit protection devices were discussed along with advantages and limitations. Following guidelines can be used when deciding simulation approach for switchgears 1) FVM based approach should be used when accurate information about case temperature, air temperature is important or vents and fins are to be optimized 2) FEM based approach should be used when only accurate information about temperature of current carrying parts is needed or sizing of conducting bodies is to be optimized. 3) Network based method should be used during initial approximate sizing of current carrying parts.

References

[1] Paulke, J., Weichert, H. and Steinhaeuser, P., 2002. Thermal simulation of switchgear. *IEEE Transactions on Components and Packaging Technologies*, 25(3), pp.434-439.).

[2] Frei, P. U., & Weichert, H. O. (n.d.). Advanced thermal simulation of a circuit breaker. *Proceedings of the 50th IEEE Holm Conference on Electrical Contacts and the 22nd International Conference on Electrical Contacts Electrical Contacts, 2004.* https://doi.org/10.1109/holm.2004.1353102

[3] Bedkowski, M., Smolka, J., Banasiak, K., *et al.* 2014. Coupled numerical modelling of power loss generation in busbar system of low-voltage switchgear. *International Journal of Thermal Sciences*, 82, pp.122-129.

[4] Checurri, K., 2007. *Thermal Network Theory for Switchgear under continuous current.* PhD. NIT Rourkela.

[5] Yu, X., Yang, F., Bing, G., Liu, H., Li, X., Ai, S. and Wu, X., 2019. Investigation on the Thermal Performance of a 363 kV Vacuum Circuit Breaker Using a 3D Coupled Model. *IEEE Access*, 7, pp.128606-128616.

[6] Molitor, F., Shoory, A., Sologubenko, O., Kaufmann, P., Kraft, K., Janos, J., Vitek, L. and Iordanidis, A., 2021. Thermal Analysis and Design of Laminated Bus Plate Based Low Voltage Switchgear. *IEEE Transactions on Power Delivery*, 36(3), pp.1440-1448.

Address correspondence to *Mr. Avadhoot Kittur, Lead Engineer, Modelling and Simulation COE, Eaton Technologies, Survey No. 77, Plot No. 1, Cluster C, Wing 1, EON Free Zone, Kharadi, Pune – Maharashtra*
Email: AvadhootKittur@Eaton.com
Phone: 09619870759

ARAI Journal of Mobility Technology
Volume 2 • Issue 2 • April–June, 2022, pp. 233-248
Research Paper
https://doi.org/10.37285/ajmt.1.2.10

Lithium-Ion Battery Technologies for Electric Mobility – State-of-the-Art Scenario

Nagmani, Debanjana Pahari, Ashwani Tyagi and Sreeraj Puravankara

School of Energy Science & Engineering, Indian Institute of Technology Kharagpur, Kharagpur, West Bengal, India

ABSTRACT

Rechargeable batteries are an integral part of all types of electric vehicles (EVs). Batteries must contain higher energy-power densities and longer cycle life for an EV system. Lead-acid batteries, Nickel-metal hydride batteries, and Lithium-ion batteries (LIBs) have been employed as charge storage in EV systems to date. Lead-acid batteries and Nickel-metal hydride batteries were deployed in EVs by General Motors in 1996. However, the low specific energy in Lead-acid batteries (34 Whkg^{-1}) and high self-discharge (12.5% per day at r.t.) in Nickel-metal hydride batteries have marked these batteries obsolete in EV applications. LIB~~s~~ currently occupy most of the EV market because of their high specific power (~130-220 Whkg^{-1}) and a low self-discharge rate (~5% per month). The current technological maturity and mass production in LIBs have reduced the overall battery cost by ~98% in the last three decades, reaching an average value of $140 kWh^{-1} in 2021. Although a game-changer in battery technologies, LIBs encounter various challenges: high cost, low safety, less reliability, and immature infrastructure despite environmental benignness. Overcharging and overheating of LIBs can cause thermal runway leading to fire hazards or explosion. Declining Li-resources also raise concerns regarding the reliability and shelf-life of LIB technology. Hence, a critical assessment of Li-ion chemistries is essential to comprehend the potential of LIBs in electric mobilities and to realize the prospects in EVs.

KEYWORDS: Li-ion Battery Technology; Electric Vehicles; Energy density; Well-to-Wheel; Battery Chemistry; High Voltage Cathodes; Safety

Introduction to Electric Mobility – Battery on Wheels

Electric Mobility in the 20th Century

Transportation and vehicular mobility have been significant aspects of modern civilization, ensuring connectivity and facilitating socio-economical development. Today, most automobiles on the road run with conventional fossil fuels like gasoline and diesel. In an Internal Combustion Engine (ICE), incomplete combustion results in greenhouse gas (GHG) emissions contributing to 25% of the total GHG emissions worldwide. As the global consensus grew, green and sustainable alternatives emerged towards the electrification of transportation sectors worldwide. However, electric vehicles (EVs) are historically older technologies as compared to ICE-based automobiles [1]. Battery-powered car first appeared in the early 1800s, followed by electrified locomotives in the 1830s [2]. Patents were granted in England and America in 1840 and 1847 to use electrified rails [3]. Almost a decade later, Gaston Plante invented rechargeable lead-acid batteries in 1859 [4], making battery-operated vehicles viable. However, the limitations of a naïve technology, the people's obsession for "powerful machines," and the lack of an appreciable range of EV vehicles with low energy density rechargeable batteries made the technology obsolete [5].

Due to the limited energy/power storage and low driving range, battery-operated vehicles had never gained popularity in the 19th century and were replaced by gasoline-fueled engines in the early 1900s. ICE as the power generator dominated the automobile market till the 1970s. The petroleum embargo in the 1970s resulted in a rapid increase in fuel cost, [6], [7] forcing the world into more sustainable and green solutions for mobility. The global consensus about the depletion of fossil fuel resources and global warming (0.4°C from 1970 to 1984) due to GHG emissions has fueled the revival of electric automobiles. In 1996, rechargeable Lead-acid batteries (PbA) and Nickel-metal hydride (NiMH) batteries were deployed in EVs by General Motors. [8], [9], [10] Compared to ICE-based vehicles, the low-range EVs failed to spark consumer confidence, and the battery-powered EVs remained more as future prototype vehicles.

The development of rechargeable Li-ion batteries in the 1990s (LIBs) has led to a battery revolution in consumer electronics. Since then, the evolution of LIBs as sustainable solutions as EV batteries has reduced the usage of existing rechargeable PbA and NiMH batteries

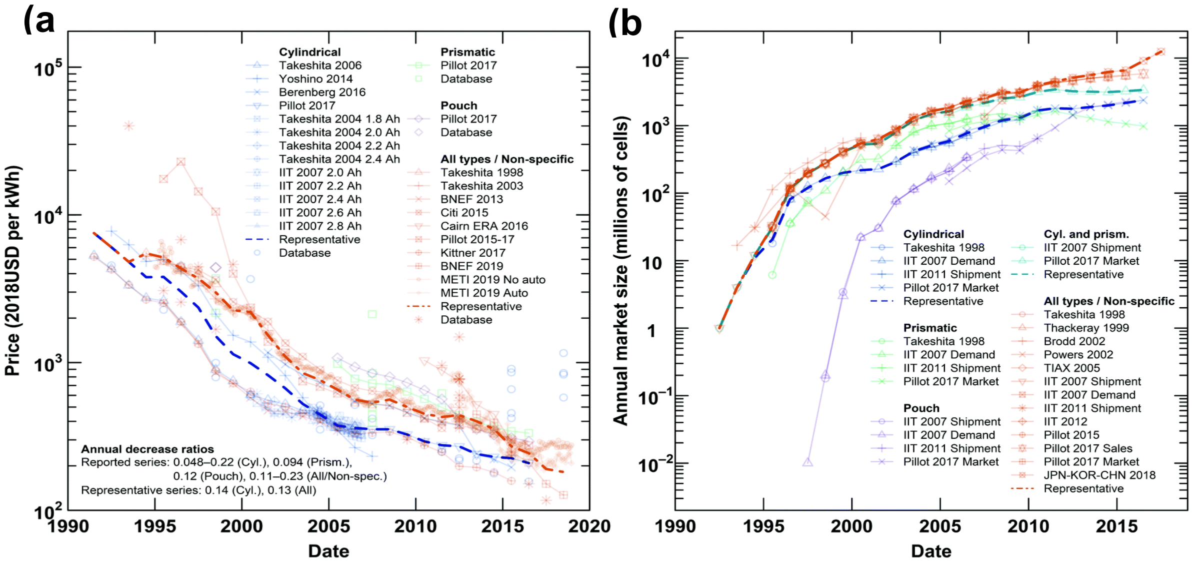

Fig. 1. The progress trends of LIB in terms of (a) price ($/kWh), and (b) Market growth volume (millions), since 1990 [Reproduced with permission from ref. 11. Copyright 2021, Royal Society of Chemistry].

due to their higher energy density (~130-220 $Whkg^{-1}$) and shallow self-discharge rate (~5% per month). LIBs provide the best choice in terms of energy and power densities, flexibility, and compact cell designs. Figure 1 illustrates the progress trends of LIB in terms of cost ($) per kWh and its market growth since 1990. R&D and mass production of LIBs has reduced the total cell cost by ~98% in the last three decades, reaching an average value of $140 $(kWh)^{-1}$ in 2021[11]. However, LIBs encounter a few challenges due to the limited abundance of lithium sources and the inadequate infrastructure for widespread EV applications. Cell safety and less service reliability of LIBs impede the growth of EVs. New-edge LIB technologies involving cheaper, safer, and sustainable materials have gathered enough attention in the EV market to eliminate these barriers.

This review provides an overview of EVs and the different battery technologies used in electric vehicles, focusing on the state-of-the-art LIB technology for EVs. The current global e-mobility scenario with OEM in battery technologies and automobile manufacturers for Hybrid (HEV), Plug-in Hybrid (PHEV), and All-Electric Vehicles (AEV) is discussed, along with an assessment of materials used as the anode, cathode, and electrolyte for commercial LIBs. The current status of LIBs for e-mobility from an Indian perspective is also presented.

Classifications of Electric Vehicles

Electric vehicles can be broadly classified into hybrid electric vehicles (HEV) and all-electric vehicles (AEV). A hybrid vehicle sub-class is a plug-in hybrid electric vehicle (PHEV) recharged using an external power source. A classification table of various technologies is shown in **Table 1**. The low carbon emission has caused a paradigm shift in consumer vehicles. The sustainable solutions nature of EVs has resulted in a surge in the EVs market share, reflecting the gain in consumer confidence, quality, and performance. However, the cost-effectiveness of EVs is still a significant challenge compared to conventional ICE vehicles. Figure 2(a) shows the progress of electric vehicles (in millions) among the major countries like China, USA, and Europe since 2010. The light passenger vehicles have drawn significant attention, and the demands have increased over 10 times since 2012 (Figure 2(b)).

TABLE 1:

Comparing EV technologies with ICE vehicles.

Type of vehicle	Fuel	Advantages	Disadvantages
ICE-based vehicle	Gasoline, Diesel, CNG	Proven technology and established infrastructure, Consumer confidence	High emissions, High maintenance
HEV	Gasoline, Diesel, CNG based fuel and Electricity	Lower emissions, Hybrid Technology and utilization as per need	Emissions, No direct charging from the grid
PHEV	Gasoline, Diesel, CNG based fuel and Electricity	Lower emissions, Hybrid Technology and utilization as per consumer need, Direct grid charging	Emissions, Lack of charging infrastructure
AEV	Electricity	No fossil fuel, Zero emissions, Sustainable with electricity from renewable energy, Low maintenance	High electricity demand, Non-renewable electricity generation grid

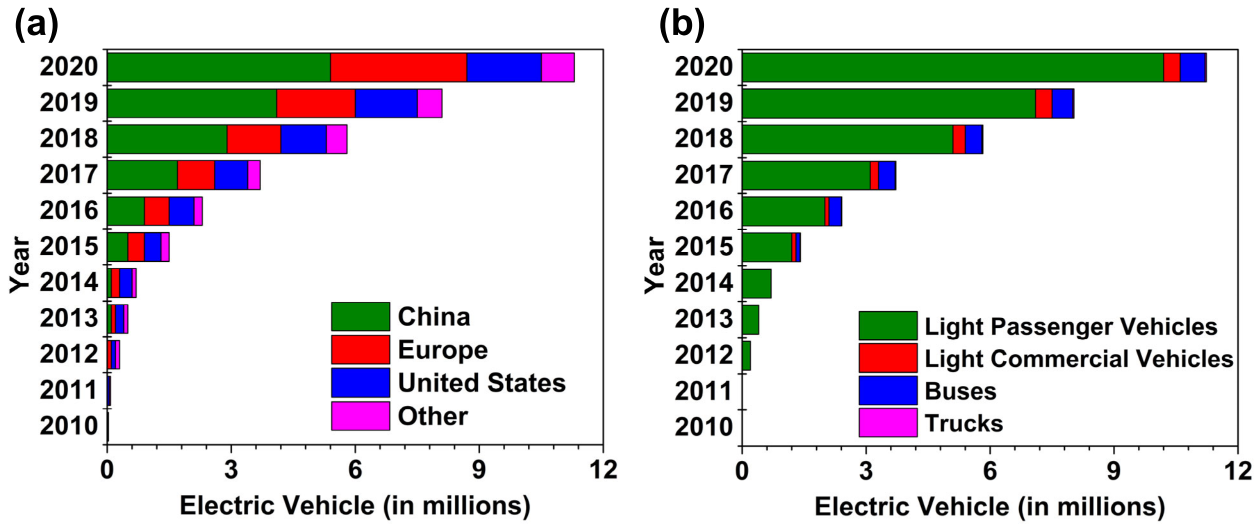

Fig. 2. (**a**) Progress in EV global market share since 2010, (b) The demand of different types of EV (in millions) since 2010 [12].

Hybrid Electric Vehicles (HEVs)

Hybrid electric vehicles (HEVs) combine traditional internal combustion engines (ICE), and electric motors as an alternate fuel for better customizable vehicle performance. Although the target vehicles for HEVs are battery-operated electric cars, various other vehicles, including pickup trucks, tractors, buses, are also beneficiaries in the EV market. A full-hybrid electric vehicle can run with just the ICE, the electric motor, or both. The regenerative braking in modern HEVs convert kinetic energy to electrical energy, and an in-built energy storage device (battery/ supercapacitor) stores the power for later use as employed in Toyota Prius [13]. After the Toyota Prius market's inception in 1997, a surge in full-hybrid electric vehicles has been evident in the automotive market. Over 17 million HEVs are currently operational worldwide. The notable examples of HEVs are Toyota Prius by Toyota, Silverado Hybrid pickup truck by Chevrolet, Saturn Aura Greenline and Malibu Hybrid by General Motors, Ford Fusion Hybrid by Ford, and Honda Accord Hybrid by Honda [14]. Figure 3(a) shows the global market share of HEVs by different automotive manufacturers till 2020. However, the simultaneous hydrocarbon fuel consumption in HEVs will not be environmentally sustainable.

Plug-in Hybrid Electric Vehicles (PHEVs)

Unlike classic HEVs, Plug-in hybrid electric vehicles (PHEVs) can be charged from an electrical power station when needed. PHEVs consist of an onboard charger and a charge port connected to the traction battery pack and electric motor. PHEVs are also recharged by regenerative braking, similar to conventional HEVs. PHEVs are common in commercial vehicles - passenger cars, trucks, buses, trains, and two-wheelers run with PHEV versions. As PHEVs can withdraw power directly from the electricity grid, a sustainable approach for powering the grid can be accepted by considering renewable energy generators compared to traditional HEVs.

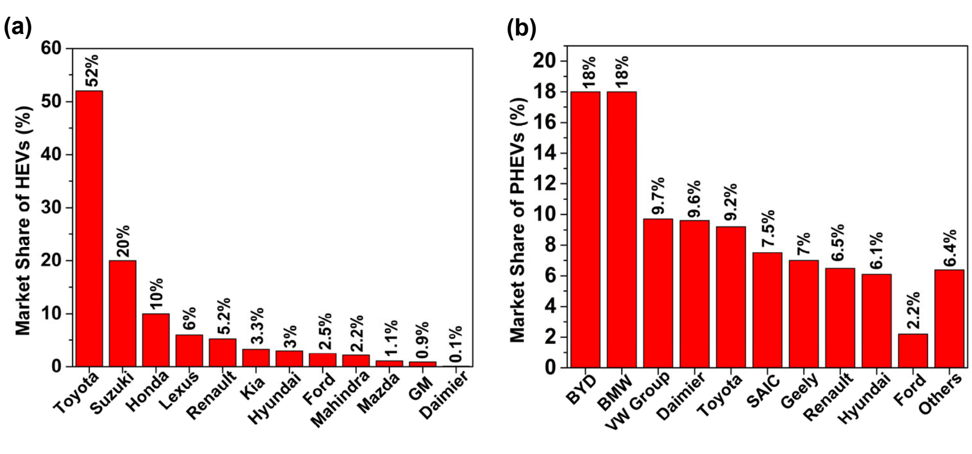

Fig. 3. Global market share (%) of (a) HEV, and (b) PHEV, till the year of 2020. [15].

China, USA, Canada, Japan, Norway, Germany, France, UK, and the Netherlands are the primary markets for PHEVs. The PHEV market models include Mitsubishi Outlander P-HEV, Chevrolet Volt, and Toyota Prius PHV. Five bestselling Cumulative sales of PHEV models have been recorded as ~8,00,000 units until 2018 [16], [17]. PHEVs can save 60% and 40% of the energy costs compared to gasoline-fueled vehicles and classic vehicles HEVs, respectively. The vehicle operating costs are minimized by plugging the battery into charging stations instead of utilizing the onboard charger's power. The onboard charger acquires power from ICE, which adds more tailpipe emissions. However, a larger battery pack to store the energy eventually increases the battery cost. The battery cost for the Chevrolet Volt model PHEV-40 (Li-ion battery pack of 8.0 kWh) has been estimated as US$14,000 in 2010, which can still save around 55% gasoline consumption compared to a classic HEV. PHEVs's global market share (till 2020) is dominated by BYD and BMW, as shown in Figure 3(b).

All-electric Vehicles (BEVs)

All-electric vehicles (AEVs) or pure electric vehicles run on electrical power generated by high-performance batteries. The stored chemical energy in the battery packs is converted into kinetic energy with the help of electric traction motors. The energy supply is controlled and monitored by the power electronics controllers. Numerous applications of AEVs are reported to date, including motorized two-wheelers, passenger-carrying four-wheelers, busses, trains, goods carriages. Based on their applications, AEVs are broadly classified into two groups; heavy and light AEVs. All-electric trains, trucks, and buses are included in heavy AEVs. While light AEVs include electric cars, motorcycles, scooters, and rickshaws. The global emerging AEV market is currently dominated by Tesla, Mitsubishi, General, Nissan, GM, BMW, and Audi, as shown in Figure 4(a). Since 2011, the market growth of AEV and PHEV has been expanding, and AEV has been popular in terms of annual sales in the last decade (Figure 4b).

Lead-acid battery-operated passenger-carrying three-wheelers currently occupy the majority of the Indian AEV market. The current Indian major market players for four-wheeler AEV's are Tata Motors Limited, Maruti Suzuki India Limited, Mahindra & Mahindra Limited, MG Motor India, Toyota Kirloskar Limited. Recently, Infraprime Logistics Technology (IPLT) launched a heavy-duty 60-tonne electric truck, claiming a mileage of 400 km (without load) and 200 km (with load) [17].

Batteries for EVs

As an integral part of the EV system, energy storage devices can consist of batteries, supercapacitors, or fuel cells. Nowadays, batteries impart one of the best performances as the state-of-art lithium-ion battery (LIB) technologies exert high power and energy densities with compact, lightweight designs. Compared to traditional Lead-acid (Pb-A) batteries and a few decades-old Nickel-metal hydride batteries (NiMH) technologies, LIBs extend much higher economic and environmental benefits. Figure 5 shows the performance parameters (energy density, single-charge range, and battery mass for EVs) for different battery technologies. A comparison shows the advantages and disadvantages of different battery technologies (Table 2). However, in either case, the expensive and high emitting gasoline-based fuel consumption is restricted to quite an extent, making the EV technology more attractive.

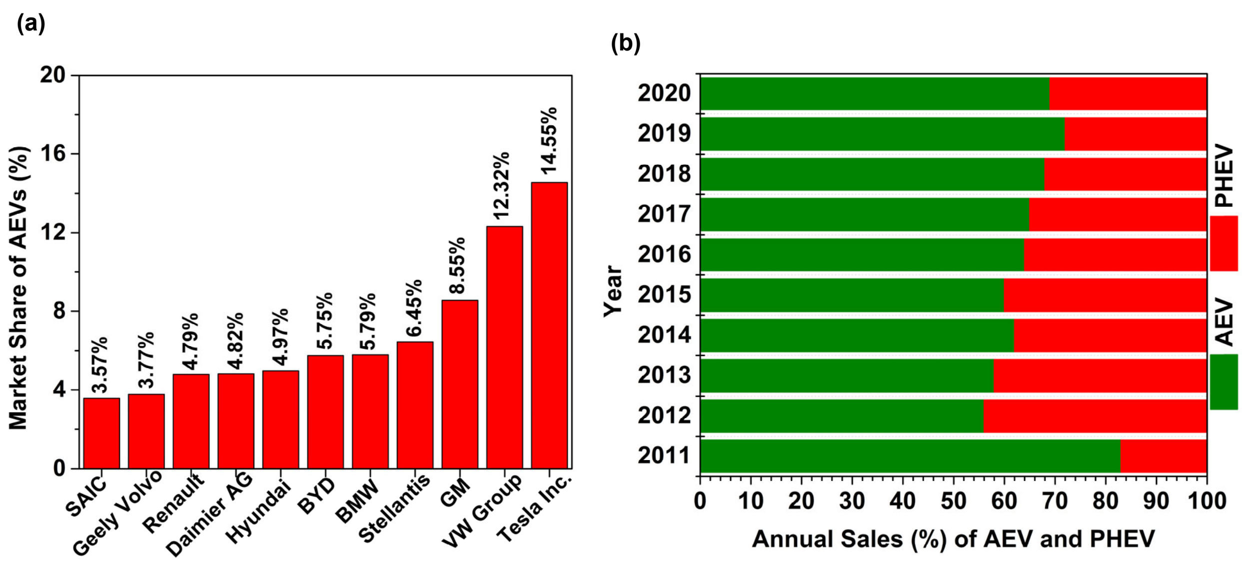

Fig. 4. (a) Global market share (%) of AEV till the year of 2020; (b) Annual sales (%) comparison of AEV and PHEV from 2011 to 2020. [15]

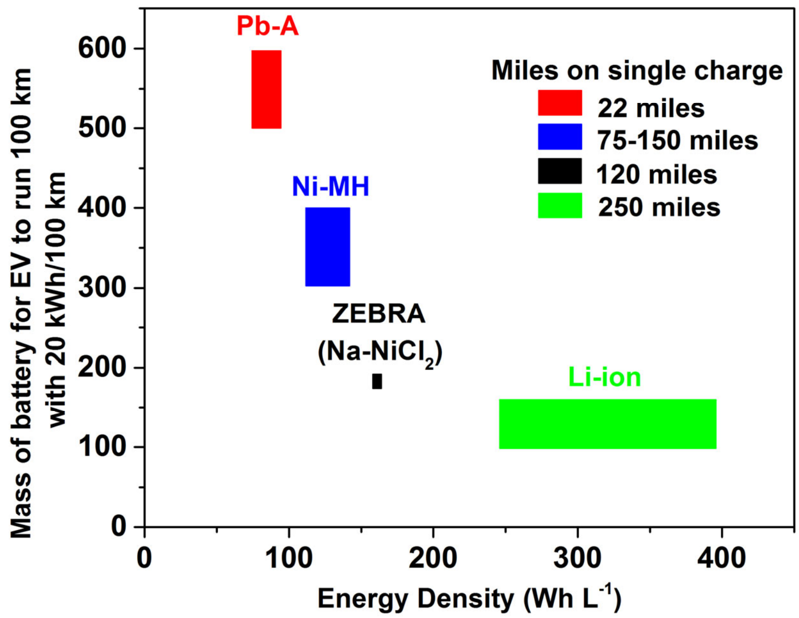

Fig. 5. Comparison of battery technologies in terms of energy density, battery weight, and range (miles) on a single charge.

TABLE 2:
Comparison of different Battery Technologies for EVs

Battery System	Nominal Cell Voltage (V)	Capacity (Wh/kg)	Advantages	Disadvantages
Pb/Acid	2	35	Low cost, Rugged and proven technology	Low specific energy, poor charge retention
Ni-MH	1.4	55	High storage capacity, good cycle life, resistance to overcharge	High initial cost, high self-discharge rate
Li-ion	up to 4.2	135	High energy and power density, matured technology, durable, flexible	High cost, Safety concerns, poor charging infrastructure

Lead-acid Batteries

Rechargeable lead-acid (Pb-A) batteries were the earliest generation of batteries employed in EV applications. The low cost has made their applications affordable in any stationary or mobile use due to the matured and rugged technology and sufficient raw materials availability. Pb-A batteries were used in most of the conventional battery electric vehicles in the 20th century. However, the low specific energy of 34 Whkg^{-1} has failed to satisfy the extended driving range requirements. Also, heavy-weight Pb-A batteries occupy at least 20-25% of the total vehicle weight. Therefore, Pb-A batteries usage has been restricted into two separate areas in the current scenario. The Pb-A batteries are being used as start lighting-ignition batteries in automobile [18] to start the engine. Simultaneously, the deep-cycle Pb-A batteries are expected to store sizeable electrical energy for moving the wheels. In the Indian market, over 1.5 million three-wheelers (E-rickshaw) based on Pb-A batteries are on the road. A gasoline-powered rickshaw has a running cost of about 4/km, while the running cost of its e-rickshaw is coming around 0.5/km [19]. Working temperature conditions play a vital role in the usage of Pb-A batteries. Flooded Pb-A batteries deployed to start the engine need to be monitored regularly. The electrolyte of these batteries needs to be replaced periodically as at moderate/higher temperatures, the evolution of hydrogen, oxygen, and sulfur gases are pervasive during charge/discharge. In lower temperatures, the efficiency of deep-cycle Pb-A batteries drops quite an extent. All-electric Pb-A powered EVs were introduced to the market by GM. The 1st generation Pb-A [9] operated GM EV 1 has provided charge storage for 130-160 km mobility. Low energy storage capacity and poor service life of Pb-A batteries have indicated its restricted use in the current EV market.

Nickel-metal Hydride Batteries

The commercialization of Nickel-metal hydride (Ni-MH) batteries in EV applications started in the late 1990s. Toyota has introduced Toyota Prius EV as the world's first commercial HEV in Japan. Prius model functions with a Ni-MH pack providing a significant driving range. General Motors and Ovonic Battery's joint venture emerged as GM Ovonic L.L.C. in 1994, which has developed various generations of Ni-MH batteries for electrified GM vehicles. GM Ovonic has served impressive and extensive research on Ni-MH batteries, which pioneered the EV evolution [20]. The first-generation GMO-1 batteries were assembled using 11 Ni-MH cells with 90 Ah cell capacities in a series connection. Each Ni-MH cell could exert 70 $Whkg^{-1}$ of specific energy and 170 WhL^{-1} of volumetric energy density. The battery pack has supplied 13.2 V voltage with 1.2 kWh capacity. In the second generation, GMO-2 batteries, the ultimate power and energy densities were kept constant while compacting the cell design. A total no of 10 individual Ni-MH cells well assembles into a battery pack. GMO-2 batteries have provided 12 V voltage with 100 Ah capacity. The overall specific energy was noted as 80 $Whkg^{-1}$ per battery pack. The second-generation GMO-3 batteries were assembled with Zr–Ti–Ni-based metal hydride alloy as the electrode leading to a storage capacity of 380-400 $mAhg^{-1}$. Such improvement in cell-level energies has eventually led to obtaining a battery pack with >95 $Whkg^{-1}$ specific energy.

GMO-3 batteries are remarkably tolerant of aggressive conditions. The 160,000 km driven GMO-3 batteries have shown high thermal stability even at 60°C and excellent retention of 80-90% of the energy efficiencies. GM EV1 e-cars launched in 1999 with Ni-MH batteries have furnished a driving range of 225 km [10]. Several other fully electric and PHEV models from automobile manufacturers like Daimler Chrysler, Ford, General Motors, and Honda were functional with Ni-MH batteries as the last century's charge storage device. However, high-performance LIBs have gradually acquired the EV market, replacing Pb-A and Ni-MH technologies.

Lithium-ion batteries (LIBs)

Lithium-ion batteries (LIBs) furnish many applications, from mobile phones to transport vehicles (Figure 6). Each application requires a different set of electrochemical performances and material components. The choice of materials in LIBs for consumer electronics may not be ideal for stationary storage or electric vehicle application. High gravimetric and volumetric energy densities are prerequisites for EV applications. The choice of a battery system's cathodes, anodes, and electrolyte materials have varying impacts on the application's targeted needs.

LiB Technology

Electrode Materials for LIBs

Lithium cobalt oxide (LCO) is the most widely used cathode in consumer electronic devices. It falls short as a suitable cathode in EVs as it inherently suffers from structural instabilities in the overcharged state at the cost of battery lifespan. In contrast, Lithium manganese oxide (LMO), Lithium nickel cobalt aluminum oxide (NCA), Lithium nickel manganese cobalt oxide (NMC), and Lithium iron phosphate (LFP) materials are widely accepted cathodes as a replacement for LCO. Graphitic anodes are still indispensable in LIBs for EV applications on the anode side.

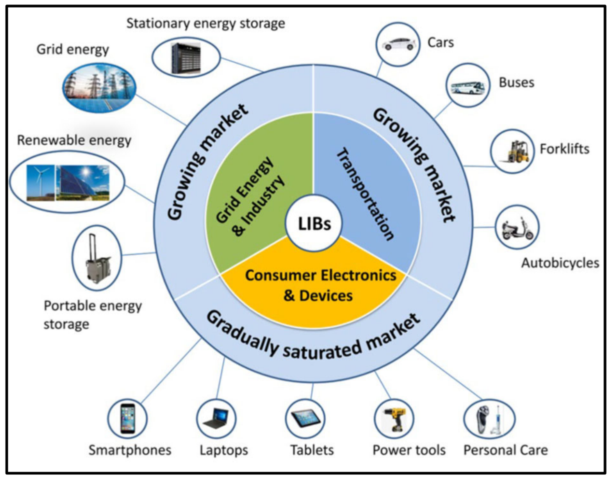

Fig. 6. Lithium-ion battery technology devices for various energy sectors [Reproduced with permission from ref. 21, Copyright @2019 Springer Nature]

Cathodes

The cathode contributes to the maximum cost in manufacturing LIBs, making optimal material and cell design essential to achieve high performance, as shown in Figure 7. Batteries for EVs must be small, light, and portable. Hence, such small and lightweight batteries should contain cathodes of high gravimetric and volumetric energy densities. In reality, only a few cathodes qualify these criteria. LMO, LFP, NCA, and NMC cathodes are notable examples employed in current technologies.

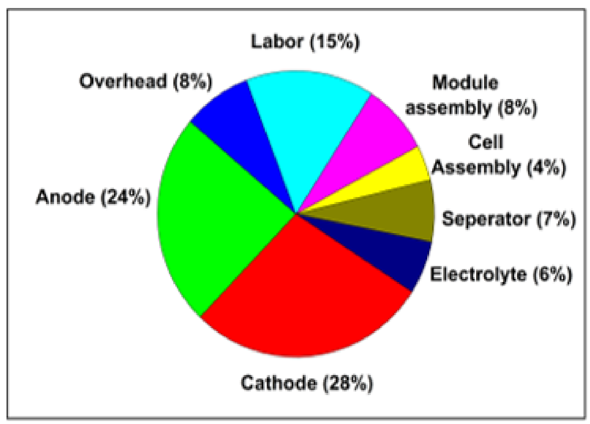

Fig. 7. The cost breakdown of various components in LIB fabrication technology [Reproduced (adapted) with permission from ref. 22 under a Creative Commons Attribution License Copyright © 2020 MDPI].

Lithium Iron Phosphate (LFP)

In 1996, JB Goodenough and co-workers first explored LFP as a potential replacement of LCO cathodes. [23] LFP cathodes provide high thermal stability, long cycle life, and significant power density. A polyanionic-based cathode can also extend the stability range at a higher charged state, unlike LCO. However, for the same reason, LFP suffers low electronic conductivity compared to oxide-based cathodes. Such low electronic conductivity reduces the fast charge capabilities, making its EV applications critical. Also, LFP cathodes exert a low average voltage (3.4 V), leading to a comparatively low gravimetric energy density of ~120 $Whkg^{-1}$ and volumetric energy density of ~220 WhL^{-1} [24]. For high-performance EV applications, smaller-size, compact, and high energy density battery packs are essential. Such low volumetric energy density in LFP cathodes qualifies them as suitable systems in larger vehicles such as buses and goods carriages. BYD e6 is an AEV that runs on prismatic cell types based on LFP cathode and provides a range of 300 driving kilometers. A123 pouch cells fabricated for Chevrolet spark e-cars employ carbon-coated LFPs as cathodes and extend the volumetric energy density up to ~250 WhL^{-1}. However, much lower battery energy (21 kWh) and range (130 km) unfortunately do not meet the current EV requirements [25].

Lithium Nickel Cobalt Aluminum Oxide (NCA)

As a cheaper, stable alternative of LCO, $LiNiO_2$ (LNO) cathodes have been identified with a high theoretical capacity of 275 $mAhg^{-1}$. Despite the advantages, LNO cathodes undergo structural deformations while charging. Similar size Ni^{2+}-ions (0.69Å) diffuses into Li-layer (ionic radii of Li^+ is 0.76 Å), causing an irreversible phase transition [26]. Substitution in the transition metal site has significantly improved the phase stability in LNO cathodes. One of the modern EV battery cathodes, NCA ($LiNi_{0.8}Co_{0.15}Al_{0.05}O_2$), is synthesized via substituting Ni with 15 mol% Co and 5 mol% Al ions [27]. Tesla EV models employ NCA cathodes provided by Panasonic batteries. Al^{3+}ions substitution helps improve the structural and thermal stability, increasing the voltage of operation and subduing the structural deformations at high voltage charging [28].

On the other hand, the inclusion of Co^{3+}ions into the Ni-site can suppress Ni-migration into Li-layer and provide extra electrochemical support during the battery's charging/discharging [29]. NCA cathodes can successfully extend gravimetric and volumetric energy densities of 236 $Whkg^{-1}$ and 673 WhL^{-1}, making them one of the most potent cathodes in EV industries. Despite its toxic and expensive Co-component, NCA cathodes are typical examples in EV batteries due to their long service life of more than 15 years.

Lithium nickel manganese cobalt oxide (NMC)

NMC cathodes have emerged as economically viable solutions of LCO cathodes as expensive Co-transition metal is replaced by Ni and Mn in the transition metal layer. A variety of NMC compositions are currently used in the EV market. NMC majorly includes low or medium Ni-containing cathodes. $LiNi_{1/3}Mn_{1/3}Co_{1/3}O_2$ (NMC-111) is counted as a low Ni-containing cathode. Medium Ni-containing cathodes are typically $LiNi_{0.4}Mn_{0.4}Co_{0.2}O_2$ (NMC-442) and $LiNi_{0.5}Mn_{0.3}Co_{0.2}O_2$ (NMC-532) [30]. The notable producers of NMC cathode-based batteries are Panasonic, LG Chem, Sanyo, and Toshiba, which have successfully been employed in EVs such as Tesla 3, Chevrolet Bolt, Renault Zoe, VW e-Golf, and Honda Fit EV. NMC cathodes can furnish sufficient energy densities, good cycle stability, and high thermal stability. Tesla 3 EVs can provide a 350-500 km driving range with 75-100 kWh battery packs. Additionally, new-edge Ni-rich NMCs, NMC-622 ($LiNi_{0.6}Mn_{0.2}Co_{0.2}O_2$) and NMC-811 ($LiNi_{0.8}Mn_{0.1}Co_{0.1}O_2$), have shown their potential to be the future of EV technologies due to enhanced specific energy and low cost [31]. High energy composite-based NMC cathodes were initially considered an alternative solution to minimize cell manufacture costs involving expensive Co-metal. They also provided excellent specific energy of ~900 $Whkg^{-1}$ considering the cathode formula of $xLi_2MnO_3.(1\text{-}x)LiMO_2$ (M=Ni, Mn, Co) [32]. A hybrid system, composite NMC/LMO cathode has proven its worth by delivering 150-160 km driving range. Various oxide-spinel composite cathodes are efficiently utilized in EV models such as Mitsubishi i-MIEV, Ford Focus, and Nissan Leaf. The NCA cathodes can prove the best specific capacity of 200 $mAhg^{-1}$ and the highest thermal stability (even at 60°C). However, the cells suffer from economic constraints. Composites of NMCs are the most suitable cathodes for high-performance EVs. Figure 8a summarizes the different cathode materials in LIBs technology regarding specific energy, energy density, energy efficiency, and working potential.

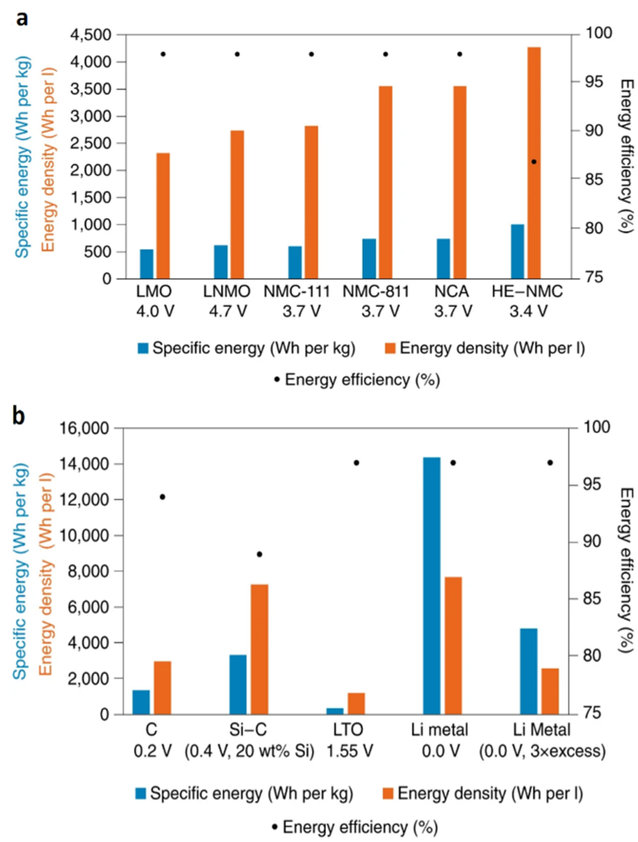

Fig. 8. Specific energies, energy densities, and average energy efficiencies of cathodes (**a**) and anodes (**b**) materials at materials level [Reproduced with permission from ref. 33, Copyright 2018 Springer Nature]

Anodes

Anode materials for LIBs are categorized based on their lithiation/ de-lithiation process. First are intercalation-type anodes materials, in which ions are inserted into the layered structures. Graphite is one of the most common intercalation-type anodes used in LIBs and forms LiC_6 intercalated compound providing a high theoretical capacity (Q_{th}) of 372 $mAhg^{-1}$ with a low volume expansion of about 9%.[34],[35] Many cell manufacturers such as AESC, LG-Chem, Li-Tech, Li Energy Japan, Samsung, and Panasonic use graphite as an anode for EV applications (Table 3).

TABLE 3:

Material Characteristics of different OEM for anode materials in EVs [36].

Anode Materials	Plateau potential vs Li/Li⁺ (V)	Theoretical Capacity (mAh g^{-1})	Advantages	Disadvantages	Battery Manufacturer/ company for EVs
Graphite	0.1	372	Abundant, cheap, long cyclic stability	SEI formation, low energy density, lithium plating	AESC LG Chem Li-Tech Samsung Panasonic
LTO	1.5	175	High coulombic efficiency, negligible volume expansion	Low capacity, low energy density higher plateau voltage	Toshiba Aptiv Altairnano
SiO_x	0.4	4200	Very high capacity for next-generation LIBs.	Low ICE Low electronic conductivity Sudden volume change	Enevate Enovix Huawei Amprius Nanotek

Since 1980, lithium titanate (LTO) has replaced graphite for Li-ion batteries. The spinel structure of LTO is regarded as a precious material due to negligible volume changes during the charge-discharge process, resulting in the electrode's durability [37]. In graphite, lithiation occurs at lower potential (~0.1V) close to metallic lithium. In comparison, LTO, due to higher lithiation potential at around 1.5 V, reduces the chance of metal plating and increases the batteries' safety [38][39]. Lithium titanium oxide (LTO) has been used in LIBs (Toshiba Cell) markets for EV application by Honda and Mitsubishi Company due to advantages of no SEI formation, high rate capability, negligible volume expansion/contraction during cycling. The serious shortcoming of LTO is low Q_{th} (≈ 175 mAh g^{-1}), and high operational voltage (≈ 1.55 V vs. Li/Li⁺) results in inadequate energy density [40],[41]. The Toshiba cells have the lowest specific energy and energy density for Li-ion batteries due to the high voltage plateau and low specific capacity of the LTO anode. The specific energy and energy density of Li-ion batteries come in the range of 90-160 Wh kg^{-1} and 200-320 Wh $L^{-1,}$ respectively, when an individual cell is concerned. Panasonic cells using cylindrical design provide the highest specific energy of 248 $Whkg^{-1}$ and energy density of 630 WhL^{-1} [42]. The electrochemical performance characteristics of anode materials such as specific energy, energy density, working potential, and energy efficiencies are summarized in Figure 8 b.

Alloying-type anode materials (Si, Ge, Sn, Sb metals and metal oxides, sulfides, and phosphides) offer very high specific discharge capacity. However, they suffer colossal volume expansion of more than 300% resulting in poor cyclic stability limiting its practical application [43]. Low-cost silicon has a high theoretical capacity of 4200 $mAhg^{-1}$ dominating graphite and metallic lithium (Q_{th} = 3860 $mAhg^{-1}$) as an anode material. Silicon stored a more significant number of Li-ions upon charging than graphite, giving more range for the EVs on a single charge [44]. Recently, Enevate's silicon-based LIBs deliver a 400 km run on a 5 min charge.[45] Also, to high internal strain, silicon displays low Li^+-ionic mobility and high resistance in the electrical circuit.

The conversion reaction-based anodes such as Fe_2O_3, Co_2O_3, and CuO (transition metal compounds) deliver a higher specific capacity than graphite [46]. Anions (oxides and sulfides) have shown great potential as a high theoretical capacity ranging from 500 to 1500 $Ahkg^{-1}$ is evident [47]. The major drawback of these anodes is the volume expansion during cycling from conversion reactions between products and reactants. It leads to ~~a~~ substantial irreversible capacity loss, low rate performance, and voltage hysteresis due to poor electronic conductivity and loss of contact upon cycling [48].

The alternative anode materials have been explored towards high energy density, long-term cyclic stability, volume expansion, and improved reversible capacity for EV applications. Due to the safety concern and poor cyclic stability, intercalation-type anodes materials attract more attention in LIBs for EV applications. For safe LIBs anode for EVs, SEI's thermal stability is critical to guard lithiated graphite against being exposed to the electrolyte. The coated graphite with Al_2O_3 effectively avoids undesirable reactions to protect lithiated graphite and showed excellent capacity retention even at a higher temperature [49] [50]. The addition of electrolyte~~s~~ additives also provides thermally stable SEIs.

Electrolytes

Electrolyte~~s~~ are the ion-conducting medium sandwiched between two electrode components. The high ionic conductivity, low viscosity, and high cationic transference numbers are essential requirements for a smooth shuttling of Li^+-ions across the electrolytic medium. Four major electrolytes have been explored in LIB systems: organic, aqueous, solid-polymer, and ceramic electrolytes. Among them, organic electrolytes are the most widely investigated systems to date. Organic electrolytes present the maximum electrochemical stability window of 5 V vs. Li/Li⁺ when ionic conductivity maximum is noted as ~8 $mScm^{-1}$. Also, standard organic electrolyte systems are preferred over the other electrolytes due to their high wettability to maintain good surface contact with the electrodes. Organic electrolytes are typically a combination of Li-salt ($LiClO_4$, $LiPF_6$, LiTFSI) and one or more organic carbonate-based solvents such as ethylene carbonate (EC) dimethyl carbonate (DMC), ethyl methyl carbonate (EMC), propylene carbonate (PC) [51]. However, organic solvents are highly flammable and can cause fire hazards when overcharged or used in high-temperature conditions.

Also, the formation of a solid electrolyte interface (SEI) by decomposing electrolytes is critical in batteries' longer cycle life. A stable SEI performs as a protective layer onto the electrode surface whose micro-channels allow the Li^+-ions to traverse the electrode and prevent the electrodes from chemical dissolution. An unstable and outgrown SEI hinders the ionic diffusion leading to poor/zero surface contact. Dendritic growth on the anode surfaces is one of the significant examples of SEI failure [52]. One of the pioneers in the EV market, Tesla, has mentioned its challenges working with classic organic electrolytes due to poor carbon-based electrode stability. Due to organic electrolytes' high flammability and low thermal stability issues, aqueous and solid electrolytes have gained enough interest as green and sustainable solutions [53-56]. Aqueous electrolytes inherently suffer from a low electrochemical stability window (1.23 V) and inefficient SEI formation. However, concentrated aqueous electrolytes in the form of a "water-in-salt" scenario can remarkably improve the electrochemical stability window > 2 V by offering a stable SEI layer onto the anode surface.

Similarly, reliable electrolyte systems can improve battery safety by eliminating organic solvents. Polyethylene oxide (PEO) based polymers and Lithium Super Ion Conductors (LISICON) are widely accepted solid electrolytes in LIB systems.

Current Status of Battery Electric Vehicles

LIBs as high energy density batteries have initially been developed for small-scale stationary storage devices, and the utilization in EV industries was targeted to cut down on conventional fossil fuel usage. Unfortunately, the low earth abundance of LIB raw materials and the high cost slowed down mobility applications during the late 1990s and early 2000s. A sharp reduction of cell cost after 2010 has made the EVs economically viable (Figure 9a). Recent developments in LIBs have significantly dropped the overall battery cost by ~85% in the last decade, reaching a $176 kWh^{-1} in 2019. To this extent, the base price for Honda Clarity e-car has come down below $20,000. However, the high driving range (~300 km) of Tesla X AEVs is still above $100,000. Tesla EVs typically employ high-performance Panasonic batteries with a large-scale production GWh factory established in Nevada, USA. Since the incubation and first production in 2017, the manufacturing cost fell by 30%, and the final production capacity is to reach 150 GWh per year[57].

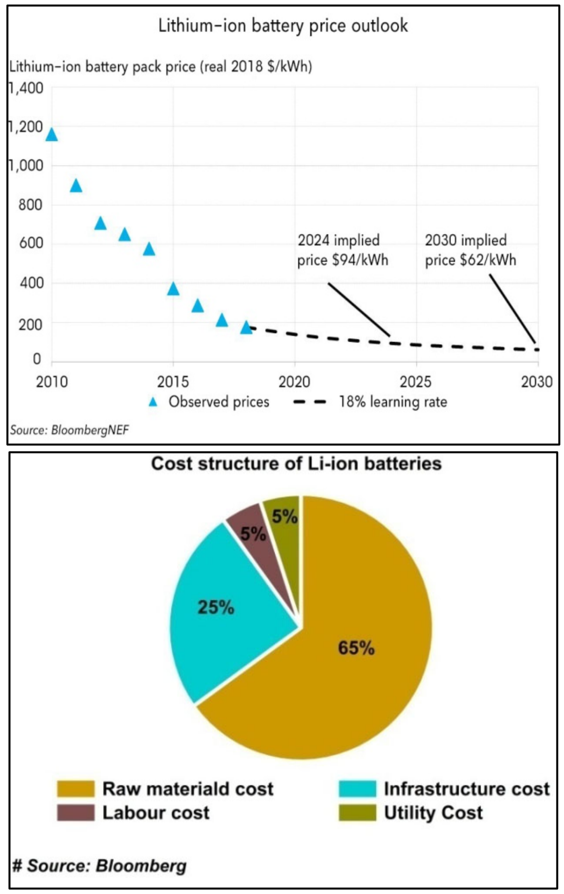

Fig. 9. (a) Actual and projected LIB pack price over the years and (b) Cost break-up of LIBs sourced from Bloomberg NEF [58].

Tesla has been the most prominent service provider in terms of driving range among AEVs. The EV models can run for ~300 km on a single charge with a battery pack energy of 60 kWh. BMW i3, Nissan Leaf, Volkswagen e-Golf, Toyota RAV4EV serve the moderate driving range 170-200 km per single charge. While Fiat 500e, Kia Soul EV, Ford Focus EV, Mercedes B-class Electric, and Mitsubishi I are the low driving range (100-160 km) EVs. Low and moderate driving range EVs cost between $20,000 - $50,000[59]. As expected, the high driving range Tesla models cost ~ $100,000[60]. However, Nissan Leaf EVs provide a driving range (~230 km) with a 62 kWh battery pack and a low price below $30,000 since 2019. The current AEV market models and their battery characteristics are listed in Table 4.

The PHEVs are considered as low-driving range vehicles for 20 to 85 km. Battery capacities of PHEVs are much lower (6-18 kWh) than AEVs as additional gasoline-based fuel provides the necessary power. Chevrolet Volt 2nd generation EVs deliver the highest electric range of 85 km along 595 km of gasoline fuel, leading to 680 km (Table 5). Although small PHEVs' overall costs are lower than AEVs, consumers' interest in AEVs has increased in the last decade.

The growth of electrification of vehicles is still catching up despite the dramatic reduction of battery pack costs. The global market share for PHEVs has increased by only 0.79% in 5 years till 2016. While at a similar period, ICE-based car sales have increased by 97%. There is still a preference for ICE-based cars among consumers over EVs due to the high cost and poor infrastructure of EV technologies. The central and federal government policies keenly promote zero-emission vehicles globally to reduce fossil-fuel dependence. Nissan has received a grant of $32.5 million from the British government to set up a plant for the manufacturing of Nissan Leaf. Toyota has sold roughly 600,000 Toyota Prius EVs only in Europe. The EV penetration percentages are 23.5% in Norway 5.1% in the Netherlands, 3.2% in Sweden, 1.3% in the UK, 1.2% in France, 0.7% in Germany, 0.9% in the USA, and 1.3% in China relative to the country's total light vehicles sold.

Table 4:

Battery packs currently used in All Electric Vehicles (AEV)[61]

Automobile Manufacturer	Model	Battery size (kWh)	Battery Chemistry	OEM	Vehicle range (km)
Tesla	S	60-100	C/NCA	Panasonic/Tesla	334-508
Tesla	X	60-100	C/NCA	Panasonic/Tesla	334-508
BMW	i3	22,33	C/NMC	Samsung/Bosch	129-183
Nissan	Leaf	24,30	C/LMO (C/NMC)	AESC and LG Chem†	135-172
Volkswagen	e-Golf	24,35.8	C/NMC	Panasonic (Sanyo)	135-200
Chevrolet	Spark	19	C/LFP	A123	132
Fiat	500c	24	C/NMC	Samsung/Bosch	140
Kia	Soul EV	27	C/NMC	SK Innovation	145
Smart	Fortwo EV	17.6	C/NMC	LG Chem	109
Ford	Focus EV	35.5	C/NMC	LG Chem	160
Mercedes	B-Class Electric	28	C/NCA, (C/NMC)	Panasonic/Tesla and SK Innovation†	137
Mitsubishi	I	16	LTO/LMO	Toshiba	100
Honda*	Fit EV	20	LTO/LMO	Toshiba	132
Toyota*	RAV4 EV	41.8	C/NCA	Panasonic/Tesla	182
*Discontinued Models.					
†In process of changing suppliers.					
Note: NCA= $LiNi_{0.8}Co_{0.15}Al_{0.05}O_2$, NMC = $LiNi_{1-x-y}Mn_xCo_yO_2$, LMO = $LiMn_2O_4$, C = Graphite, LTO = $Li_4Ti_5O_{12}$.					

Table 5:

Battery packs for current market PHEVs [61]

Automobile Manufacturer	Model	Battery size (kWh)	Battery Chemistry	OEM	Vehicle range (km)
Chevrolet	Volt	18.4	C/NMC	LG Chem	85
Ford	Fusion Energi	7.6	C/NMC	Panasonic	32
Ford	C-Max Energi	7.6	C/NMC	Panasonic	32
BMW	X5	9.2	C/NMC	Samsung/Bosch	22
Hyundai	Sonata Plug-In	9.8	C/NMC	LG Chem	43
Audi	A3 Plug-In	8.8	C/NMC	Panasonic (Sanyo)	26
Volvo	XC90 Plug-In	9.2	C/NMC	LG Chem	40
BMW	i8	7.1	C/NMC	Samsung/Bosch	37
Porsche	Cayenne SE-Hybrid	10.8	C/NMC	Samsung/Bosch	22
BMW	3 Series Plug-in	7.6	C/NMC	Samsung/Bosch	22
Mercedes	S550 Plug-In	6.4	C/NMC	Panasonic (Sanyo)	32
Mercedes	GLE 550E Hybrid	8.8	C/NCA and C/NMC	Tesla and SK Innovation†	30
Porsche	Panamera SE-Hybrid	9.4	C/NMC	Samsung/Bosch	35
Cadillac	ELR	17.1	C/NMC	LG Chem	60
†In process of changing suppliers.					
Note: NCA= $LiNi_{0.8}Co_{0.15}Al_{0.05}O_2$, NMC = $LiNi_{1-x-y}Mn_xCo_yO_2$, C = Graphite.					

To attract consumers towards electric mobilities, several governments have included incentivizing electric cars. This incentivization consists of both offering subsidies and investments to better charging infrastructures. A study based on the incentivization of EVs in Europe reveals that more than 80% of the new EV registration has taken place in 10 different cities/regions among Germany, United Kingdom (UK), France, the Netherlands, and Norway 2014[62]. Figure 10 indicates the relationship between the tax incentive and charging points per 1,000 registered cars among the above regions around Europe. As expected, the higher market shares of plug-in hybrid electric vehicles (PHEVs) and battery electric vehicles (BEVs) are found in cities/countries where sound incentives and charging infrastructures exist. For example, both of these criteria make Norway's EV share much higher than the rest of Europe. It is also interesting that a few individual cities/regions have a higher market share than their respective countries. For example, the EV development in Bergen, Oslo, and Utrecht is higher than in their respective countries. Indirect incentivization, including preferential treatment of EV consumers, application of EV in public transport, consumer outreach events, are the prime reasons for such a surge in market share.

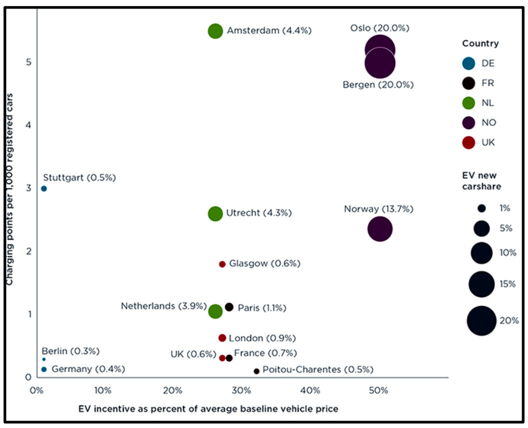

Fig. 10. The plot of fiscal incentives for EVs and charging point density for five European countries and ten cities/regions. The marker's size represented the EV share of newly registered vehicles [62].

Since 2014, a significant increase in EV market share has been observed in Germany. The recent data shows a sharp rise in EV market penetration in September 2020 in Germany. A large number of EVs sold in September (21,188 units) led to an increase of 260% compared to the last year[63]. Battery electric vehicles currently cover 8% of the total car share in Germany. Hybrid electric vehicles have observed an increase of 185%, leading to a total share of 20.4%. Although new registrations of gasoline-based cars have dropped by 24.4% (petrol and diesel engine), their market share remains higher (a total of 71.1%) compared to the EVs. A significant increase in EV share due to new government regulations and subsidies was observed during this period. Also, such growth in EV share has reduced the average carbon dioxide emissions by 13% (1,343 grams per kilometer) as compared to the last year. Besides, a record number of new EV registrations (2,04,251 units) are observed between January and September 2020 despite the economic shrinkage caused by the Covid-19 pandemic. Norway currently holds the largest EV share around the world.

The adequate incentives and easy access to charging stations have encouraged the consumers to move towards electric mobility slowly. In the first half of 2020, Norway has experienced 68% new cars[64]. The second and third positions were occupied by Iceland (49%) and Sweden (26%). Figure 11 represents a total of BEV and PHEV sales and percentage growth during the first half of 2020 (from January to June) instead of the last year. Covid-19 pandemic effects were more severe in Europe, as the new sales of EVs have increased to around 57% compared to the rest of the world.

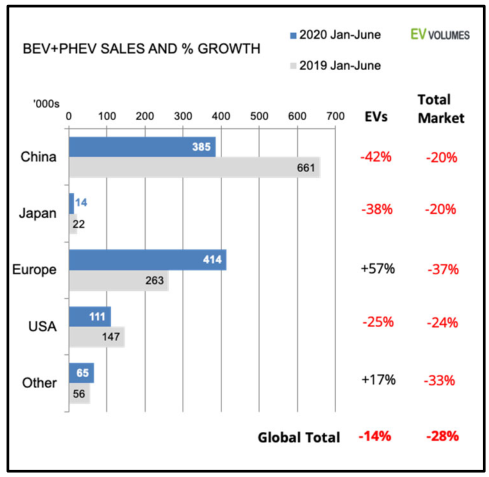

Fig. 11. The total of BEV and PHEV sales and percentage growth during the first half of 2020 (January to June) as opposed to the last year [64]

EVs – An Indian Perspective

The electrification of India's vehicles has experienced remarkable growth after the National Mission for Transformative Mobility launch in 2019. The motive behind this mission was to enforce clean, green, and sustainable vehicles on the road. The Indian EV market is currently dominated by electric three-wheelers (E3W). E3W has already penetrated smaller cities as these vehicles offer income to commercial transport agencies. BYD e-bus, electric two and four-wheelers have also contributed to the total market share[65]. Various Tier 1 city has also acquired electric buses for in-city transport. In 2014, Chinese manufacturers launched the BYD e-bus (K9D) in Bangalore[66]. The government of India's committee has sanctioned 5,645 e-buses for 65 cities in 2019 for intercity operation [67]. Olectra Greentech Ltd (Formerly Goldstone Infratech Ltd) built e-buses and delivered the first e-bus (K7) in Silvassa with a range of 200 km on a single fully charged battery [68]. Figure 12 illustrates multiple EV models currently functional in India and their respective prices in the Indian scenario [69].

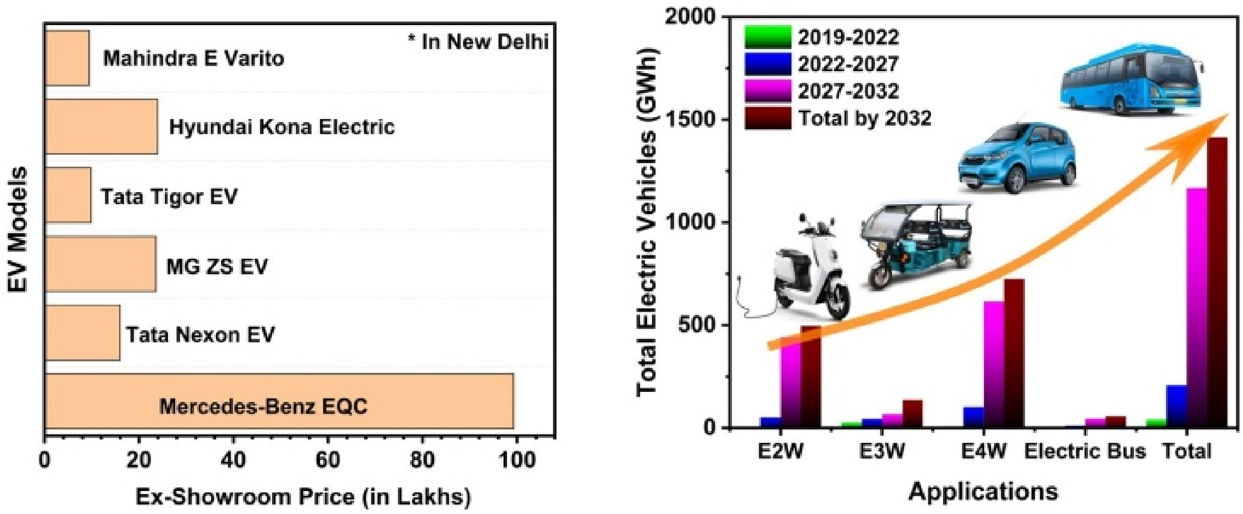

Fig. 12. Electric Cars scenario for India based on Energy Storage for Electric Mobility Applications (India Energy Storage Alliance Estimates) [70]

It is projected that E2Ws and E4Ws will cover most of the EV market shortly. The launch of large-scale LIB industries is anticipated under the Phased Manufacturing Programme (PMP) scheme for cost-effective battery productions. Such growth at the industry level will eventually encourage personal buyers to prefer EVs. In the next five years, EVs' cost is expected to surpass the price of ICE-based vehicles [70]. Figure 12 also presents the projected growth (Indian Energy Storage Alliance, IESA) of EVs across India till 2032.

Summary

LIBs presently dominate batteries in EVs as they provide high energy and power densities with appreciable driving range. However, LIBs inherently experience challenges, including high cost, low safety, and immature infrastructure. Overcharging and overheating of LIBs can cause thermal runway leading to fire hazards or explosion. Declining Li-resources also raise concerns regarding the reliability and shelf-life of LIB technology. Hence, a critical assessment of Li-ion chemistries is essential to comprehend the potential of LIBs in electric motilities and to realize the prospects in next-generation EVs. LIBs must attain a minimum cost of \$125 $(kWh)^{-1}$ and a high driving range of 500 km to achieve significant vehicles' electrification. Ni and Mn-based cathode materials like NCA, NMC, and blended LMO-NMC can considerably reduce the raw material costs. Similarly, moving towards Si-based anodes can also improve the specific energy and cut costs. Next-generation solid-state electrolyte-based LIBs enhance battery safety. Solid-state electrolyte found LIBs can also extend the specific energy range up to 900 $Whkg^{-1}$.

The innovation in the anode and cathode materials for LIBs with low cost, better battery efficiency, durability, and lightweight will be the top priorities to power EVs' demand. The next-generation anode material for LIBs could be silicon, and using these materials could improve the mileage of the EVs on a single charge. As a complementary technique to LIBs, sodium-ion batteries (SIBs) have gained momentum in the stationary storage and transport-based markets. What makes SIBs attractive is the abundant resources and comparable capacity and energy density to LIBs and lead-acid batteries. Recycling spent LIBs for EV applications can also add to sustainability and achieve good economic returns. At present, LIB technologies are almost indispensable in near-future EV applications, while various green and sustainable alternatives can lower their dependency in the far future.

Acknowledgements

This work was supported by funding from the Science & Engineering Research Board (SERB), DST, GoI, India, (Early Career Research Award (Grant No: ECR/2016/002003)). Nagmani, D.P and AT acknowledge the Ministry of Education, GoI, and IIT Kharagpur for the Ph.D. fellowship.

CRediT authorship contribution statement

Nagmani: Literature review, Conceptualization, Permissions, Figures, TOC and Tables, and Writing - original draft preparation, editing and review. **Debanjana Pahari**: Literature review, Permissions, Figures and Tables, and Writing - draft preparation. **Ashwani Tyagi**: Permissions, Figures and Tables, and TOC. **Sreeraj Puravankara**: Conceptualization, Supervision, Resources, Writing - review & editing, Funding Acquisition, and Project Administration.

Declaration of competing interests

The authors declare no known competing financial interests or personal relationships that could have influenced this review article, and there are no conflicts of interests to declare.

References

[1] Onori, S.; Serrao, L.; Rizzoni, G. Hybrid Electric Vehicles: Energy Management Strategies; *Springer: Berlin/Heidelberg*, Germany, 2016. https://doi.org/10.1007/978-1-4471-6781-5.

[2] Morimota, M. Which is the First Electric Vehicle? *Electrical Engineering in Japan. 192* (2), 31-38, 2015. https://doi.org/10.1002/eej.22550.

[3] White, John H. *A History of the American Locomotive: Its Development, pp.1830-1880. North Chelmsford, MA: Courier*. p. 14. 1979. ISBN 9780486238180.

[4] May, G. J., Davidson, A., Monahov, B. Lead batteries for utility energy storage: A review. *J. Energy Storage*, *15*, 145-157, 2018. https://doi.org/10.1016/j.est.2017.11.008.

[5] Prengaman, R. D., Mirza, A. H. Recycling concepts for lead-acid batteries. *Lead-Acid Batteries for Future Automobiles,* 578-598, 2017. https://doi.org/10.1016/B978-0-444-63700-0.00020-9.

[6] Shafiee, S., Topal, E. A long-term view of worldwide fossil fuel prices. *Appl. Energy*, *87*(3), 988-1000, 2010. https://doi.org/10.1016/j.apenergy.2009.09.012.

[7] Baffes, J., Kose, M. A., Ohnsorge, F., Stocker, M. The Great Plunge in Oil Prices: Causes, Consequences, and Policy Responses. *World Bank group*, Policy Research Note, PRN/15/01, 2015. http://hdl.handle.net/10986/23611.

[8] Chian, T. Y., Wei, W. L. J., Le, E. L. Ze., Ren, L. Z., Ping, Y. E., Bakar, N. Z. A., Faizal, M., Shivkumar, S. A Review on Recent Progress of Batteries for Electric Vehicles. *Int. J. Appl. Eng. Res., 14*, 4441-4461, 2019. http://www.ripublication.com.

[9] Chan, C. C. The state of the art of electric and hybrid vehicles. *Proceedings of the IEEE*, *90*(2), 247-275, 2002. https://doi.org/10.1109/5.989873.

[10] Gifford, P., Adams, J., Corrigan, D., Venkatesan, S. Development of advanced nickel/metal hydride batteries for electric and hybrid vehicles. *J. Power Sources*, *80*(1-2), 157-163, 1999. https://doi.org/10.1016/S0378-7753(99)00070-1.

[11] Micah, S. Z., Juhyun, S., and Jessika, E. T. Determinants of lithium-ion battery technology cost decline. Energy Environ. Sci., 14, 6074-6098, 2021. https://doi.org/10.1039/D1EE01313K.

[12] IEA (2020). *Global EV Outlook 2020*. IEA, Paris. https://www.iea.org/reports/global-ev-outlook-2020. (Accessed December 18, 2021).

[13] Staunton, R. H., Ayers, C. W., Marlino, L. D., Chiasson, J. N., and Burress, B. A. Evaluation of 2004 Toyota Prius Hybrid Electric Drive System. UT-Battelle, ORNL-27 (4-00), U.S. Department of Energy, 2006. http://www.osti.gov/bridge.

[14] Verbelen, F., Lhomme, W., Vinot, E., Stuyts, J., Vafaeipour, M., Hegazy, O., Sergeant, P. Comparison of an optimized electrical variable transmission with the Toyota Hybrid System. *Applied Energy*, *278*, 115616, 2020. https://doi.org/10.1016/j.apenergy.2020.115616.

[15] Press Release, 13% of total new car registrations in Europe made up by EVs in January 2020, *JATO* (London, UK) 2020. https://www.jato.com/13-of-total-new-car-registrations-in-europe-made-up-by-evs-in-january-2020/. (Accessed December 20, 2021).

[16] Song, D., Ruojin, L. Forecasting the sales and stock of electric vehicles using a novel self-adaptive optimized grey model, *Engineering Applications of Artificial Intelligence*, *100*, 104148, 2021. https://doi.org/10.1016/j.engappai.2020.104148.

[17] Jain, A., Prasad, A., Sharma, S., Patni, J. C. Electric Cars a New Era of Digital India-Autonomous Cars or Smart Cars. *5th International Conference on Next Generation Computing Technologies (NGCT-2019)*, 2020. https://dx.doi.org/10.2139/ssrn.3545099.

[18] Marom, R., Ziv, B., Banerjee, A., Cahana, B., Luski, S., Aurbach, D. Enhanced performance of starter lighting ignition type lead-acid batteries with carbon nanotubes as an additive to the active mass. *J. Power Sources, 296*, 78-85, 2015. https://doi.org/10.1016/j.jpowsour.2015.07.007.

[19] Vishal, S. Electric Vehicles in India: Current Trends and Future Forecasts. *International Journal of Electric and Hybrid Vehicles, 13* (2), 117-126, 2021. https://dx.doi.org/10.1504/IJEHV.2021.117836.

[20] Dhar, S. K., Ovshinsky, S. R., Gifford, P. R., Corrigan, D. A., Fetcenko, M. A., Venkatesan, S. Nickel/metal hydride technology for consumer and electric vehicle batteries-a review and up-date. *J. Power Sources*, *65*(1-2), 1-7, 1997. https://doi.org/10.1016/S0378-7753(96)02599-2.

[21] Ding, Y., Cano, Z. P., Yu, A., Lu, J., Chen, Z. Automotive Li-Ion Batteries: Current Status and Future Perspectives. *Electrochemistry Energy Reviews, 2*, 1-28, 2019. https://doi.org/10.1007/s41918-018-0022-z.

[22] Berckmans, G., Messagie, M., Smekens, J., Omar, N., Vanhaverbeke, L., Mierlo, J. V. Cost Projection of State of the Art Lithium-Ion Batteries for Electric Vehicles Up to 2030. *Energies, 10* (9), 1914, 2017. https://doi.org/10.3390/en10091314.

[23] Padhi, A. K., Nanjundaswamy, K. S., & Goodenough, J. B. Phospho-olivines as positive-electrode materials for rechargeable

lithium batteries. *J. Electrochem. Soc.*, *144*(4), 1188, 1997. https://doi.org/10.1149/1.1837571.

[24] Anseán, G. D., González, V. M., Viera, J. C., Álvarez A. J. C., Blanco V. C. J., García, V. M., Evaluation of $LiFePO_4$ batteries for Electric Vehicle applications. *International Conference on New Concepts in Smart Cities: Fostering Public and Private Alliances, SmartMILE*, 1-8, 2013. http://dx.doi.org/10.1109/SmartMILE.2013.6708211.

[25] Andre, D., Kim, S. J., Lamp, P., Lux, S. F., Maglia, F., Paschos, O., Stiaszny, B. Future generations of cathode materials: an automotive industry perspective. *J. Mater. Chem. A*, *3*(13), 6709-6732, 2015. https://doi.org/10.1039/C5TA00361J.

[26] Li, H., Li, J., Ma, X., Dahn, J. R. Synthesis of single crystal $LiNi_{0.6}Mn_{0.2}Co_{0.2}O_2$ with enhanced electrochemical performance for lithium-ion batteries. *J. Electrochem. Soc.*, *165*(5), A1038, 2018. https://doi.org/10.1149/2.0951805jes.

[27] Delmas, C., Saadoune, I., Rougier, A. The cycling properties of the $Li_xNi_{1-y}Co_yO_2$ electrode. *J. Power Sources*, *44*(1-3), 595-602, 1993. https://doi.org/10.1016/0378-7753(93)80208-7.

[28] Li, W., Liu, X., Celio, H., Smith, P., Dolocan, A., Chi, M., Manthiram, A. Mn versus Al in layered oxide cathodes in lithium-ion batteries: a comprehensive evaluation on long-term cyclability. *Adv. Energy Mater.*, *8*(15), 1703154, 2018. https://doi.org/10.1002/aenm.201703154.

[29] Zhang, X., Jiang, W. J., Mauger, A., Gendron, F., & Julien, C. M. Minimization of the cation mixing in $Li_{1+x}(NMC)_{1-x}O_2$ as cathode material. *J. Power Sources*, *195*(5), 1292-1301, 2010. https://doi.org/10.1016/j.jpowsour.2009.09.029.

[30] Schmuch, R., Wagner, R., Hörpel, G., Placke, T., Winter, M. Performance and cost of materials for lithium-based rechargeable automotive batteries. *Nat. Energy*, *3*(4), 267-278, 2018. https://doi.org/10.1038/s41560-018-0107-2.

[31] Manthiram, A., Song, B., Li, W. A perspective on nickel-rich layered oxide cathodes for lithium-ion batteries. *Energy Storage Mater.*, *6*, 125-139, 2017. https://doi.org/10.1016/j.ensm.2016.10.007.

[32] Thackeray, M. M., Kang, S. H., Johnson, C. S., Vaughey, J. T., Benedek, R., Hackney, S. A. Li_2MnO_3-stabilized $LiMO_2$ (M= Mn, Ni, Co) electrodes for lithium-ion batteries. *J. Mater. Chem.*, *17*(30), 3112-3125, 2007. https://doi.org/10.1039/B702425H.

[33] Schmuch, R., Wagner, R., Hörpel, G., Placke, T., Winter M. Performance and cost of materials for lithium-based rechargeable automotive batteries. *Nat. Energy, 3*, 267-278, 2018. https://doi.org/10.1038/s41560-018-0107-2.

[34] Miao, Y., Hynan, P., Jouanne, A. V., Yokochi, A. Current Li-ion battery technologies in electric vehicles and opportunities for advancements. *Energies, 12*, 1074, 2019. https://doi.org/10.3390/en12061074.

[35] Jun, L., Zhongwei, C., Feng, P., Yi, C., Khalil, A. High-performance anode materials for rechargeable lithium-ion batteries. *Electrochemical Energy Reviews, 1,* 35-53, 2018. https://doi.org/10.1007/s41918-018-0001-4.

[36] Jian, D., Xuan, T., Haifeng, D., Ying, Y., Wangyan, W., Xuezhe, W., Yunhui, H. Building safe lithium-ion batteries for electric vehicles: A Review. *Electrochemical Energy Review, 3*, 1-42, 2019. https://doi.org/10.1007/s41918-019-00060-4.

[37] Luo, Y., Guo, L., Xiao, M., Wang, S., Ren, S., Han, D., Meng, Y. Strategies for inhibiting anode dendrite growth in lithium–sulfur batteries. *J. Mater. Chem. A, 2*, 4629-4646, 2020. https://doi.org/10.1039/C9TA12910C.

[38] Liu, Q., Du, C., Shen, B., Zuo, P., Cheng, X., Ma, Y., Yin, G., Gao, Y. Understanding undesirable anode lithium plating issues in lithium-ion batteries. *RSC Advances, 6*, 88683-88700, 2016. https://doi.org/10.1039/C6RA19482F.

[39] Chen, X., Shen, W.,Vo, Z. Cao and A. Kapoor. An overview of lithium-ion batteries for electric vehicles. *10th International Power & Energy Conference (IPEC)*, pp. 230-235, 2012. https://doi.org/10.1109/ASSCC.2012.6523269.

[40] Norio, T., Keigo H., Hiroki I. Lithium diffusion in $Li_{4/3}Ti_{5/3}O_4$ particles during insertion and extraction. *J. Electrochem. Soc., 158 (6)*, A725-A730, 2011. https://doi.org/10.1149/1.3574037.

[41] Kai, W., Jun, Y., Yao, Z., Chenyun, W., Deyu, W. Investigation on $Li_4Ti_5O_{12}$ batteries developed for hybrid electric vehicle. *J. Appl. Electrochem., 42*, 989-995, 2012. https://doi.org/10.1007/s10800-012-0442-0.

[42] Qiangfeng, X., Bing, L., Fang, D., Li, Y., Mei C. Application of Lithium-Ion Batteries in Vehicle Electrification. *Electrochemical Energy: Advanced Materials and Technologies, 6*, 159, 2015. http://dx.doi.org/10.1201/b19061-9.

[43] Fei, D., Liyi, S., Guorong, C., Dengsong Z. Silicon/carbon composite anode materials for lithium-ion batteries. Electrochemical Energy Reviews, 2, 149-198, 2019. https://doi.org/10.1007/s41918-018-00028-w.

[44] Enevate's Silicon Anodes Could Yield EV Batteries that Run 400 Km on a 5-Minute Charge - *IEEE* Spectrum, 2020.

https://www.enevate.com/enevates-silicon-anodes-could-yield-ev-batteries-that-run-400-km-on-a-5-minute-charge/ (Accessed November 27, 2021).

[45] Yan, Lu., Le, Y., Xiong, W. L. Nanostructured conversion-type anode materials for advanced lithium-ion batteries. *Chem. 4*, 972-996, 2018. https://doi.org/10.1016/j.chempr.2018.01.003.

[46] Yu, S. H., Feng, X., Zhang, N., Seok, J., Abruña, H. D. Understanding Conversion-Type Electrodes for Lithium Rechargeable Batteries. *Accounts of Chemical Research,* 273–281, 2018. https://doi.org/10.1021/acs.accounts.7b00487.

[47] Yu, S. H., Lee, S.H., Lee, D.J., Sung, Y. E., Hyeon, T. Conversion Reaction-Based Oxide Nanomaterials for Lithium-Ion Battery Anodes. *Small, 12*, 2146–2172, 2016. https://doi.org/10.1002/smll.201502299.

[48] Yoon, S. J., Andrew, S. C., Leah, A. R., Sun-Ho, K., Anne, C. D., Markus, D. G., Steven, M. G., Se-Hee, L. Ultrathin direct atomic layer deposition on composite electrodes for highly durable and safe Li-ion batteries. *Adv. Mater., 22 (19)*, 2010. https://doi.org/10.1002/adma.200903951.

[49] Zheng, C., Po-Chun, H., Jeffrey, L., Yuzhang, L., John, W. F. T., Nan, L., Chao, W., Sean, C., Andrews, J. L., Yi, C., Zhenen, B. Fast and reversible thermoresponsive polymer switching materials for safer batteries. *Nat. Energy, 1*, 15009, 2016. https://doi.org/10.1038/nenergy.2015.9.

[50] Nowak, S., Winter, M. Chemical analysis for a better understanding of aging and degradation mechanisms of non-aqueous electrolytes for lithium-ion batteries: method development, application and lessons learned. *J. Electrochem. Soc.*, *162*(14), A2500, 2015. https://doi.org/10.1149/2.0121514jes.

[51] Burow, D., Sergeeva, K., Calles, S., Schorb, K., Boerger, A., Roth, C., Heitjans, P. Inhomogeneous degradation of graphite anodes in automotive lithium-ion batteries under low-temperature pulse cycling conditions. *J. Power Sources*, *307*, 806-814, 2016. https://doi.org/10.1016/j.jpowsour.2016.01.033.

[52] Pahari, D., Puravankara, S. Greener, Safer, and Sustainable Batteries: An Insight into Aqueous Electrolytes for Sodium-Ion Batteries. *ACS Sustain. Chem. Eng.*, *8*(29), 10613-10625, 2020. https://doi.org/10.1021/acssuschemeng.0c02145.

[53] Janek, J., Zeier, W. G. A solid future for battery development. *Nat. Energy*, *1*(9), 1-4, 2016. http://dx.doi.org/10.1038/nenergy.2016.141.

[54] Cheng, K. W. E., Divakar, B. P., Wu, H., Ding, K., Ho, H. F. Battery-management system (BMS) and SOC development for electric vehicles. *IEEE Trans. Veh. Technol.*, *60*(1), 76-88, 2010. http://dx.doi.org/10.1109/TVT.2010.2089647.

[55] Nagmani., and Puravankara, P. Insight into the diverse precursor-based micro-spherical hard carbons as anode materials for sodium-ion and potassium-ion batteries. *Material Advances, 3*, 810, 2022. https://doi.org/10.1039/D1MA00731A.

[56] Nagmani., and Puravankara, P. Insight into the Plateau Capacity Dependence on the Rate Performance and Cycling Stability of a Superior Hard Carbon Microsphere Anode for Sodium-Ion Batteries. *ACS Appl. Energy Mater.*, *3*(10), 10045–10052, 2020. https://doi.org/10.1021/acsaem.0c01750.

[57] König, A., Nicoletti, L., Schröder, D., Wolff, S., Waclaw, A., Lienkamp, M. An Overview of Parameter and Cost for Battery Electric Vehicles. *World Electric Vehicle Journal. 12* (1), 21, 2021. https://doi.org/10.3390/wevj12010021.

[58] Goldie-Scot, L. A Behind the Scenes take on Lithium-ion Battery Prices. *BNEF Blog*, 2019. https://about.bnef.com/blog/behind-scenes-take-lithium-ion-battery-prices/. (Accessed November 28, 2021).

[59] Michael A. Cusumano. Self-Driving Vehicle Technology: Progress and Promises. *Communications of the ACM*, 63(10), 20-22, 2020. https://doi.org/10.1145/3417074.

[60] Jaiswal, D., Kaushal, V., Kant, R., Singh, K. P. Consumer adoption intention for electric vehicles: Insights and evidence from Indian sustainable transportation, *Technological Forecasting and Social Change, 173*, 121089, 2021. https://doi.org/10.1016/j.techfore.2021.121089.

[61] Blomgren, G. E. The development and future of lithium-ion batteries. *J. Electrochem. Soc.*, *164*(1), A5019, 2016. https://doi.org/10.1149/2.0251701jes.

[62] Tietge, U., Mock, P., Lutsey, N., Campestrini, A. Comparison of leading electric vehicle policy and deployment in Europe. *Int. Council Clean Transp*, *49*, 847129-102, 2016. https://theicct.org/comparison-ev-policies-europe-2016.

[63] Amelang, S. Germany registers more than 20,000 pure electric cars in a month for first time. Journalism for the Energy Transition, (2020). https://www.cleanenergywire.org/news/germany-registers-more-20000-pure-electric-cars-month-first-time. (Accessed on December 08, 2021).

[64] The Electric Vehicles world sales database, EV Volume, 2021. https://www.ev-volumes.com/datacenter/. (Accessed December 10, 2021).

[65] Vedant, S., Virender, S., Vaibhav, S. Analysis of electric vehicle trends, development and policies in India. *Case Studies on Transport Policy, 9* (3), 1180-1197, 2021. https://doi.org/10.1016/j.cstp.2021.06.006.

[66] Goel, S., Sharma, R., Rathore, K A. A review on barrier and challenges of electric vehicle in India and vehicle to grid optimization. *Transportation Engineering ,4*, 100057, 2021. https://doi.org/10.1016/j.treng.2021.100057.

[67] Maske, P., Chel, P. A., Goyal, P. K., & Kaushik, D. G. Sustainable Perspective of Electric Vehicles and Its Future Prospects. *Journal of Sustainable Materials Processing and Management*, 1(1), 17–32, 2021. https://publisher.uthm.edu.my/ojs/index.php/jsmpm/article/view/10022.

[68] Pal, S., Basudeb, D., Bartik, C., Sanjay, S., Deb, S R., Tirthankar, D R., Suparna, C. Recent Developments and Future Scopes of Electrical Vehicles in Power Market on Covid-19 Pandemic situation. *J. Phys.: Conf. Ser., 1797*, 012058, 2021. http://dx.doi.org/10.1088/1742-6596/1797/1/012058.

[69] Aijaz I., Ahmad A. Electric Vehicles for Environmental Sustainability. In: Agarwal P., Mittal M., Ahmed J., Idrees S.M. (eds). Smart Technologies for Energy and Environmental Sustainability. Green Energy and Technology. Springer, Cham, 1, XII, 273, 2022. https://doi.org/10.1007/978-3-030-80702-3.

[70] IESA report, Energy Storage System Roadmap for India: 2019-2032, (2019). http://www.indiaenvironmentportal.org.in/node/466097/. (Accessed December 12, 2021).

Address correspondence to *Mr. Nagmani School of Energy Science & Engineering, IIT Kharagpur, Kharagpur – 721302, West Bengal, India*
Email: nagmani@iitkgp.ac.in